POLITECNICO DI MILANO
DIPARTIMENTO DI SCIENZE E TECNOLOGIE AEROSPAZIALI
DOCTORAL PROGRAMME IN ROTARY–WING AIRCRAFT

WING–ROTOR AERODYNAMIC INTERACTION IN TILTROTOR AIRCRAFT

Doctoral Dissertation of:
Giovanni Droandi

Supervisor:
Prof. Giuseppe Gibertini

Tutor:
Prof. Luigi Vigevano

The Chair of the Doctoral Program:
Prof. Luigi Vigevano

Year 2014 – XXVI CYCLE

A Gaia

Acknowledgements

I would like to express my thankfulness to those people who were close to me during the development of this work.

First of all, I am very grateful to my supervisor, Prof. Gibertini, because he gave me the opportunity to do what I love during the last three years. With his experience, he guided me through the difficulties I often encountered during my work. I very much enjoyed working with him and I would like to thank him for the many helpful and encouraging discussions we had during the course of my Ph.D. studies. Thanks to him, I had the possibility to join a professional working environment where I could take advantage of professional training and to increase and develop my technical skills. In the working environment, I met very skilled people that helped me when I faced problems and issues and, most important of all, with who I became really good friend. In this regard, I want to thank Donato and Gabriele for their precious help. Three years ago, when I started to work with them, I had no idea where to start from to run an experimental test. With plenty of patience, they taught me a lot of relevant tricks and they helped me to design, develop and realise such a complex test rig. Thanks to Alex, my officemate, for all the suggestions provided during these years and for giving me a fundamental help in PIV measurements. Thanks to Alessandro, Luca and Lorenzo who gave me solid support and encouragement in my work and for bearing with me during the time. I also want to acknowledge the help of Prof. Lanz who gave me a priceless support for the structural design of the blades. I say thank you to Dr. Schwarz, who offered to review this work.

Thanks to mom and dad for their love and their constant presence by my side. I would like to thank my grandmother for being there for me and all my family for their continuous encouragement. I also want to thank all my friends for giving me support. In particular, thanks to Dario and Andrea for sharing crazy adventures in Milano and beyond. Thanks also to Alessandro, Francesco, Marco and Fabio for believing in me.

At last, I would like to thank the most important person in my life, Gaia. Even though she lives far away at the moment, she is always by my side.

Abstract

A tiltrotor is an aircraft that combines the capability to hover, typical of helicopters, with the possibility to flight in cruise at high speed, like propeller driven aircraft. It represents a concrete possibility to overcome the main limitations of helicopters and propeller aircraft by matching together the peculiarities of both of them. However, the hovering performance and the lifting capability of tiltrotor aircraft are strongly affected by the aerodynamic interaction between wing and rotors. In helicopter flight mode, the presence of the wing under the rotor modifies the rotor wake and thus is responsible for the loss of rotor performance. To have acceptable hover performance, in existing tiltrotor large rotors have been adopted however increasing the aerodynamic interference due to wing–rotor interaction. Large rotors prevent also the take–off and landing in aircraft flight mode and lead to important limitations in cruise flight.

Since the improvement of the performance in aircraft mode is one of the focus points for future developments of new tiltrotor, non conventional configurations have to be investigated in order to preserve the performance in helicopter mode. A possible approach to improve the performance in aircraft mode is to modify the blade shape by reducing the rotor diameter to get a propeller similar to the ones of propeller aircraft. This solution leads to the tiltwing concept. A tiltwing aircraft has the possibility to tilt the external part of the wing with the rotor, minimising the wing surface on which the rotor wake strikes. Good hover performance are preserved and wing–rotor interference is reduced. Even if the tiltwing solution was the subject of several studies, many aspects of this configuration have to be further analysed for future evolutions and applications.

The objective of the present research activity is to investigate from both experimental and numerical points of view the aerodynamic interference between wing and rotor on a high–performance tiltwing aircraft. For this purpose, a tiltwing aircraft geometry has been defined and numerical calculations have been used to get a first insight on the problem. Once the rotor blade and the wing have been designed at full–scale, a 0.25 scaled wind tunnel half–model has been manufactured to study the hover flight condition. Since the aerodynamic interaction between wing and rotor is very complex, force measurements may give only partial information about the phenomena related to this non conventional configuration. Aircraft performance and rotor wake geometry have been investigated by means of forces and Particle Image Velocimetry measurements.

Compendio

Un convertiplano è un aeromobile che combina la capacità di operare a punto fisso, tipica degli elicotteri, e la possibilità di volare in crociera ad alte velocità, propria degli aeroplani ad elica. Il convertiplano rappresenta una possibilità concreta di superare le limitazioni intrinseche degli elicotteri e degli aeroplani raccogliendo insieme le loro peculiarità. Tuttavia, le prestazioni sono influenzate dall'interazione aerodinamica che si crea tra rotore ed ala. In modalià elicottero, la presenza dell'ala sotto al rotore ne modifica la scia provocando una netta perdita di prestazioni. Per avere prestazioni accettabili, nei modelli esistenti vengono utilizzati rotori di grandi dimensioni che provocano un aumento dell'interferenza aerodinamica, impediscono il decollo e l'atterraggio orizzontali e comportano forti limitazioni in crociera in modalità aeroplano.

Poichè l'incremento delle prestazioni in modalità aeroplano è uno degli obbiettivi principali nello sviluppo di di nuovi convertiplani, è necessario lo studio di configurazioni alternative al fine di preservare buone prestazioni in modalità elicottero. Una possibile soluzione è rappresentata dalla riduzione del diametro del rotore e dalla modifica delle pale nel tentativo di ottenere un rotore che sia più simile a quello dei velivoli ad elica. Questa soluzione ha portato allo studio dei convertiplani tiltwing, in grado di ruotare la parte esterna dell'ala insieme al rotore, minimizzando la superficie frontale dell'ala investita dalla scia del rotore. In questo modo, riducendo gli effetti legati all'interazione tra ala e rotore, vengono mantenute buone prestazioni in volo a punto fisso. Anche se questa configurazione è stata soggetto di numerosi studi, sono ancora molti gli aspetti che devono essere studiati in dettaglio.

L'obbiettivo del presente lavoro è lo studio sperimentale e numerico dell'interazione aerodinamica che si instaura tra ala e rotore in un convertiplano di tipo tiltwing. Dopo aver definito la geometria di un aeromobile appartenente a questa classe, si è cominciato lo studio di questa configurazione per mezzo di strumenti numerici che sono serviti anche per il progetto aerodinamico delle pale del rotore e dell'ala. È stato progettato e realizzato un nuovo modello sperimentale in scala per studiare la condizione di volo a punto fisso. Data la complessità dei fenomeni che riguardano questo tipo di interazione aerodinamica, le misure di forza riescono a dare solo informazioni parziali. Per meglio comprendere i fenomeni legati a tale problema, il campo di moto è stato studiato anche attraverso l'utilizzo della Velocimetria ad Immagini di Particelle.

Contents

List of Figures

List of Tables

CHAPTER 1

Introduction

1.1 Motivations

Throughout history, the idea of an aircraft with the capability to Vertical Takeoff and Landing (VTOL) attracted the interest of many inventors and designers which proposed numerous solutions characterised by a wide variety of lifting and propulsion devices. Even though it is generally accepted that the aerial–screw designed by the Renaissance genius Leonardo da Vinci is the predecessor to the modern day helicopters, the concept of vertical flight aircraft is already found in some Chinese toys of about $400\ BC$, known as Chinese tops (described by Everett–Heath [23] and Liberatore [50]). Da Vinci's helicopter–like machine, dated 1483, was made from reed, linen and wire. Four men standing on a central platform should power the machine turning cranks to rotate the shaft in such a way "that said screw bores through the air and climbs high". Despite the da Vinci's machine would not have been able to take flight due to weight constrictions, his idea was far ahead of its time. Additionally, da Vinci was aware that to produce enough lift to flight the rotor needed to be large, indeed he designed the aerial–screw having a rotor with a diameter of 8 *braccia* (which corresponds to a length varing from $4.5\ m$ to $7.9\ m$, depending on the definition of the old Florentine unit of measure). Many years later, between the late 1940s and early 1960s this elementary concept led to the definition of the disk loading parameter (where disc loading DL is commonly defined as the thrust divided by the area over which it is produced [44]). It allows to understand for a given VTOL aircraft the achievable level of efficiency in the production of the required thrust to hover. As explained by Leishman [48], VTOL aircraft that have a low disk loading will require low values of power per unit of thrust produced becoming more efficient and consuming less fuel with respect to aircraft characterised by high disk loading. It is straightforward that aircraft with low disk loading represent a good solution every time lower fuel consumption in hover flight is needed, or extended–

duration hover or near–hover conditions are required. However, VTOL aircraft need to have good performance also in cruise flight, with certain speed and range requirements, and not only in hover flight. The problem of designing an aircraft able to have good performance both in hover and in cruise flight at high speed was the major challenging task for the development of the VTOL aircraft.

In the context of VTOL aircraft design, helicopters should appear to be the right choice thanks to their large rotors which imply very low disk loading devices. As known, the purpose of the helicopter main rotor is to provide a vertical lift force to balance the weight of the aircraft in hover flight. On the other hand, in forward flight condition the same device has to provide at the same time a propulsive force that should be able to win the drag of the helicopter (mainly due to fuselage, rotor hub, landing gear and other devices) and a lift force to balance its weight. However, conventional helicopters exhibit some important limitations in forward flight that restrict the scope of their use. In fact, since the rotor blades of conventional helicopters encounter an asymmetric velocity field in forward flight, the main rotor is affected by strong limitations of aerodynamic nature. One of the main problems is related to the power losses given by compressibility effects that arise on the outer part of the advancing blade at high speed in forward flight conditions. The stall phenomenon on the main rotor retreating blade represents another important aerodynamic effect that occurs at high forward flight speed or during maneuvers at high load factors and is responsible for the production of negative effects on helicopter performance. These problems lead to significant restrictions of helicopter performance in terms of cruise speed in level flight. In this regards, modern helicopters are able to fly in cruise at about $300\ km/h$ with an operative range of about $800\ km$.

1.2 Non conventional helicopters history

With the aim of finding an aircraft configuration which is able to overcome the limitations exhibited by conventional helicopters, Dr. James Allan Jamieson Bennett in 1939 issued a patent from the UK Patent Office about the gyrodyne, an intermediate type of rotorcraft proposed in 1936 [7]. With the help of an auxiliary propulsion device and wings to unload the main rotor, the Jet Gyrodyne prototype flew for the first time in 1954, and performed a complete transition from vertical to horizontal flight in March 1955. In 1951, the McDonnell Aircraft Co. proposed the experimental compound XV–1 aircraft [26] in the frame of the joint U.S. Army and U.S. Air Force Convertiplane Program. This aircraft included features such as a three bladed main rotor, low–mounted wings, and a pusher propeller at the rear which provided the thrust in forward flight. In 1955 the XV–1 model would reach a speed of $300\ km/h$ demonstrating however that the problem limiting the speed capability of the conventional helicopter were still present in high speed flight. In the late 1960s the revolutionary Lockheed AH–56 Cheyenne model was proposed by Lockheed Martin in the frame of compound helicopters. Even if this aircraft had good performance in forward flight and could fly at over $407\ km/h$, the Cheyenne program was cancelled in 1972. During the last 10 years, other two high-speed compound helicopters have been developed by Sikorsky Aircraft Corporation and Eurocoper. The Sikorsky X2 model was an experimental model with coaxial rotors which reached a speed of $460\ km/h$ in level flight. The X3 (X–Cubed) is the Eurocopter experimental compound helicopter, now under development, which became the World's Fastest Helicopter by reaching a speed of $472\ km/h$ on June 2013.

Some years before the Bennett's proposal, the need for an aircraft that would be able to combine together the capability to hover and possibility to takeoff and landing vertically with the high speed cruise performance of fixed–wing aircraft led to the tiltrotor aircraft concept. At the beginning of 1920s, Henry Berliner [77] proposed an innovative flying machine that was a fixed–wing biplane with two large diameter fixed–pitch propeller mounted on a vertical shaft at the tip of the upper wing. By tilting forward the shafts, the Berliner helicopter was able to achieve a flight speed of about $64\ km/h$. In September 1930, George Lehberger issued a patent for his so called "Flying Machine" which employs together for the first time the concept of tilting rotor with the low disk loading idea. During the following twenty years, some early tiltrotor models were developed with little success until the Transcendental Aircraft Corporation of New Castle, Delaware, proposed the Model 1–G tiltrotor aircraft in 1947. Between 1954 and 1955, the experimental aircraft was able to complete more than 100 flights and it is commonly recognised as the first tiltrotor aircraft which successfully explore the conversion flight mode. In the same period, general mission requirements for new aircraft were strongly conditioned by military requirements. In particular, rescue operations required for aircraft with extended–duration hover capabilities, low speed maneuvering and increased speed and operative range. For these reasons, in 1951 a joint research program between the U.S. Army and U.S. Air Force was started to explore the possibility to build new aircraft with convertiplane technologies. In addition to the compound XV–1 model by McDonnell Aircraft Co., the XV–2 stoppable rotor by Sikorsky Aircraft and the XV–3 tiltrotor aircraft by Bell Helicopter Company were proposed. In the end, however it was decided to develop only the first and the latter models. While the XV–1 model exhibited its limitations very soon by demonstrating its inability to overcome the typical helicopter problems, the Bell XV–3 aircraft was recognised to have the potential to overpass the main helicopter limitations. Therefore, the XV–3 model became the subject of many investigations even though it was characterised by numerous technical problems. In the period between the 1953 and 1968, a wide series of flight and ground tests and wind tunnel experiments were conducted by Bell and NASA (National Aeronautics and Space Administration). A description of the XV–3 research activities was given by Maisel et all. [54]. When the XV–3 research program was terminated, engineers understood that the main technical problems characterising this aircraft were related to several factors: the dynamic instability which occurred during conversion and aeroplane modes was due to aeroelastic instability of the rotor/pylon/wing system [35]; helicopter–like rotor blades were not the best choice for tiltrotor aircraft because they suffered power losses due to onset of compressibility effects in aircraft mode at high speed. Moreover, with the goal to solve these problems, further modifications were applied to the original aircraft configuration however leading to a degradation of performance both in hover and cruise flight.

While the rotor/pylon/wing aeroelastic instability was solved by the introduction of a new hinged (gimbaled) rotor hub design in which a pitch change mechanism was used to increase the blade flapping when out–of–plane motion occurred [27], the design of rotor blade became the objective of new studies. Moreover, at the beginning of the 1970s, some large experimental models representing both isolated rotors and rotors installed on half–wings were tested in the Ames Research Center 40– by 80–feet wind tunnel. These experimental test data were used to get a fundamental understanding of the physical phenomenon related to the interaction between wing and rotor [40], [41] and also they represented a basis to develop the first numerical codes to predict the performance of tiltrotor aircraft [43], [42]. New strategies were applied to design the blades ad–hoc for tiltrotor aircraft. Several research activities were carried out to investigate the sensitivity of rotor performance to twist and chord variations, like the Bell Model 300 titlrotor aircraft design, both at ONERA S–1 wind tunnel and Ames Research Center 40– by 80–feet wind tunnel [15].

Starting from the Bell Model 300, the Bell Helicopter company took part to the XV–15 program competition proposed in 1971 by NASA and won the contract to develop the so called Bell Model 301. During the next twenty years Bell designed and developed two tiltrotor prototypes which became the subject of a wide numbers of experimental tests (wind tunnel [82] and flight tests [83]) and numerical activities [58], [53]. The XV–15 program first results were so encouraging that, in 1983, Bell Helicopter together with Boing Vertol started to work on a program for the development of a new and bigger tiltrotor aircraft. The Joint–service Vertical takeoff/landing Experimental (JVX) aircraft program supported by the U.S. Department of Defense led to the design of the V–22 Osprey tiltrotor aircraft (first tiltrotor which went into production). Also in this case, many experimental and numerical studies were conducted on the V–22 Osprey. An extensive experimental database was built in the frame of the JVX program on the experimental half–model tested both in the Outdoor Aerodynamic Research Facility (OARF) at NASA–Ames [57] and in the Ames Research Center 40– by 80–feet wind tunnel [2]. The results of these works led to a better understanding of some physical phenomenon on the wing–rotor aerodynamic interaction, as for example the download effect in hover (i.e. the vertical force that grows on the wing in the opposite direction of the rotor thrust when the rotor wake impinges on it [84], [24], [59]). Also the rotor–rotor interaction in the proximity of the aircraft symmetry plane was investigated and the presence of a negative effect, named fountain effect, was revealed when half–model configuration was used instead of a full–span model [69], [16]. Numerical calculations revealed the same effect when a half–model was used and a symmetry condition was applied on the aircraft symmetry plane [71]. In this regards, in the early 2000s, a 0.25 scaled full–span model was realised for wind tunnel tests in the Ames Research Center 40– by 80–feet wind tunnel. A general description of the test rig was given by McCluer and Johnson [56], while hover tests results were discussed by Young et all. [85]. The continuous improvements in tiltrotor technologies led to the definition of the AgustaWestland AW609 project, also known as Bell–Agusta BA609 (1998).

1.3 The tiltwing concept

As described in the previous section, a tiltrotor is an aircraft that combines the capability to hover, typical of helicopters, with the possibility to flight in cruise at high speed, like propeller driven aircraft. The tiltrotor concept represents a concrete possibility to overcome the main limitations of helicopters and propeller aircraft by matching together the peculiarities of both of them. Thanks to the high versatility of this kind of aircraft [54], [28], the tiltrotor concept represents nowadays a very attractive compromise for the civil industry [72]. However, the hovering performance and the lifting capability of this kind of aircraft are strongly affected by the aerodynamic interaction between wing and rotors. In helicopter flight mode, the presence of the wing under the rotor significantly modifies the rotor wake [16] and thus is responsible for the loss of rotor performance [57]. Moreover, when the rotor wake impinges on the wing surface, a download force of approximately 10 %–15 % of the rotor thrust [57], [24] is generated. To overpass these limitations, in existing tiltrotor (XV–15, V–22 Ospray and BA609) large rotors have been adopted however increasing the aerodynamic interference due to wing–rotor [59] and rotor–rotor [69] interaction. Moreover, large rotors prevent the take–off and landing in aircraft flight mode and lead to important limitations in cruise flight as for example the maximum cruise speed achieved and the operative range which is limited to a relevant fuel consumption.

Since the improvement of the performance in aircraft mode is one of the focus points for future developments of new tiltrotor aircraft, non conventional tiltrotor configurations have to be further investigated [4], [33], in order to preserve the performance in helicopter mode. A possible approach to improve the performance in aircraft mode, i.e. the propulsive efficiency and the cruise speed, is to significantly modify the blade shape [46] by reducing the rotor diameter to get a propeller similar to the ones of propeller aircraft [20]. This solution leads to the tiltwing concept that has been recently adopted for the development the of European project ERICA (Enhanced Rotorcraft Innovative Concept Achievement, [4]). Actually, the tiltwing concept was employed many years before the birth of the ERICA project. In fact, in 1956 the Boeing Vertol Company developed the Vertol Model 76 (VZ–2) that was a VTOL aircraft which belonged to the tiltwing family. However, due to the technical complexity of the aircraft, the project was abandoned after the 1965. The main characteristic of a tiltwing aircraft is represented by the possibility to tilt the external part of the wing with the rotor, minimising the wing surface on which the rotor wake strikes. Good hover performance are preserved in this way and the resulting download force on the aircraft is less than 1 % of the rotor thrust. During the last fourteen years the ERICA concept has been studied under several points of view [29], [6], and it has been the subject of many project founded by the European Community and involving Industries, Research Centers and Universities in Europe. With the goal to study and understand the problems related to this novel aircraft concept, the rotor hub (DART, Development of an Advanced Rotor for Tiltrotor, [13])), the blades (TILTAERO, TILTrotor interactional AEROdynamics, [79]) and (ADYN, Tiltrotor Acoustic DYnamic and Noise, [46]), the tilting wing mechanism (TRISYD, TiltRotor Integrated drive SYstem Development) and the flight control system (ACT–TILT, Active Control Technology for TILTrotor) were investigated for future applications in tiltrotor aircraft. Even if ERICA has been widely studied, many aspects of this non conventional tiltrotor configuration, as same quite basic aspect of the aerodynamics of wing–rotor interaction, could be investigated more deeply for possible future evolutions of the tiltwing concept.

1.4 Present work

The goal of the present research activity is to investigate the aerodynamic interaction between wing and rotor on a high–performance tiltwing aircraft. For this purpose, both experimental and numerical approaches have been used to give a detailed description of the main physical phenomenon related to the interaction between wing and rotor in this kind of aircraft. At the beginning of the activity, a tiltwing aircraft in the same class of ERICA has been defined by means of a statistical approach but not strictly reproducing the ERICA geometry because the aim of the study was more general. Thanks to its non conventional configuration and due to the tiltwing design, the aircraft had small rotors compared with the span of the wing. It follows that close to the aircraft symmetry plane the wing–rotor and rotor–rotor interferences are rather small and thus an half–model configuration can be used instead of the full–span one. For this reason, all the studies of this research make use of an half–model configuration where just one half–wing and one rotor are reproduced. Numerical calculations have been adopted to design both the shape of the blade and the wing. In particular, the aerodynamic blade design has been performed first by means of a multi–objective optimizer which embedded a simple BEMT (Blade Element Momentum Theory) aerodynamic solver. Then high accuracy calculations have been carried out by means of a CFD (Computational Fluid Dynamics) code to verify the blade performance and to refine the shape of the tip. CFD calculations have been used also to define the position of the tilt section along the span of the wing and a first estimation of the wing download force has been done numerically at full–scale. Once the aircraft design was concluded, a 0.25 scaled wind tunnel half–model has been designed and manufactured in order to study the hovering condition in helicopter mode flight. The experimental test rig has been designed to test both different wing configurations (in terms of tilt angles) and different wing positions with respect to the rotor hub. The test rig was used to produce a extensive experimental database which allowed to well describe the flow field and the performance of the aircraft, as well as to offer the possibility to validate CFD codes. Since in hover the interaction between the rotor and the wing is very complex, force measurements may give only partial information about the phenomena related to this non conventional configuration. Therefore, in the present work the hover flight condition has been analysed by means of both force measurements PIV (Particle Image Velocimetry) measurements.

CHAPTER 2

Aircraft design

The performance of a tiltrotor aircraft are strongly affected by the aerodynamic interaction between the wing and the rotors. To study the phenomenon that belongs to this kind of interaction, we defined first a realistic tiltrotor configuration and than we designed its main components at full–scale. In this chapter the main characteristics of the selected aircraft configuration are briefly described. Once the aircraft operating conditions and the design goals are defined, the aerodynamic shape design of its rotor blade and wing are presented.

2.1 Aircraft general sizing

The tiltwing concept is very attractive and promising due to its high versatility with respect to the conventional tiltrotors (XV–15, V–22 Ospray and BA609). Nevertheless, since the possibility to tilt the external part of the wing leads to a significant increase in the aircraft complexity, during the last thirty years only in the ERICA [4] project the tiltwing solution has been adopted. For this reason, in order to define the aircraft geometry and its operating flight conditions, same general data of the whole aircraft has been assumed by defining a tiltwing tiltrotor in the same class of ERICA. The preliminary aircraft geometry has been developed in–house based on the tiltwing concept but not strictly reproducing the ERICA geometry because the aim of the study is more general. Consequently, a typical mission profile for this kind of aircraft has been identified on the point to point service (that is the connection between two urban areas, two oil rigs, ect.) taken from and to vertports. Furthermore, the aircraft has to be able to takeoff and to land both in helicopter and aircraft configurations. The mission requirements included also significant hover and near–hover duration, the capability to maneuver at low speed and the possibility to flight in cruise at high speed. Operational require-

	Helicopter mode	**Aircraft mode**
Passengers	20	22
Crew	2 pilots	3 pilots
Cruise altitude	–	7500 m
Maximum cruise speed	–	170 m/s
Design climb speed	10 m/s	–
Operative rotor speed	560 rpm	430 rpm
Maximum operative range	1200 km	1500 km
Take-off	allowed	allowed
Landing	allowed	allowed

Table 2.1: *Aircraft Operational requirements.*

	VTO	**STO**
Empty weight	7100 kg	7100 kg
Payload (passengers + luggage)	2000 kg	2200 kg
Crew	200 kg	300 kg
Fuel	1600 kg	2000 kg
Gross wieght	10900 kg	11600 kg

Table 2.2: *Aircraft design weights.*

ments and design goals for the full–scale aircraft have been then defined within this framework and are listed in Tab. 2.1 where both the helicopter and aircraft configurations are considered. Aircraft design weights have been estimated by mean of statistical approach [74] and [78] and are reported in Tab. 2.2.

The wing had a span of $15\ m$ and it was defined as the distance between the rotor axles. All the tests (numerical and experimental) of this research make use of an half–model configuration were just one half–wing and one rotor with the nacelle are reproduced, as shown in Figure 2.1 and 2.2. In conventional tiltrotor the rotor radius is slightly lower than the half–wing span, thereby in helicopter mode the fuselage is partially immersed in the rotor wake. It has been observed that for the V–22 Osprey the fuselage contribution to the total aircraft download (that is the component of the aerodynamic force acting on the airframe, parallel to the rotor thrust and directed in the opposite direction) was between the 36 and $42\ \%$ [84], [85]. It follows that the influence of the rotor wake on the fuselage and vice–versa is non–negligible. Therefore, to study the interaction between the rotor and the airframe in a conventional tiltrotor, the fuselage has to be taken into account. On the contrary, since in a tiltwing tiltrotor aircraft the rotor radius is about $50\ \%$ the half–wing span, the interaction between the rotor wake and the fuselage is very low when the aircraft operates in helicopter mode. For this reason the fuselage was not included in the analysed model so that the wing root lied on the aircraft symmetry plane. The wing had a trapezoidal planform and it was untwisted and unswept with NACA 64A221 section. The wing chord c varied linearly from $3\ m$ at the root to $2\ m$ at the tip (i.e. at the nominal extremity of the wing, ideally prolonged up to the rotor axle) and each half–wing was divided in two different components. Following the tiltwing concept, the inner part of the half–wing is fixed while the outer part can be rotated independently. The span of the tilting portion has been defined trying to minimise the drag force that raises on the wing in helicopter mode when the

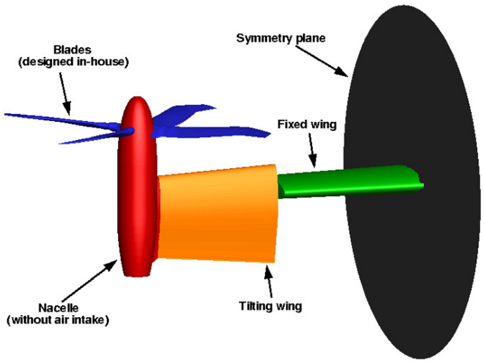

Figure 2.1: *Model layout in helicopter mode.*

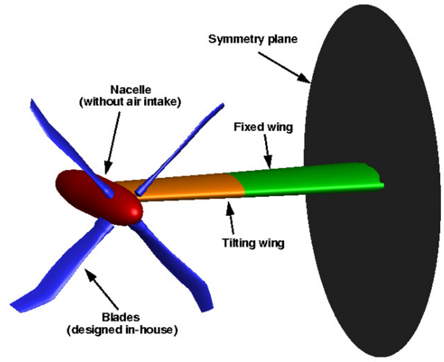

Figure 2.2: *Model layout in aircarft mode.*

rotor wake impinges on it. The nacelle had a maximum diameter of $1\ m$ and a length of $4.5\ m$. Since the present work is based on the study of the phenomenon produced by the wing–rotor aerodynamic interaction, we decided to simplify the model geometry by removing the degree of freedom associated with the shape of the nacelle air intake that was not reproduced. The rotor had 4 non linearly tapered twisted blades with a radius of $3.7\ m$. The rotor blade has been designed in order to fulfill the different requirements due to the very different flight conditions in which the aircraft has to operate and a multi–objective optimisation technique, based on the algorithm NSGA–II [18], has been used to design the blade shape.

2.2 Blade design

The rotor blade aerodynamic design is a very critical task in the project of a tiltrotor aircraft. For an aircraft of this kind, the same propulsive system must be used both in helicopter and aircraft mode flight but the operative conditions are very different in the two modes. The thrust required to the rotors in helicopter flight mode essentially corresponds to the aircraft weight in hover, while the thrust required in aeroplane flight mode is about a fifth of the hover thrust as it corresponds to the aerodynamic drag [57], [24]. Nevertheless, a tiltrotor blade has to give good performance both in hover (and vertical climb) and cruise flight. On the other hand the inflow ratio $\lambda = (V_\infty + v_i)/(\Omega R)$ is quite lower for the helicopter rotor with respect to the aeroplane propeller. Moreover, if the tiltrotor has a non conventional design, as in the present case, because it has the capability to takeoff and land horizontally like an aeroplane, the rotor diameter has to be smaller than conventional ones (like XV–15, V–22 Ospary and BA–609). All these requirements strongly influence the rotor design process and they have to be taken into account during the aerodynamic blade design. The huge difference between operating flight conditions of helicopters and turboprops implies the need of appropriate strategies in tiltrotor blade design. Aside from the chosen design strategy, the proprotor efficiency depends on many parameters. An extensive description of possible design parameters and their influence on proprotors' aerodynamic optimisation have been given by Leishman and Rosen [49].

The design of proprotors is more complex than in the case of helicopter rotor or aeroplane propeller because the design goals have to be selected to achieve a fair balance between helicopter and aeroplane mode flight performance. When more than a one target has to be considered in an optimisation process, two possible strategies can be followed: a single objective optimisation with a weighted objective function that balances the different needs or a multi–objective optimisation that deals with more than one objective. The advantage of the multi–objective optimisation with respect to single–objective optimisation is represented by the vectorial nature of the objective function, where the scalar components of the latter directly correspond to each selected objective [19]. Moreover, since the multi–objective optimisation procedure produces a final solution in terms of Pareto–optimal solutions (a set of optimal non–dominated solutions), the designer can compare the results and select the best compromised optimal solution for the analysed problem. A good example of the application of a multi–objective optimisation procedure for the aerodynamic design of helicopter rotor has been recently described by Le Pape and Beaumier [65].

In general, since the aerodynamic design of a tiltrotor blade can be seen like a shape optimisation problem, it can efficiently approached by means of a genetic algorithm. In the present work the aerodynamic design of the tiltwing tiltrotor blade has been performed with a two–steps optimisation procedure. In the first step, a multi–objective optimisation procedure has been used in the frame of the genetic optimisation technique to define an optimal blade geometry. To reduce power losses due to onset of compressibility effects on the rotor tip and to improve its the performance in aircraft mode, in the second phase of the optimisation procedure a non–linear sweep distribution has been applied to the blade.

2.2.1 Objectives definition and problem formulation

Three different objectives have been selected for the multi–objective optimisation procedure and, for each objective, an aircraft operating condition has been assumed. Following Liu et al. [51], Paisley [64] and McVeigh et al. [58], the performance goals have been set in terms of overall efficiency of the rotor. In particular, according to the main goals of the ERICA rotor system optimisation, the following design points have been chosen:

- Objective 1: Maximisation of the hover Figure of Merit (FM);
- Objective 2: Maximisation of the Propulsive Efficiency (η_{climb}) in vertical climb;
- Objective 3: Maximisation of the Propulsive Efficiency (η_{cruise}) in cruise at high speed.

The FM can be calculated using the simple momentum theory [48], [49] and is defined as the ratio between the ideal power required to hover and the actual power required, that is:

$$\begin{aligned} FM =& \frac{\text{Ideal power required to hover}}{\text{Actual shaft power required}} \\ =& \frac{C_{T_{meas}}^{3/2}}{\sqrt{2} C_{P_{meas}}} < 1, \end{aligned} \tag{2.1}$$

where $C_{T_{meas}}$ is measured value of the thrust coefficient and $C_{P_{meas}}$ is measured value of the power coefficient. Concerning the propulsive efficiency, Leishman and Rosen [49] suggested for a tiltrotor aircraft the same definition adopted for conventional propellers. The propulsive efficiency can be expressed as follows:

$$\begin{aligned}\eta =& \frac{\text{Ideal propulsive power}}{\text{Actual shaft power required}}\\ =& \frac{T_{meas}V_{\infty}}{P_{meas}},\end{aligned} \tag{2.2}$$

where T_{meas} and P_{meas} are the measured values of the thrust and the propulsive power while V_{∞} represents the climb or cruise speed of the aircraft.

The first and the second objectives are related to the aircraft operating in helicopter configuration, while the third objective concerns the aeroplane flight mode. The previous points represent the scalar components of the objective function of the multi–objective optimisation process. The optimisation procedure has been carried out on three different objectives corresponding to three different flight conditions, shown in Table 2.3. To reduce the complexity of the optimisation problem it was decided to fix the rotational speed Ω of each operating condition by comparison with existing tiltrotors (XV–15, [54], V–22, [57], ERICA, [4]). For the same reason, we also decided to impose both the internal radius R_i, that is $0.8\ m$, and the external radius R_o, that is $3.7\ m$, while the number of blades for each rotor was fixed to 4. Due to the half–tilt wing configuration, the aerodynamic rotor–wing interaction in hover is so small [4] that it has been neglected in the present optimisation process. The absence of relevant interaction effects has then been confirmed by numerical calculations and experiments (see Chapter 2). It follows that the required thrust for the hovering flight $T_{r,1}$ can be assumed to be equal to half the aircraft maximum takeoff weight. On the other hand, when the aircraft is climbing in the helicopter mode or is flying in the aircraft mode, the wing drag and the fuselage drag have to be taken into account in order to evaluate accurately the required thrust ($T_{r,2}$ and $T_{r,3}$). The wing–fuselage drag D^{wf}, that is

	Flight Condition 1 (Helicopter)	
Rotor speed	Ω	560 rpm
Altitude	h	0 m
Maximum takeoff weight	W_{MTOW}	10900 kg
Required thrust for hover	$T_{r,1} = W_{MTOW}/2$	53464 N
	Flight Condition 2 (Helicopter)	
Rotor speed	Ω	560 rpm
Altitude	h	0 m
Maximum takeoff weight	W_{MTOW}	10900 kg
Climb speed	V_{∞}	10 m/s
Wing–Fuselage Drag	D^{wf}	3215 N
Required thrust for climb	$T_{r,2} = W_{MTOW}/2 + D^{wf}/2$	55072 N
	Flight Condition 3 (Aeroplane)	
Rotor speed	Ω	430 rpm
Altitude	h	7500 m
Cruise speed	V_{∞}	170 m/s
Wing–Fuselage Drag	D^{wf}	22577 N
Required thrust for cruise	$T_{r,3} = D^{wf}/2$	11288 N

Table 2.3: *Flight conditions for the optimisation procedure.*

shown in Table 2.3 and is related to the wing surface $S^w = 35\ m^2$, has been calculated by estimating the wing–fuselage drag coefficient C_D^{wf}. For the second flight condition (i.e. the helicopter in vertical climb) we estimated a C_D^{wf} of 1.5 [78], while for the third flight condition (i.e. the aircraft in cruise at high speed) we assumed a C_D^{wf} of 0.08 [74].

The blade shape is the result of a multi–variable, multi–objective constrained optimisation based on a controlled elitist genetic algorithm founded on NSGA–II by Deb [18], [19], that finds minima of multicomponent objective function using genetic algorithm. At each iteration, the solver combines the previous population with an offspring population that is the result of binary crowded tournament selection, recombination and mutation operators. The resultant population, that is a combination of parent and offspring populations, is then sorted according to a fast nondomination procedure and members of the new population are selected with a fast crowded distance estimation procedure that uses the crowded–comparison operator (a comprehensive description of the NSGA–II algorithm can be found in [18]). An implementation of the NSGA–II is included in the Global optimisation Toolbox [55] of Matlab® and it has been used in the present work.

The mathematical formulation of the constrained multi–objective optimisation problem can be written as follows:

Minimise:

$$\mathbf{F}(\mathbf{x}) = (f_m(\mathbf{x}))^T, \qquad \text{m=1,...,M,} \tag{2.3}$$

subject to:

$$\begin{aligned} &x_i^{LB} \leq x_i \leq x_i^{UB}, && \text{i = 1,...,N} \\ &g_j(\mathbf{x}) \leq 0.0, && \text{i = 1,...,J,} \\ &h_k(\mathbf{x}) = 0.0, && \text{j = 1,...,K,} \end{aligned}$$

where $\mathbf{x} = (x_1, \ldots, x_N)^T$ is the design variables array (or individual) and $\mathbf{F}(\mathbf{x})$ is the objective function that is composed by M scalar quantities, where M is the number of selected objectives. The design variables space $\mathbb{D}$ is clearly defined by imposing that each design variable x_i can take a value that is restricted between a lower x_i^{LB} and upper x_i^{UB} bound. Once the design variables array $\mathbf{x}$ meets the design bounds, the solution is a feasible solution inside the feasible solutions space $\mathbb{S}$ if the design criteria, expressed by the linear inequality $g_j(\mathbf{x})$ and equality $h_k(\mathbf{x})$ constraint functions, are satisfied. In the present analysis, the blade design variables array $\mathbf{x}$ is defined as follows:

$$\mathbf{x} = (c_1, \ldots, c_9, \theta_1, \ldots, \theta_9, ASI_1, \ldots, ASI_9)^T, \tag{2.4}$$

and it includes the blade span–wise distribution of chord length c_i, twist angle θ_i and airfoil shape index ASI$_i$. In particular, 9 sections have been identified along the blade span for a total number of 27 variables. The twist angle θ_i is defined as the angle between the hub plane and the section chord (positive nose up) with null collective pitch. Each section has been rotated around a reference axis passing through 0.25% of local chord (this axis corresponds to the feathering axis). The goal of the optimisation problem has been defined as the maximisation of 3 objectives expressed in terms of 3 efficiency parameters (which vary between 0 and 1). Since the NSGA–II algorithm used in the present work finds minima of multicomponent objective function, the objective function $\mathbf{F}(\mathbf{x})$ has been written subtracting each scalar component FM, η_{climb} and η_{cruise} from 1 (duality principle, [17]). All design variables have been limited by a set of prescribed lower and upper bounds. Linear inequality constraints limit the maximum twist angle variations and chord rate of change between one section and the following one. To avoid abrupt changes in chord value near the root of the blade, the chord of the first blade section has been linked to the chord of the second section by a linear equality constraint. The same has been done for last two sections at the blade tip.

2.2.2 Multi–objective optimisation procedure

Every time an individual $\mathbf{x}$ of a certain population P^t has to be evaluated during the optimisation procedure, each scalar component of the objective function $\mathbf{F}(\mathbf{x})$ is computed by an aerodynamic solver, based on the BEMT (Blade Element Momentum Theory, see Appendix B for a brief description of the BEMT solver), as recommended by Leishman and Rosen [49] because it is mathematically parsimonious and agrees reasonably well with experimental data [51], [34]. This very simple model [48] is based on the blade decomposition in a span–wise series of sectional blade elements (BE) and on the corresponding rotor disk decomposition in a series of concentric annuli. For each blade element a 2D aerofoil aerodynamics approach is coupled, by means of a recursive approach, with the induced velocity obtained by the annular version of the disk actuator model (Momentum Theory, MT). Both the axial and the azimuthal (i.e. the swirl effect, [30]) components of the induced velocity are taken into account. At blade tip, were the annular theory underestimates the induced velocity, the approximate Prandtl's tip loss function is employed to account for the wake inflow effects [31]. The blade global loads are then computed as sum of the different blade element contributions. Since in the objective function rotor performance (FM, η_{climb} and η_{cruise}) have to be evaluated in different flight conditions, aerodynamic characteristics of airfoil sections have been previously stored in tables for a wide range of angles of attack, Reynolds and Mach numbers. The aerodynamic solver extracts interpolated values of lift coefficient C_L drag coefficient C_D and pitching moment coefficient C_m, for every specified value of angle of attack, Reynolds and Mach number in the stored range. The database of the aerodynamic characteristics of airfoil sections used for the analyses have been generated collecting together wind tunnel data (when present in literature, especially for NACA airfoils we referred to Abbott and Doenhoff [1]) and CFD results from two–dimensional steady simulations. For the m–th flight condition, the aerodynamic solver yields the estimated thrust T_m and power P_m given by the selected blade.

To compute the performance of rotor blades operating in one flight condition, it is first necessary to calculate the corresponding trim condition of the rotor (in terms of pitch blade angle θ_0 [48]). Once the blade shape and the flight condition have been fixed, the trim condition is then computed by the aerodynamic solver. Since the calculation of the trim condition can be fundamental to the evaluation of the blade performance for a given flight condition, the trim pitch angle is computed by the aerodynamic solver in order to satisfy the thrust required constraint $T_{r,m}$. The problem can be summarised as follows:

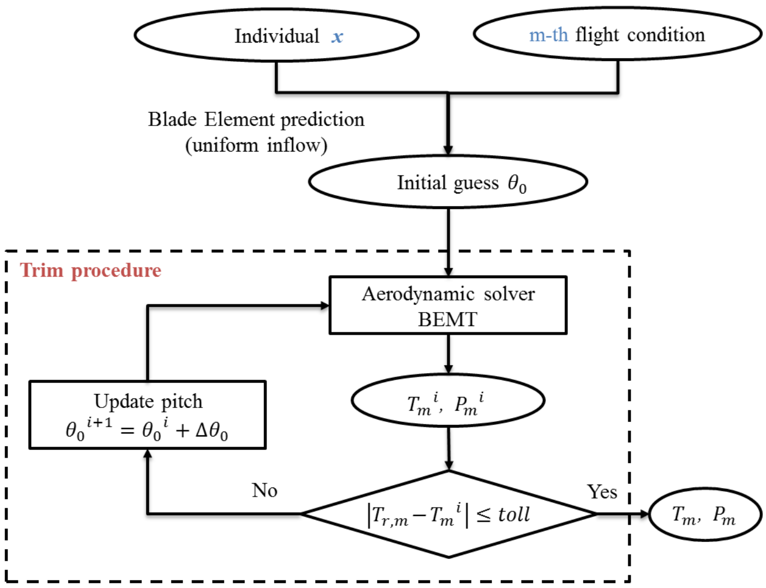

Figure 2.3: *Rotor trim procedure for a selected flight condition.*

Find:

$$\theta_0, \qquad \text{m=1,...,M,} \tag{2.5}$$

such that:

$$T_m\left(\theta_0\right) - T_{r,m} = 0.$$

The link between the pitch angle θ_0 and the thrust T given by a rotor is typically non–linear, hence Equation 2.5 is non–linear and it has to be solved in a suitable manner. As shown by [48], the trim problem for an hovering rotor can be efficiently approached by an iterative calculation. Every time an individual is evaluated by the optimiser, the trim problem has to be solved 3 times, one for each flight condition. Figure 2.3 shows trim procedure flow chart.

In order to manage a variables array that includes both real (the chord and the twist) and integer (the airfoil shape index) variables, same modifications of the tools of the Global optimisation Toolbox ([55]) have been done. Furthermore, appropriate crossover and mutation functions have been written in–house to improve the method efficiency. A scattered crossover operator has been used on pairs of parents, as shown by [61], creating a random index vector to exchange the corresponding genes from one parent to the other and vice–versa, to form pairs of children. Sometimes, however, the crossover operator may give one or more offspring outside of the feasible solutions space $\mathbb{S}$, [62]. If this problem arises, thanks to convex solution spaces characteristics, a whole arithmetical crossover operator is used instead of scattered crossover operator. Individuals that are not recombined by the crossover operator (this number depends on the crossover fraction, chosen equal to 0.7 in the present work) are selected for mutation. Instead of the classical uniform mutation operator, which selects a random gene k of a given chromosome $\mathbf{x}^t = (x_1, \ldots, x_k, \ldots, x_N)^T$ to yield a new chromosome $\mathbf{x}^{t+1} = (x_1, \ldots, x_k', \ldots, x_N)^T$ with a new gene x_k' that assumes a random value (uniform probability distribution) inside the range defined by lower x_k^{LB} and upper x_k^{UB}

bound, we implemented an adaptive variant of the non–uniform mutation operator developed by Michalewicz and Janikow [62]. In fact, since the non–uniform mutation operator prefers parameter values in the centre of the feasible solutions space $\mathbb{S}$, when the optimal solution is located near the boundaries of $\mathbb{S}$ the optimizer can have some difficulties to easily find the optimal solution. To avoid this problem, which may results in an increase of the computational time, the adaptive non–uniform mutation operator proposed by Neubauer [63] has been chosen. In particular, the implemented mutation scheme selects one or more genes (labelled with the subscript k) of a chromosome $\mathbf{x}^t$ from the parent population P^t and returns a new chromosome $\mathbf{x}^{t+1}$ in which the mutated genes are computed as follows:

$$x'_k = x_k + \delta_k\left(t\right), \tag{2.6}$$

where $\delta_k(t)$ is a random variation and is computed as follows:

$$\delta_k\left(t\right) = \begin{cases} \left(x_k^{UB} - x_k\right) \cdot \left(1 - \left[z_k\right]^{\gamma(t)}\right), & \text{with probability } q_k, \\ \left(x_k^{LB} - x_k\right) \cdot \left(1 - \left[z_k\right]^{\gamma(t)}\right), & \text{with probability } 1 - q_k. \end{cases} \tag{2.7}$$

In Equation 2.7, the probability function proposed by Neubauer is defined as:

$$q_k = \frac{x_k - x_k^{LB}}{x_k^{UB} - x_k^{LB}}, \tag{2.8}$$

while the parameter z_k is a random number that varies between 0 and 1 (uniform probability distribution) and its exponent is:

$$\gamma\left(t\right) = \left(1 - \frac{t}{t_{max}}\right)^{\beta}, \tag{2.9}$$

where t is the index of the actual generation, t_{max} corresponds to the maximum number of generations analysed and β is a positive exogenous strategy parameter (in the present case $\beta = 5$).

In order to have good results in relatively short computational time, it has been decided to use a population size of 70 individuals per generation. To start the optimisation procedure, an initial population P_0 is required. [70] have shown that, if the genetic information present in the initial population is not enough, the genetic algorithm can converge prematurely to a local optimal solution. Such problem can be fixed making use of a well–distributed initial population. [19] suggests to include in the initial population some feasible individuals already known. For these reasons, before starting the multi–objective optimisation, single objective constrained optimisations, that finds minima of scalar objective function using genetic algorithm, have been carried out for each objective. The single objective constrained optimisations have been performed with the same blade design variables array $\mathbf{x}$ of the multi–objective optimisation procedure. Also the linear constraint functions $g_j(\mathbf{x})$ (inequality) and $h_k(\mathbf{x})$ (equality) and the lower x^{LB} and upper x^{UB} bound are kept equal to the multi–objective optimisation. Then, the initial population P_0 of the multi–objective optimisation has been created selecting the same number of best individuals from each final population of single objective optimisations. Figure 2.4 shows the optimisation procedure flow chart.

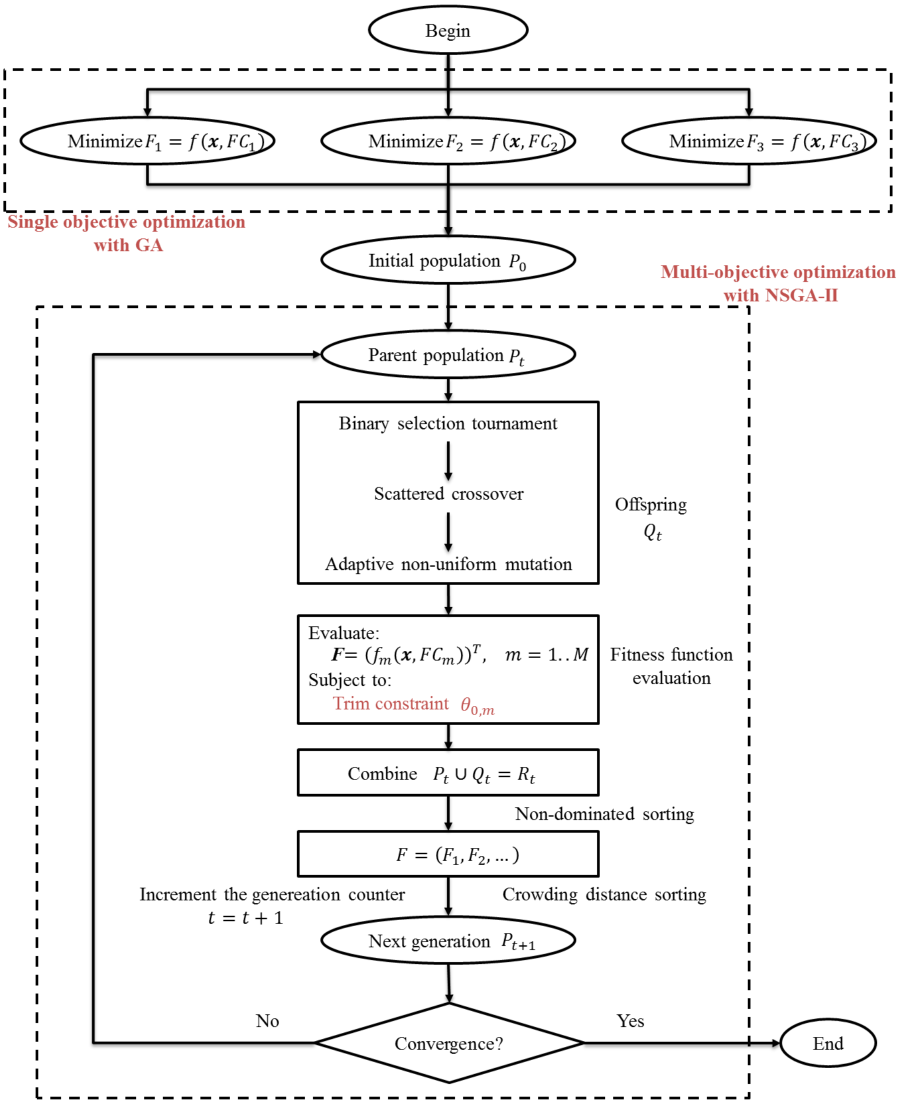

Figure 2.4: *Rotor optimisation procedure flow chart.*

2.2.3 Multi–objective optimisation results

The multi–objective optimisation procedure was ended after 400 iterations (28070 individuals have been evaluated) and the Pareto–optimal set resulted to be composed by 25 optimal individuals. In Figure 2.5 the Pareto–optimal front has been shown for each pair of objectives. Also the initial population P_0 has been reported in Figure 2.5 to show the improvements in terms of objective values due to the multi–objective optimisation procedure. As it can be seen in Figure 2.5a, the couple $f_1(\mathbf{x})$ and $f_2(\mathbf{x})$ represents slightly conflicting objectives while, on the other hand, they are both strongly conflicting with $f_3(\mathbf{x})$ (Figure 2.5b and Figure 2.5c). The chosen blade, indicated with a red circle in Figure 2.5, is apparently the best compromise solution between all the solutions included in the Pareto–optimal set because it shows good performance in all flight conditions. In Table 2.4 a summary of the predicted performance of the optimal blade

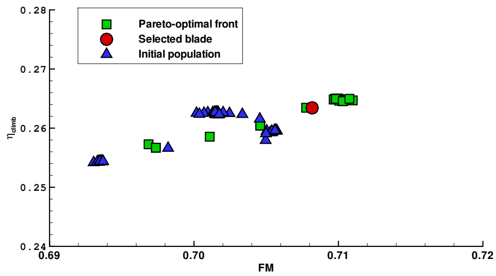

(a) *FM versus η_{climb}*

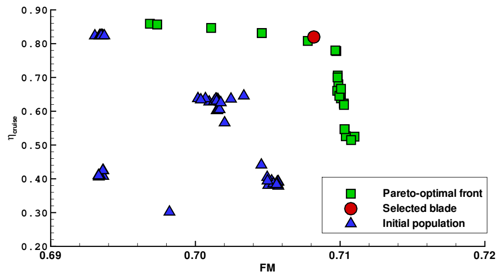

(b) *FM versus η_{cruise}*

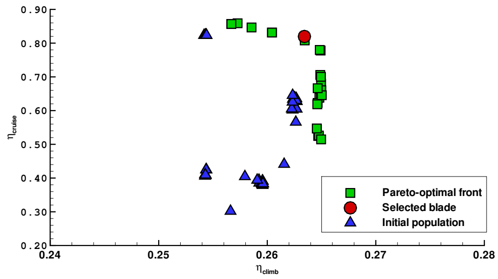

(c) *η_{climb} versus η_{cruise}*

Figure 2.5: *Pareto–front in the feasible solutions space $\mathbb{S}$. Comparison between Pareto–optimal front and initial population (created by single–objective genetic algorithm analyses).*

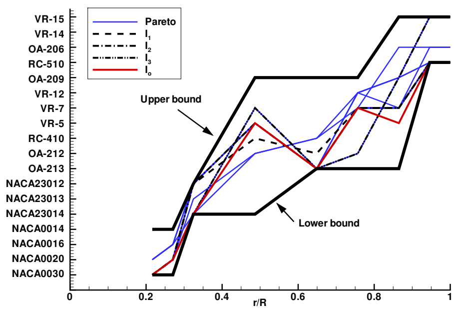

(a) *Airfoil shape index*

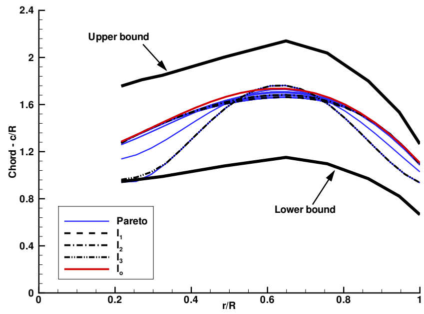

(b) *Chord*

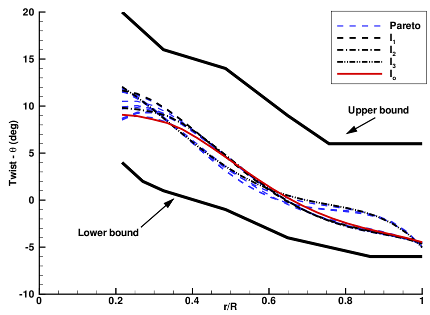

(c) *Twist*

Figure 2.6: *Optimised airfoil index, chord and twist distribution using multi–objective genetic algorithm. Comparison between individual I_1, I_2 and I_3 and selected individual I_o (from pareto–optimal front).*

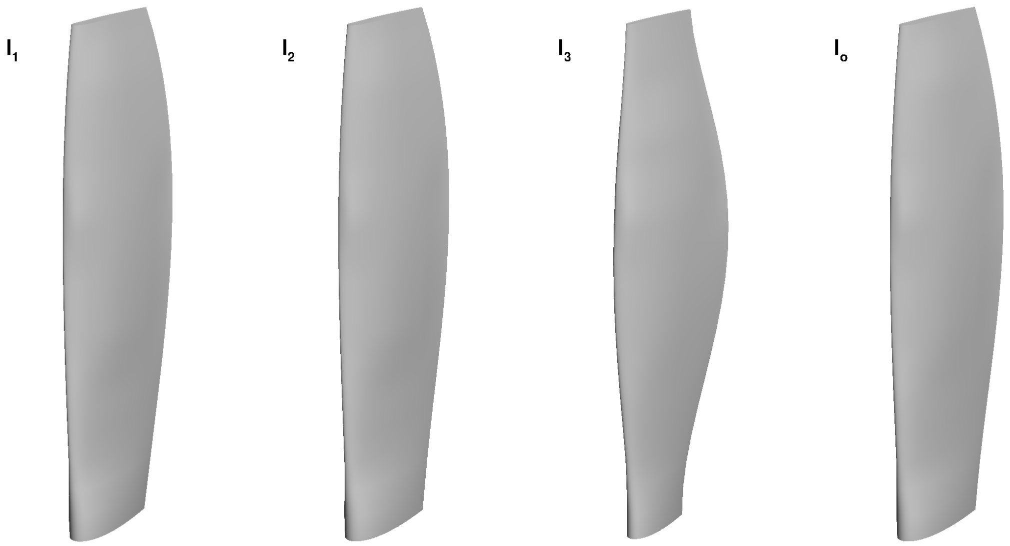

Figure 2.7: *Blade geometry of individuals I_1, I_2, I_3 and I_o from multi–objective genetic algorithm.*

		Flight Condition 1 **(Helicopter)**		
C_t	C_p	σ	θ_0 [deg]	FM
0.0215	0.00316	0.194	13.7	0.709
		Flight Condition 2 **(Helicopter)**		
C_t	C_p	σ	θ_0 [deg]	η_{climb}
0.0222	0.00388	0.194	15.9	0.263
		Flight Condition 3 **(Aeroplane)**		
C_t	C_p	σ	θ_0 [deg]	η_{cruise}
0.0169	0.0210	0.194	58.3	0.820

Table 2.4: *Predicted performance in helicopter and aircraft configurations of selected optimal blade I_o from multi–objective optimisation procedure.*

Section	r/R	c/R	θ [deg]	Airfoil
1	0.216	0.131	9.061	NACA 0030
2	0.270	0.133	8.351	NACA 0020
3	0.324	0.144	8.324	NACA 23014
4	0.487	0.168	5.217	VR–5
5	0.649	0.179	−0.005	OA–213
6	0.757	0.155	−2.265	VR–7
7	0.865	0.154	−2.849	VR–5
8	0.946	0.131	−3.540	RC–510
9	1.000	0.108	−4.759	RC–510

Table 2.5: *Geometric parameters of the individual, I_o.*

I_o has been reported for each flight condition considered during the optimisation process. In Figure 2.7 the planform of the selected optimal blade I_o is compared with the planform of the individuals I_1, I_2 and I_3 included in the Pareto–optimal front and minimising objective 1, 2 and 3 respectively. Figure 2.6 shows the resulting distribution of the optimisation variable distributions for all the individuals included in the Pareto–

optimal front. The data of the selected optimal blade I_o are also listed in Table 2.5.

It is first apparent that the blade I_1 (the best one for the hovering flight condition) has a planform almost rectangular, similar to a typical helicopter blade. On the other hand, the blade I_3 (that is the best one for the cruise flight condition) has a sensibly more elliptic and twisted shape, resembling a typical propeller blade. Looking at the load curves in hovering condition in helicopter mode, as shown in Figure 2.8, it is clear that the blades I_o, I_1 and I_2 have load distributions that are close to the ideal linear law for hovering rotor [48], while the blade I_3 has a non–optimal behaviour. However, looking at the aeroplane cruise flight condition, as reported in Figure 2.9, it can be observed that the blade I_3 has a regular load distribution resembling the shape of optimal distribution for propellers (as shown by Goldstein [31]). As for the other three solutions, only the blade I_0 has a reasonably similar behaviour while the blades I_1 and I_2 are clearly stalled toward the extremities. All the four presented solutions have the rotor inner part that does not give a positive contribution in aeroplane mode. In fact, the need to have also this part collaborating (and therefore not stalled) in the helicopter mode (where much more traction is required) leads to a blade twist quite lower respect to the need of a propeller, so producing negative incidences in aeroplane mode. On the other hand, at least for blades I_3 and I_o, the outer part of the rotor compensates adequately so that the global efficiency is nevertheless high. It should be noted that, since the individual I_1, I_2 and I_3 are different, they have different pitch trim angles. For the hovering flight, the individual I_1 and I_2 have the same pitch angle ($13.9°$) that is very close to the one of the selected optimal blade I_0 while the individual I_3 has a trim angle of $15.2°$. On the contrary, in cruise flight at high speed, the individual I_1 and I_2 have pitch trim angles that are respectively $66.6°$ and $64.7°$. In this condition, the individual I_3 is the only one which shows a trim angle ($57.5°$) similar to the blade I_0.

Figures from 2.10 to 2.12 show the variation of thrust, power and propulsive efficiency versus tip speed ration for increasing values of blade pitch angle in cruise flight condition for the selected individual I_o. It can be observed that, ones the the pitch angle

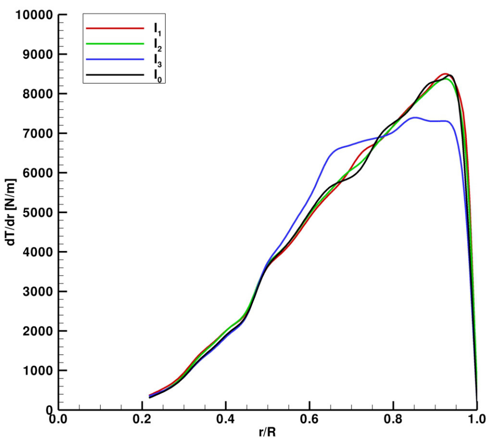

Figure 2.8: *Span–wise distribution of thrust in hover flight condition. Comparison between individual I_1, I_2, I_3 and selected individual I_o (from Pareto–optimal front).*

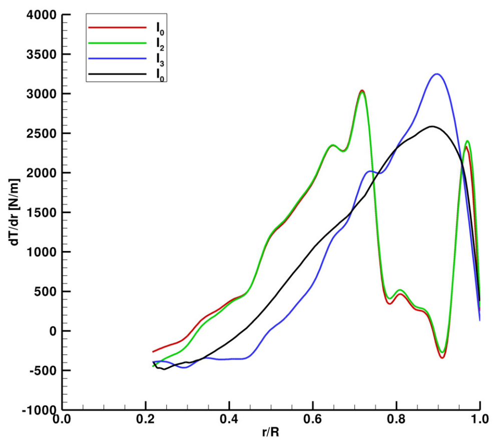

Figure 2.9: *Span–wise distribution of thrust in cruise flight condition. Comparison between individual I_1, I_2, I_3 and selected individual I_o (from Pareto–optimal front).*

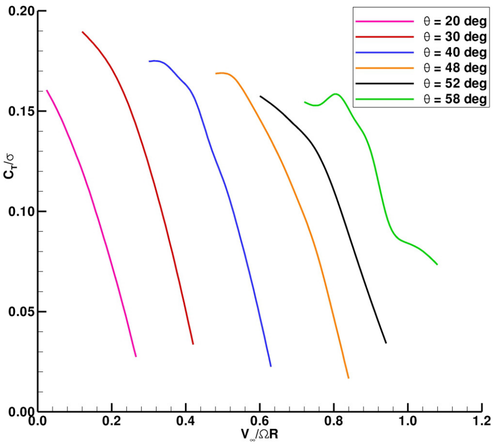

Figure 2.10: *Prediction of C_T/σ as function of $V_\infty/\Omega R$ for various pitch angles.*

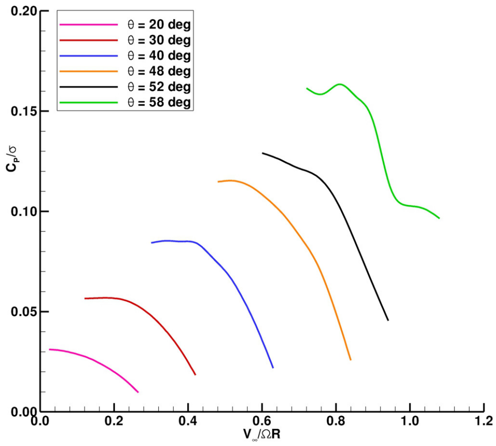

Figure 2.11: *Prediction of C_P/σ as function of $V_\infty/\Omega R$ for various pitch angles.*

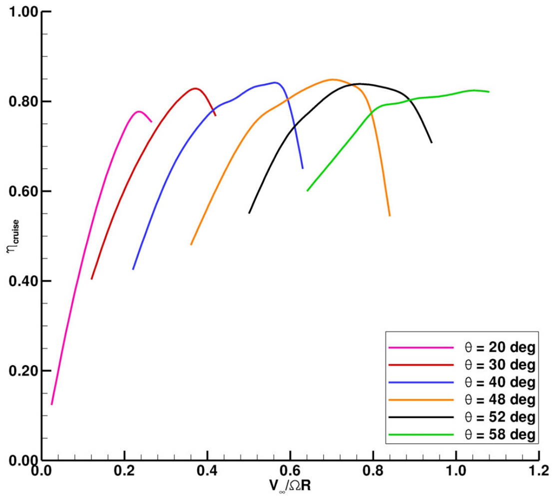

Figure 2.12: *Prediction of η_{cruise} as function of $V_\infty/\Omega R$ for various pitch angles.*

is fixed, when the airspeed decreases the blade is stalled and it requires a significant amount of power to get low values of thrust. Instead increasing the airspeed the required power decrease because the flow separation on the blade diminishes, hence η_{cruise} tends to increase. As noted by Leishman and Rosen [49], for high values of airspeed the blade operates in high transonic flow and the progressive growing of compressibility effects give flow separation at the blade tip behind.

2.2.4 Tip refinement

For a given rotational tip speed, by increasing the flight speed of a propeller, the helical Mach number increases and thus the compressibility effects arise on the blade. Thus, a progressive degradation of propeller performance becomes evident the higher the flight speed. Losses in propeller performance at high flight speed may depend on the airfoil sections and on the shape of the outer part of the blade. The most effective way to reduce power losses due to onset of compressibility effects is to sweep the blade tip following the normal Mach number criterion. Due to the fact that BEMT approach adopted in the optimisation process is not capable to account for the sweep angle effects, this correction has been applied a posteriori to the selected optimal blade I_o produced by the multi–objective optimizer. Hence the possible efficiency improvement had to be estimated by means of an high accuracy method.

The sweep angle distribution of the outer part of the blade has been calculated applying the normal Mach number criterion, which is similar to the method used for the sweptback wings [75]. This criterion has been applied taking into account the cruise flight condition. The blade has been swept without modifying the airfoil shape, the chord and the twist of local sections that have been previously defined by the multi–objective optimisation procedure. The backwards displacement of the outer sections of the blade moves the aerodynamic centre of that sections behind the feathering axis. To keep the aerodynamic torsional moment limited and independent from the blade pitch angle variation, inboard blade sections were swept upwards. The nondimensional position $\Delta\zeta/R$ (positive in upward direction, see Figure 2.13) of each section and the

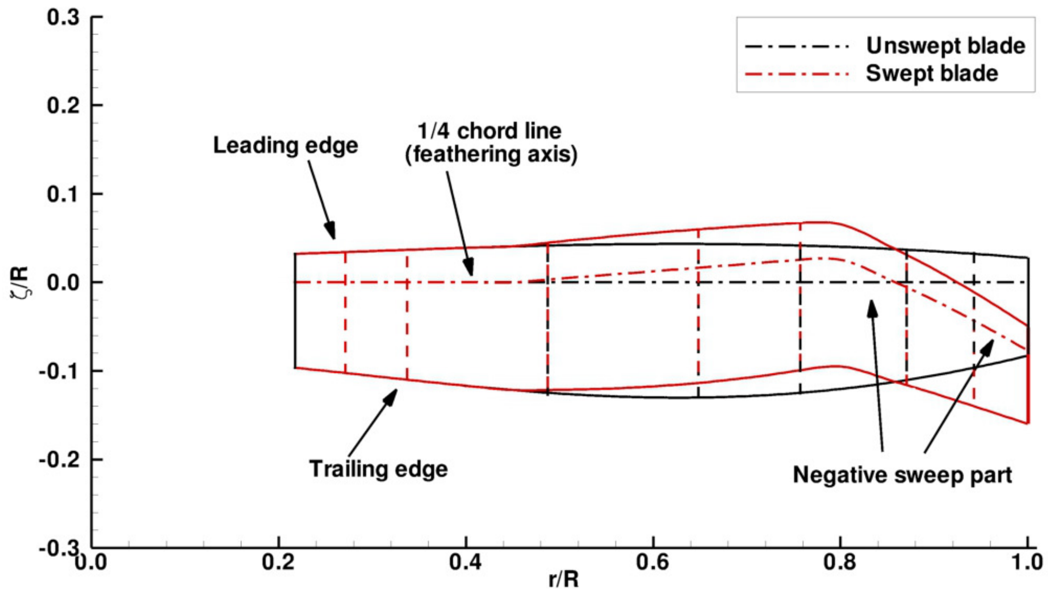

Figure 2.13: *Selected optimal blade I_o planform. Comparison between the original planform given by the multi–objective optimizer and the modified shape for compressibility losses.*

Section	r/R	c/R	θ (deg)	$\Delta\zeta/R$	Λ (deg)
1	0.216	0.131	9.061	0.000	0.0
2	0.270	0.133	8.351	0.000	0.0
3	0.324	0.144	8.324	0.000	0.0
4	0.487	0.168	5.217	0.003	−4.2
5	0.649	0.179	−0.005	0.017	−4.4
6	0.757	0.155	−2.265	0.025	−4.7
7	0.865	0.154	−2.849	−0.003	23.9
8	0.946	0.131	−3.540	−0.046	26.0
9	1.000	0.108	−4.759	−0.077	27.3

Table 2.6: *Geometric characteristics of the selected optimal blade I_o geometry in its optimised version (swept).*

corresponding local sweep angle Λ are reported in Table 2.6. The comparisons between the planforms and the $0.25\ \%$ chord curves of both the original blade I_o (unswept) and its optimised version (swept) are shown in Figure 2.13.

Since the BEMT solver that has been coupled with the multi–objective optimizer is not capable to account for the sweep angle effects, both the swept and the unswept blades have been evaluated with a compressible Navier–Stokes solver. Numerical simulations have been performed with the CFD code ROSITA (Rotorcraft Software ITAly) developed at Politecnico of Milano (see Appendix A for a brief description of the ROSITA solver). Thanks to the circumferential periodicity of the rotor geometry and its wake in the three flight conditions considered in this analysis (i.e. hovering and axial flight conditions), some hypotheses that allows to simplify the problem can be introduced. In particular, the simulations were carried out only on a $90°$ cylindrical sector around a single blade with periodic boundary conditions on the sides. In this way, the control volume that would contains the whole rotor can be reduced to one fourth. Thanks to the Chimera technique, the final computational mesh is composed of 2 different structured multi–block grids, representing the first the blade and the flow region near it and the second the background flow region in which the blade is located. The unswept and swept blade grids have been designed with the ICEM CFD software (by ANSYS) while the background grid has been realised with a Fortran code designed to generate grids of cylinder sector. Calculations have been carried out with a periodic O–H farfield mesh (the external grid), with the outer boundaries located $4\ R$ away from the blade tip in the span–wise direction, $8\ R$ above and $15\ R$ below the rotor plane in vertical direction. The farfield grid contains a total of about 1.2×10^6 cells in a single block grid and is the same for both the unswept and swept blade calculations. The

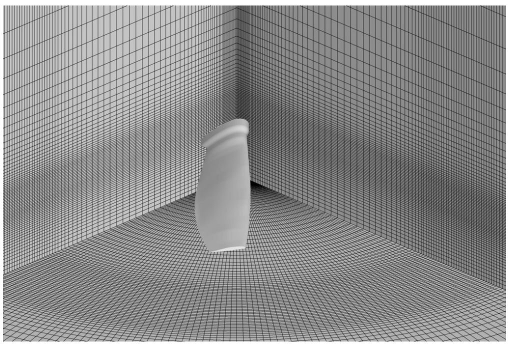

Figure 2.14: *Straight blade in the farfield grid.*

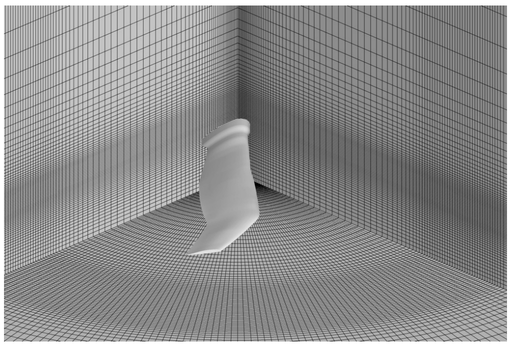

Figure 2.15: *Swept blade in the farfield grid.*

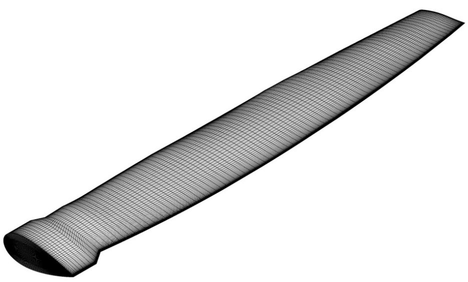

Figure 2.16: *Straight blade skin mesh.*

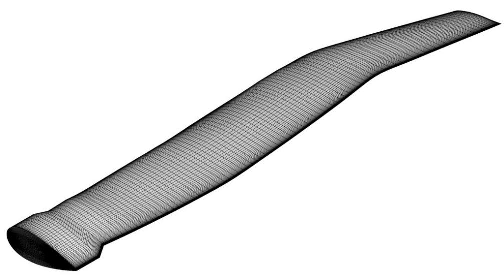

Figure 2.17: *Swept blade skin mesh.*

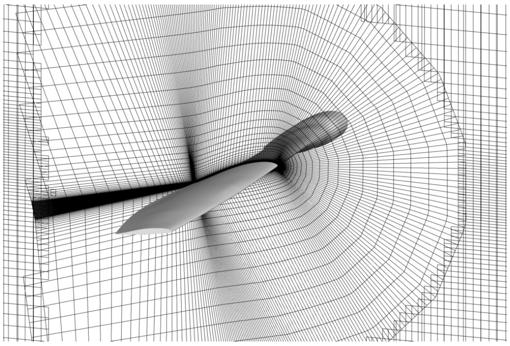

Figure 2.18: *Straight blade C–O grid topology.*

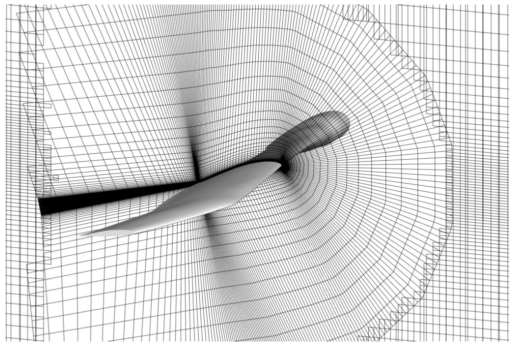

Figure 2.19: *Swept blade C–O grid topology.*

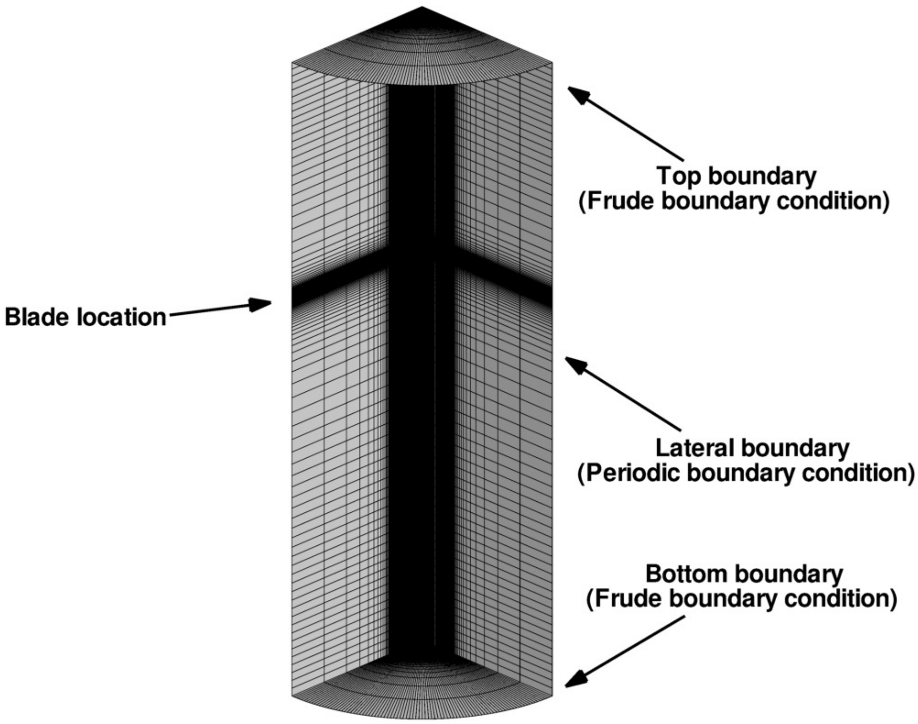

Figure 2.20: *Farfield* $90°$ *cylindrical sector O–H grid topology.*

sketches representing the blades (unswept and swept) inside the farfield grid are reported in Figure 2.14 and 2.15. For both blades, a C–O grid meshing topology has been used in order to limit the global grid size and to ensure a very good nodes distribution and orthogonality in the proximity of the blade surface. In both cases, the first layer of elements near the blade surface has a height of 4×10^{-6} R which corresponds to the value of the dimensionless wall distance (y+). This value has been based on the flow conditions (i.e. the Reynolds and Mach number) at the blade tip. The blade has been fairly well discretised in terms of nodes distribution along the chord and the normal surface directions (a hyperbolic law has been adopted in both directions), but also in the span–wise direction, especially near the blade root and tip sections. In Figure 2.16 and 2.17 the skin meshes of the unswept and swept blade are shown. The blade meshes (inner grid) have the outer boundary located at $1.5\ R$ from the tip in the span–wise direction and extend vertically by $2\ R$, having similar spatial resolution to the first one, as shown in Figure 2.18 and 2.19. The blade grids contains a total of about $3.2\ \times\ 10^6$ of cells distributed in 8 blocks. Efficient computations for hovering flight condition can be carried out imposing the farfield Froude boundary conditions [10] on the top and bottom sections of the farfield grid, while classical periodic boundary conditions are set on the two periodic faces on the farfield grid sides, Figure 2.20.

Simulations were carried out both for the hovering flight condition in helicopter mode and for the cruise flight condition in aircraft configuration (see Table 2.3 for details). The blade tip Mach number M_{Tip} was fixed to 0.64 for the hovering flight and to 0.54 for the cruise flight. Since the rotor rotational speed was fixed, in order to change the rotor thrust, only a collective pitch command was given to the blades. Also the Reynolds number based on the rotor radius and on the rotor tip speed was fixed during the tests and was equal to $5.5\ \times\ 10^7$ in the hover case and to $2.2\ \times\ 10^7$ in the cruise flight.

Figure 2.21 and 2.22 show the comparison between the CFD results achieved for the swept and the unswept blade in hover and cruise flight conditions respectively. The rotor performance, expressed in terms of FM and η_{cruise}, have been shown as function of C_T/σ. In both operating conditions the swept blade exhibits a small but not completely negligible increase of the rotor performance with respect to the unswept blade. In particular, at the design point in hover ($C_T\ =\ 0.0215$), the FM of the swept blade is 0.720, that is $1.55\ \%$ higher than the value of FM given by the unswept blade. The difference between the hover performance of the unswept and swept blades can be justified by the presence of a sort of anhedral effect [48], [65] in the swept blade due to the introduction of the sweep angle distribution along the radius. In fact, the geometrical configuration of the swept blade slightly modifies the position of the tip vortex emission. Therefore the blade tip vortex is moved below the rotor plane and it is convected downstream far from the lower surface of the blade. In Figures from 2.23 to 2.28 the contours of the Q–criterion [36] have been reported for several azimuthal blade positions for both the unswept and swept blades. The anhedral effect can

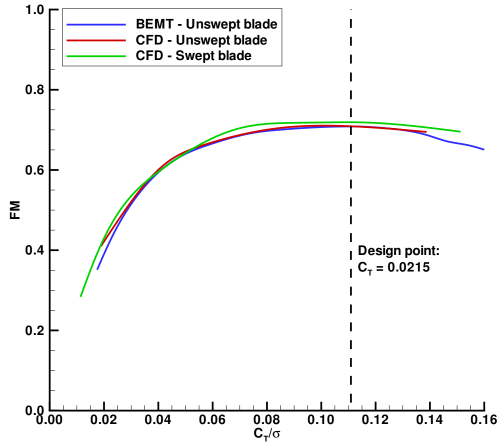

Figure 2.21: *Comparison between unswept and swept configuration of selected optimal blade I_o: FM as function of C_T/σ in hovering flight.*

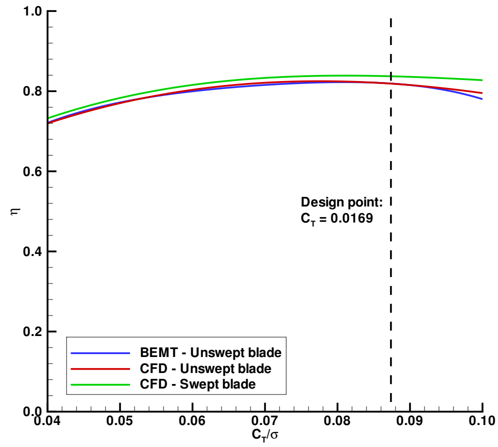

Figure 2.22: *Comparison between unswept and swept configuration of selected optimal blade I_o: η_{cruise} as function of C_T/σ in cruise flight.*

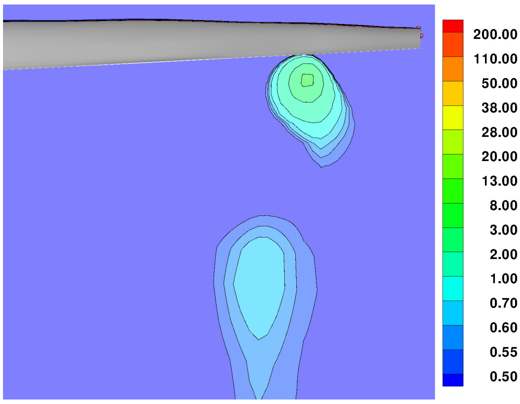

Figure 2.23: *Unswept blade in hovering flight at $\theta_0 = 14°$: Q–criterion contours on a radial plane for a phase of $\psi = 0°$*

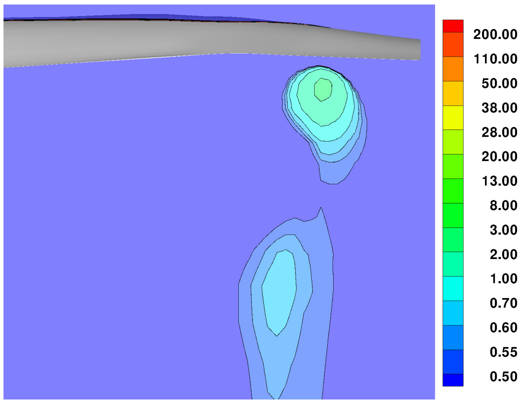

Figure 2.24: *Swept blade in hovering flight at $\theta_0 = 14°$: Q–criterion contours on a radial plane for a phase of $\psi = 0°$*

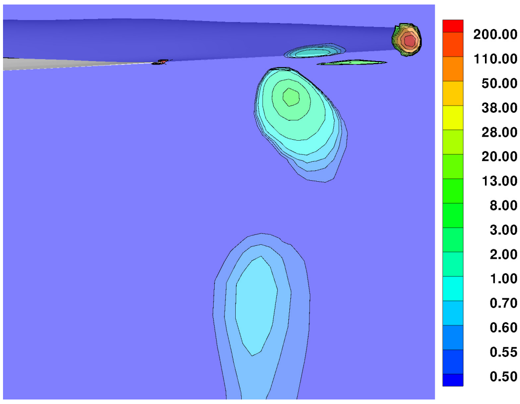

Figure 2.25: *Unswept blade in hovering flight at $\theta_0 = 14°$: Q–criterion contours on a radial plane for a phase of $\psi = 10°$*

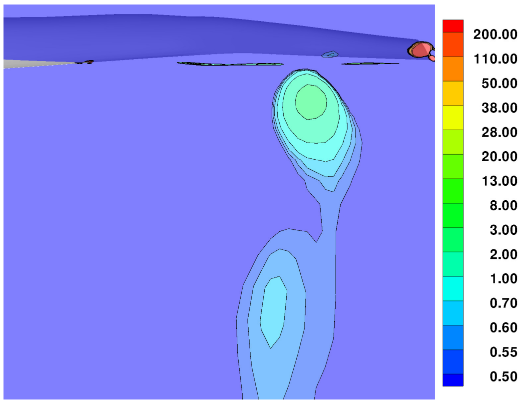

Figure 2.26: *Swept blade in hovering flight at $\theta_0 = 14°$: Q–criterion contours on a radial plane for a phase of $\psi = 10°$*

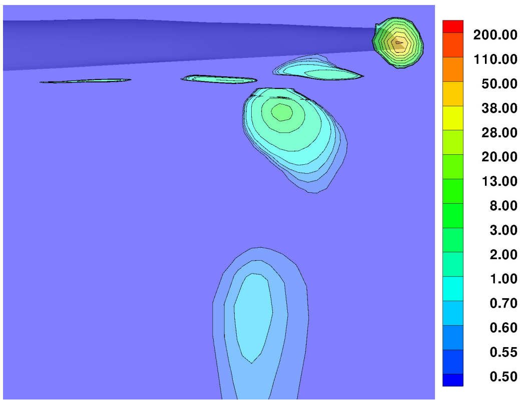

Figure 2.27: *Unswept blade in hovering flight at $\theta_0 = 14°$: Q–criterion contours on a radial plane for a phase of $\psi = 16°$*

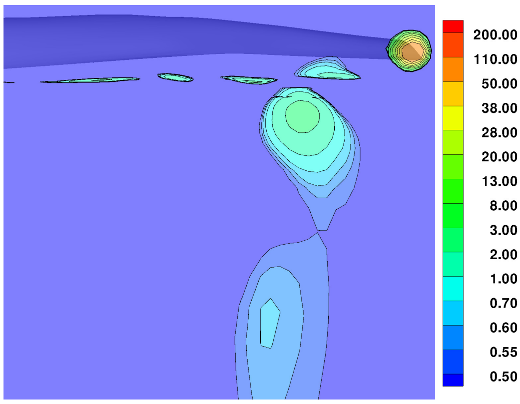

Figure 2.28: *Swept blade in hovering flight at $\theta_0 = 14°$: Q–criterion contours on a radial plane for a phase of $\psi = 16°$*

be observed by following the evolution of the tip vortex in both cases. It can be also observed that, even though the intensity of the tip vortex is slightly increase in the swept case, the interaction between the a given tip vortex and the following blade is reduced, as shown in Figure 2.23 and 2.24. In cruise flight condition, an increase of $1.46\ \%$ in the η_{cruise} has been achieved at the design point ($C_T = 0.0169$) where the η_{cruise} of the swept blade is 0.831. In Figure 2.21 and 2.22 also the results given by the BEMT solver for the unswept blade are reported. The results of CFD simulations for the unswept blade are quite closer to the results of BEMT calculations (except for the smallest C_T/σ values in hover and the highest ones in cruise flight). It can be also observed that the pitch trim angles θ_0 computed by the BEMT solver for the unswept blade in hovering and cruise flight conditions are almost equal to the ones predicted by the CFD analysis. However, the trim conditions predicted for the swept blade by the CFD solver are slightly different with respect to the unswept blade. In fact, the pitch trim angle for the swept blade is equal to $14.2°$ in hovering and to $58.0°$ in cruise flight.

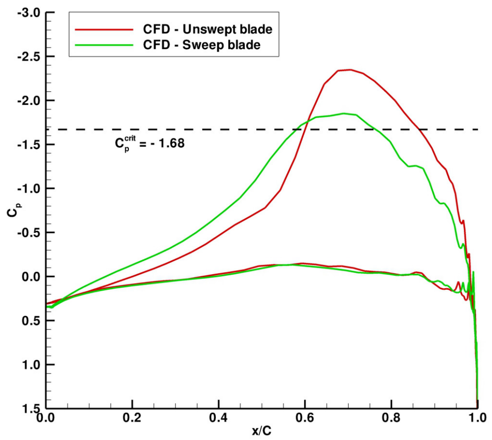

Figure 2.29: *Comparison between unswept and swept optimal blade: Sectional C_p distribution at $r/R = 0.81$ in cruise flight.*

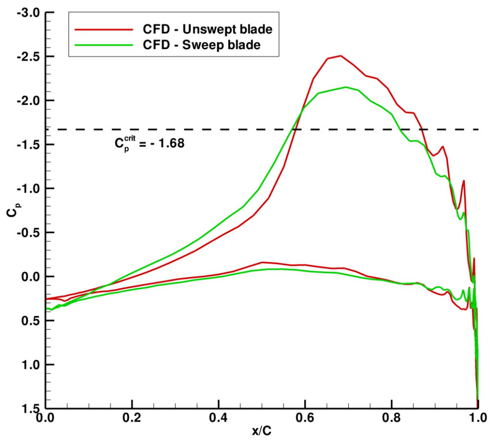

Figure 2.30: *Comparison between unswept and swept optimal blade: Sectional C_p distribution at $r/R = 0.86$ in cruise flight.*

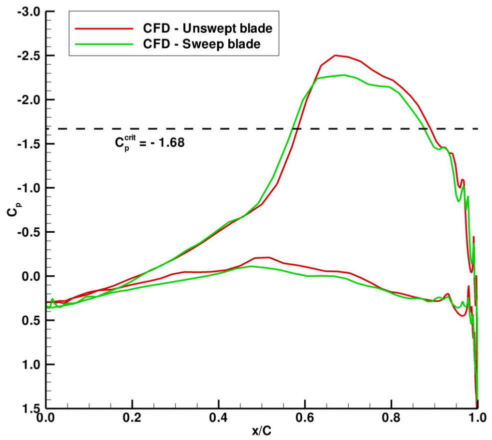

Figure 2.31: *Comparison between unswept and swept optimal blade: Sectional C_p distribution at $r/R = 0.90$ in cruise flight.*

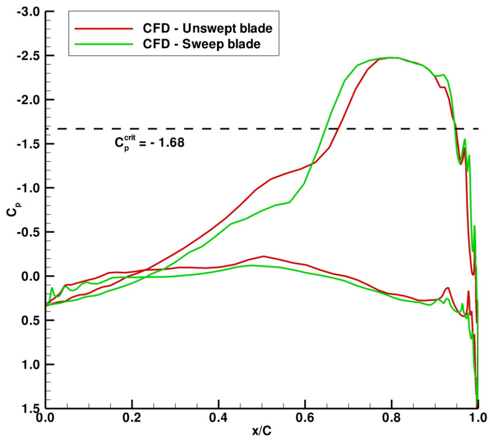

Figure 2.32: *Comparison between unswept and swept optimal blade: Sectional C_p distribution at $r/R = 0.95$ in cruise flight.*

Furthermore, from the comparison of the performance in aircraft mode, a substantial decay of the η_{cruise} can be noted after the design point for the unswept blade (see Figure 2.22). This behaviour can be mainly explained by the higher increase of the C_P after the design point for a given C_T with respect to the swept blade, as shown in Figure 2.33. The comparison between the pressure coefficient C_p distributions on several tip sections of both blades is shown in Figures from 2.29 to 2.32 confirming that the sweep angle distribution delays the onset of compressibility effects on the outer sections of the blade and limits the power losses in this region.

To evaluate the quality of the present results, the obtained rotor has to been compared with similar ones. Unfortunately public data about other proprotors of this kind are quite rare. The most obvious term of comparison is the rotor designed for the ERICA tiltrotor in the frame of TILTAERO [81] and ADYN [9] projects. Figure 2.34 shows

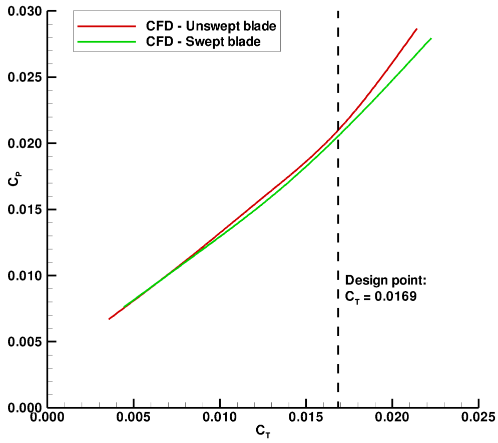

Figure 2.33: *Comparison between unswept and swept optimal blade: C_P as function of C_T in cruise.*

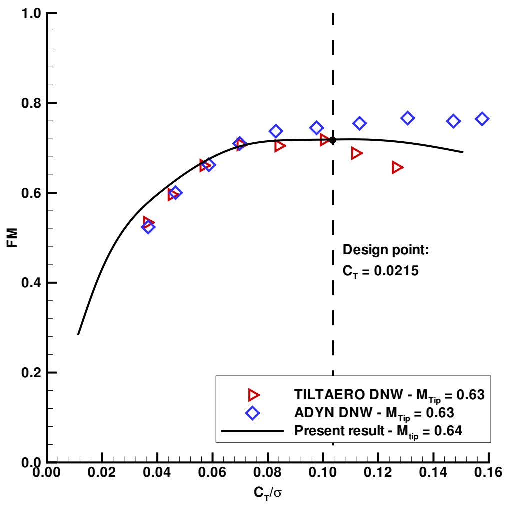

Figure 2.34: *Rotor FM as function of C_T/σ: comparison between predicted FM of selected optimal individual I_o with optimised sweep angle distribution and hover tests data of ERICA blades.*

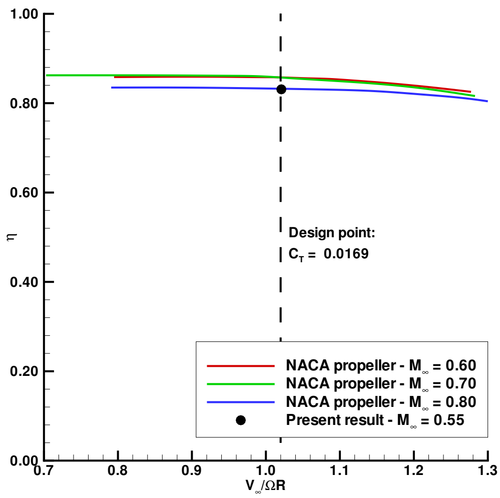

Figure 2.35: *Rotor η as function of $V_\infty/(\Omega R)$: comparison between predicted η of selected optimal individual I_o with optimised sweep angle distribution and wind–tunnel tests data of an high–speed propeller.*

that the present rotor generally has a higher hover efficiency with respect to the first version of the ERICA rotor (TILTAERO blades, [6]), while it presents a lower FM with respect to the final version of the ERICA rotor (ADYN blades, [6]). The same comparison for the aeroplane mode flight is not possible because public data on this condition are not available for the ERICA proprotor. Thus the optimised rotor has been compared with a reference NACA high–speed propeller [22]. Figure 2.35 shows that the optimised rotor has an η_{cruise} that is found to be similar to the corresponding value of a real high–speed propeller.

2.3 Aerodynamic wing design

The hovering performance and the lifting capability of a conventional tiltrotor aircraft operating in helicopter mode are strongly affected by the aerodynamic interaction between wing and rotors. In fact, in helicopter flight mode the presence of the wing under the rotor significantly modifies the rotor wake and thus it is responsible for loss of rotor performance [16]. Moreover, when the rotor wake impinges on the wing surface a vertical force in the opposite direction of the rotor thrust is generated on the airframe. It follows that to have acceptable hover performance, in existing tiltrotor models (XV–15, V–22 Ospray and BA609) large rotors have been adopted however increasing the aerodynamic interference due to wing–rotor [59] and rotor–rotor [69] interaction. For the V–22 Osprey in hovering, it has been demonstrated by Felker [24], McVeigh [57] and Young at all. [85] that the vertical force (download) acting on the airframe is approximately $10\ \%$–$15\ \%$ of the rotor thrust.

To overpass these limitations and then to reduce the negative effects due to the wing–rotor interaction in helicopter mode, a possible approach could be represented by the reduction of the wing surface on which the rotor wake strikes. An efficient way to achieve this objective is represented by the possibility to tilt the external part of the wing (i.e. the part of the wing that is inside the rotor slipstream) as in the tiltwing configuration. The idea to split each half–wing in two portions, the outer part that can be rotated and the inner part that is fixed, and to use a tube to connect the nacelles and to drive the rotors gives the possibility to use the fixed wing to hold only the bending loads, as described by Alli et all. [4]. Actually, conventional tiltrotor already employed the solution of the tube to connect together the nacelles and the rotors. However, in the tiltwing solution the tube play also a structural role because it has to carry the torsion moments given by the rotors. It follows that the higher is the span of the fixed wing, the higher is the bending stiffness given by its conventional box structure. On the other hand, to minimise the aerodynamic force acting in the opposite direction of the rotor thrust in all the flight conditions in which the aircraft operates in helicopter mode, it is necessary to increase the span of the tilting portion of the wing.

The design of a wing that represents a good compromise in terms of aerodynamic efficiency in very different flight conditions and also in terms of structural requirements is a very challenging task. In the present work, in order to define the wing layout, the effects of the span position of the tilt wing section on the tiltrotor performance have been studied and wing download caused by the interaction with the rotor wake both in hover and in climb flight conditions have been estimated. In particular, the span of the tilting portion of each half–wing has been defined trying to minimise the drag force that raises on the wing in helicopter mode when the rotor wake impinges on it. The two flight conditions (helicopter mode) analysed in the following are the same that have been considered for the design of the rotor blade (see Table 2.3).

Before starting with the analysis of the tilt wing location, and once the overall wing dimensions have been defined (the wing span and the chord distribution, see Section 2.1), the wing sectional airfoil shape and the distance between the wing and the rotor have been chosen. An important constraint that limits the choice of the airfoil is represented by the thickness of local sections that have to be large enough because the nacelles and the rotors are connected together with the torque tube that goes within the wing. For this reason we decided to use an airfoil with a thickness of $21\ \%$ of the local wing chord. This choice is consistent with the thickness of the other tiltrotor models that employ airfoils with a thickness that varies between $21\ \%$ (BA–609 and ERICA) and $23\ \%$ (XV–15 and V–22 Osprey) of the local chord. Since the cruise Mach number M_∞ in aircraft mode flight at high speed has been fixed to 0.55 (see Table 2.3), the airfoil shape has been chosen to have good performance in this flight condition. With the aim to reduce the negative effects due to onset of compressibility losses on the wing, we decided to employ an airfoil designed for this purpose. In particular, we selected an airfoil that belongs to the well known NACA 6A–series that is the NACA 64A221 [1], [52] and [66]. As far as the distance between the rotor and the wing is concerned, we fixed the value by comparison with the existing tiltrotor models. Therefore, the nominal value used in the aircraft design phase was $h^w = 0.324\ R$, where h^w was the distance between the leading edge of the wing section at the wing–nacelle junction and the plane normal to the rotor axis and passing through the rotor centre. The influence of this parameter on the wing–rotor aerodynamic interaction will be evaluated with the experimental model (as described in Section 4.2.2 and 4.3.2).

To define a wing that gives the maximum aerodynamic performance in terms of download in hover, we used CFD calculations to test different wing configurations in terms of span–wise locations of the tilt section. As just mentioned in Section 2.1, a half–model configuration (Figure 2.1) reproducing one half–wing and one rotor with the nacelle have been taken into account. We decided to test 5 different wing configurations characterised by the different location of the span–wise location of the tilt section plus one non–realistic configuration that represents the case in which all the wing is tilted. In Figure 2.36, a view of the wing and its nacelle is reported with the location of the tilt wing sections tested. Apart from the wing configuration, the rotation point of the tilt wing has been fixed on the $25\ \%$ of the local chord. Moreover, with reference to the airfoil chord, the angle of attack between the fixed wing chord and the horizon of the reference system has been established equal to $0°$. As a consequence, when the rotating portion of the wing is tilted, its chord forms an angle θ^{Tilt} of $90°$ with the chord of the fixed wing, as shown in Figure 2.37. Different structured multi–block grids have been achieved for the 2 wings for each of the 5 configurations but the total number of cells was kept constant. In general, the computational mesh is composed by 6 structured multi–block grids, for a total of 48 blocks and about 13.3×10^6 cells. The computational grid details are reported in Table 2.7 for each configuration tested. The non–realistic wing configuration has been tested by using the grids TS 2. With the aim to limit the total number of cells, the background grid is composed by 2 different grids, one fine (the inner grid, farfield 1) and one coarse (the outer grid, farfield 2). All

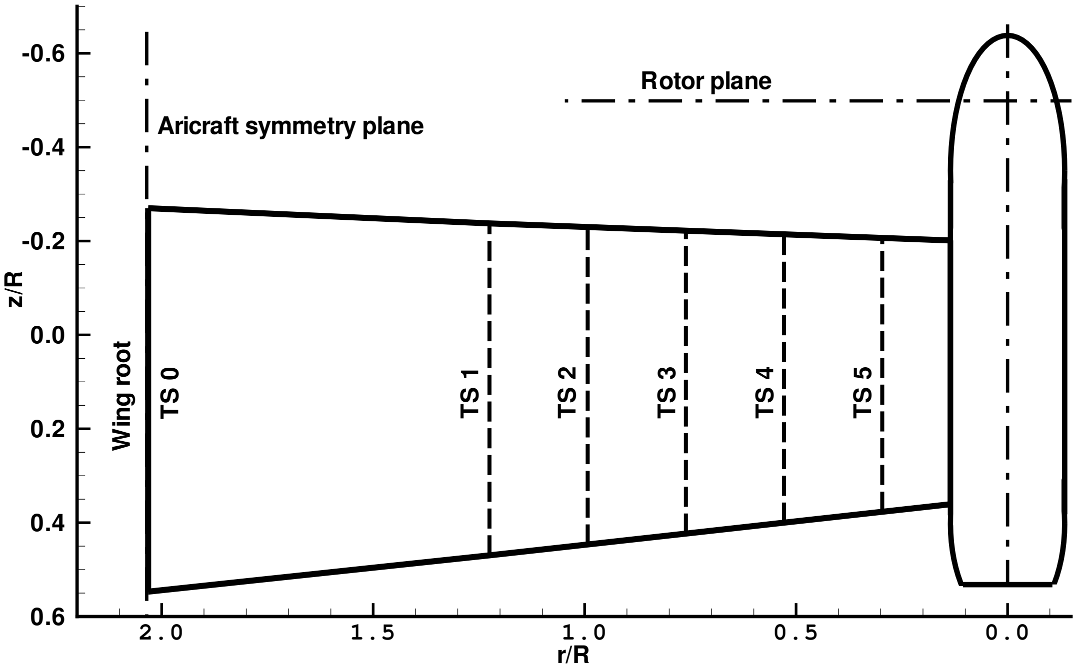

Figure 2.36: *Schematic view of different tilt wing configurations.*

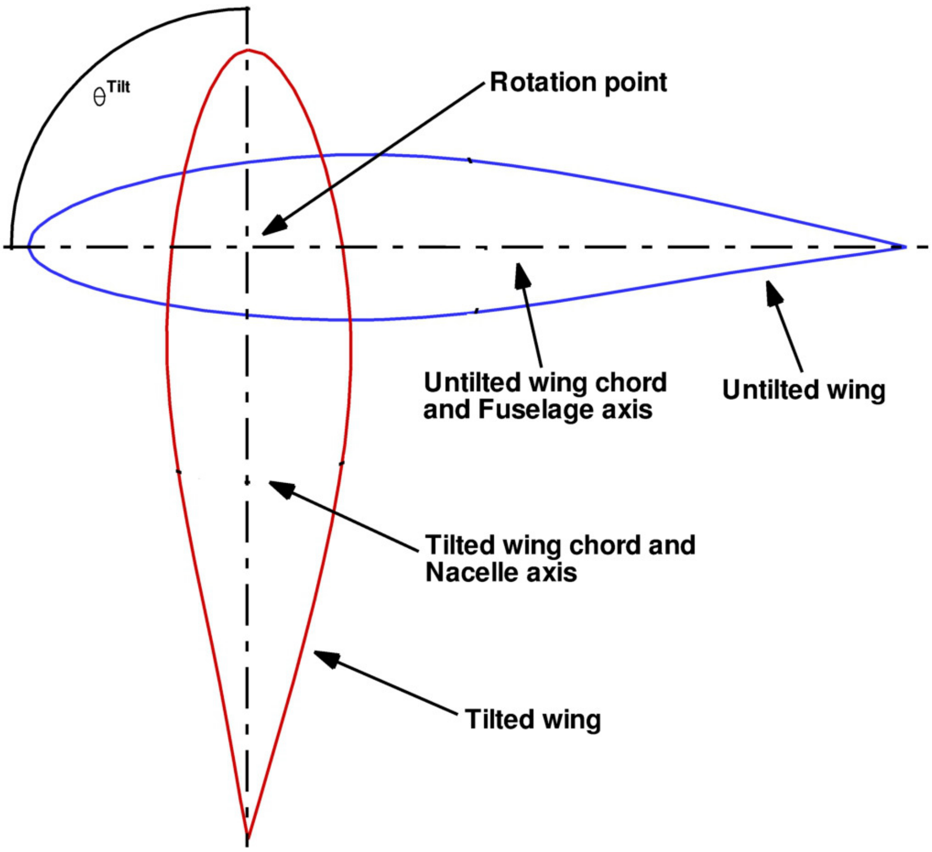

Figure 2.37: *Wing section in tilted configuration ($\theta^{Tilt} = 90°$).*

Grid	No. Blocks	No. Cells ($\times 10^6$)				
		TS 1	TS 2	TS 3	TS 4	TS 5
Wing 1	7	1.76	2.13	2.28	2.54	2.68
Wing 2	9	3.06	2.93	2.66	2.42	2.25
Nacelle	25	5.21	5.21	5.21	5.21	5.21
Actuator Disk	1	0.29	0.29	0.29	0.29	0.29
Farfield 1	1	1.95	1.95	1.95	1.95	1.95
Farfield 2	5	0.84	0.84	0.84	0.84	0.84
Total	48	13.11	13.35	13.23	13.25	13.22

Table 2.7: *Computational mesh details for half–aircraft calculations.*

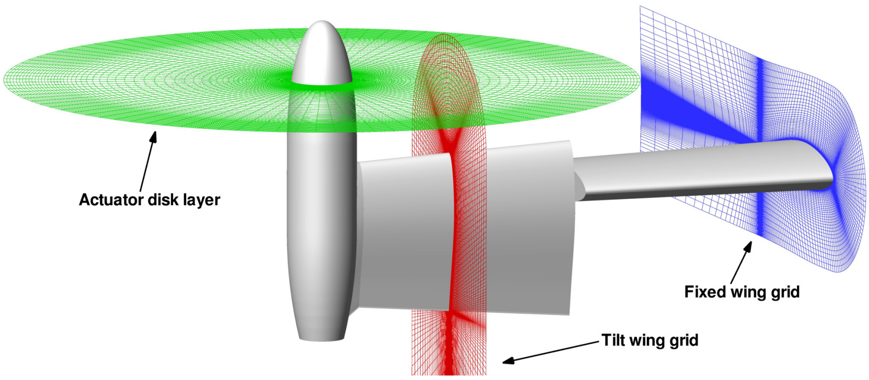

Figure 2.38: *Example of grids system for hovering and climbing flight for steady CFD calculations (configuration TS 2).*

the other grids are contained inside the finest background grid, having similar spatial resolution. The grids of wings and nacelle are C grid, with the outer boundaries located $0.4\ R$ away from the bodies except in the wake direction where the boundaries are located $1.6\ R$ from the trailing edge. Since the root of the fixed wing (wing 1) lies on the aircraft symmetry plane, a symmetry condition has been applied to that plane, whereas both wings and the nacelle have been modelled through no–slip boundary conditions. Because of need of many different simulations, in this phase of the activity it has been decided to save computational time performing steady simulations and reproducing the effects of the rotor with an actuator disk. An example of the grid system is shown in Figure 2.38. The actuator disk model embedded in ROSITA approximates the forces applied by the rotor blades to the air flow over a disk having the same diameter of the rotor. The actuator disk grid models a disk without thickness in a single layer of cells of a cylindrical O–H grid in which a non uniform source distribution is given to reproduce the desired force (per unit area) distribution [12]. Another simplification has been introduced by considering only the axial load distribution acting on the disk without simulating the swirl effect due to the blade rotation. This kind of approximation can be accepted at this stage since in the rotor slipstream the axial velocity component is considerably higher than the azimuthal and radial components. The force distribution on the disk has been computed starting from the load distributions on the blade that are known from previous CFD calculations performed on the single blade (see Section 2.2.4).

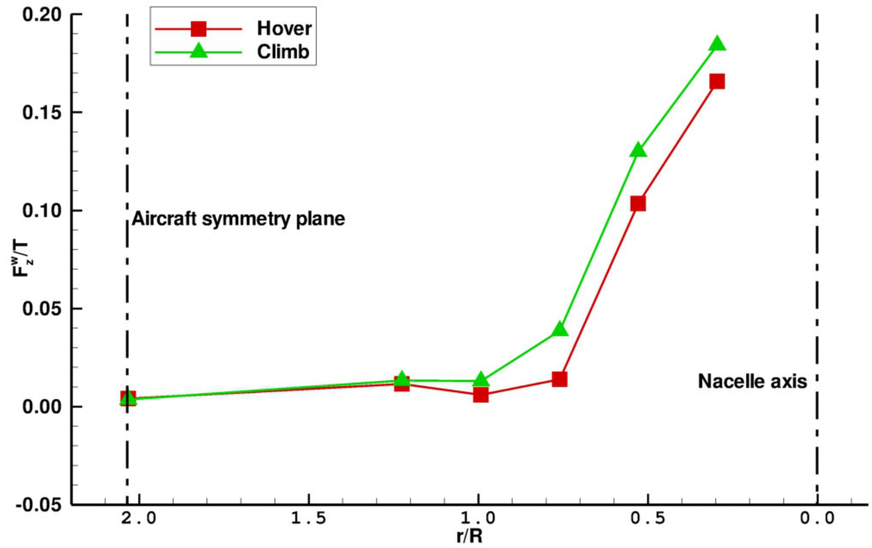

Figure 2.39: *Wing vertical force F_z^w/T distribution as function of tilt wing span for the hovering and climbing flight.*

Results for the 5 different wing configurations and the non–realistic configuration with both wings tilted, for hovering and climbing flight conditions are shown in Figure 2.39 where the download estimations for every tested configuration are displayed. From Figure 2.39 it is quite clear that configurations TS 1 and TS 2 give better results than other configurations in both flight modes. In these 2 configurations, the rotor wake strikes only on tilted wing surface without any significant interaction with the fixed wing. In particular, the lowest value of the vertical force acting on the wing and expressed in terms of the rotor thrust F_z^w/T is achieved in configuration TS 2 for the hovering flight, that is 0.0059, and in configuration TS 1 for the climb condition, that is 0.012. Also configuration TS 3 gives good results in terms of F_z^w/T in hover, but some interactions between the rotor wake and both wings arise near the tilt section. In configurations TS 4 and TS 5, in which the tilt wing span is significant smaller than the rotor radius, the interaction between wing and rotor becomes more relevant giving higher F_z^w/T values for both hovering and climbing flight conditions. Moreover, the latter configuration is similar to the conventional tiltrotor configuration and the value of F_z^w/T estimated in hover for the configuration TS 5 is quite similar to the results obtained for the XV–15 and V–22 Osprey [57], [24]. Examples of the flow field in terms of the velocity magnitude distribution in a plane parallel to the thrust direction in each configuration are given in Figure from 2.40 to 2.45 for the hovering flight. From these figures it is apparent that the higher is the span of the fixed wing portion the higher is the interaction of the rotor wake with the fixed wing surface. In particular, when the tilt section is located inside the rotor wake boundary the aerodynamic advantages of the tiltwing solution decrease until they disappear, as shown in Figure 2.39. The strong interaction between the rotor wake and the wing is evident in configurations TS 4 and TS 5, respectively Figure 2.43 and 2.45. In both cases, the presence of the untilted wing inside the rotor slipstream limits the contraction of the rotor wake in the region above the upper surface of the wing. A comparison between the configurations analysed reveals that in this flow region the rotor wake contraction approaches a minimum value

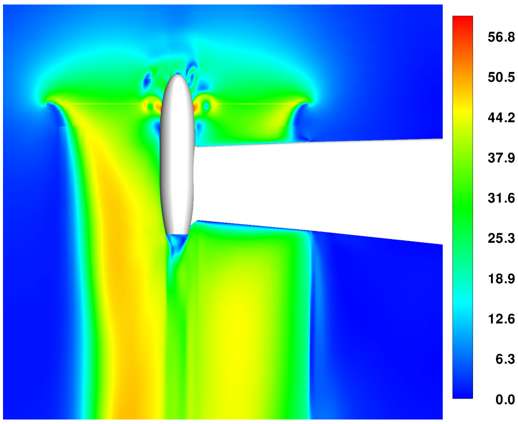

Figure 2.40: *Velocity magnitude distribution, configuration TS0, hover condition.*

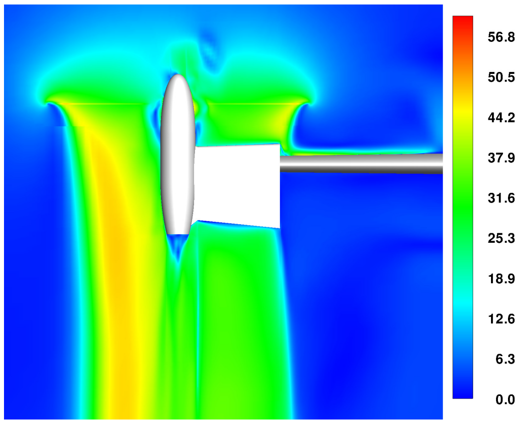

Figure 2.41: *Velocity magnitude distribution, configuration TS3, hover condition.*

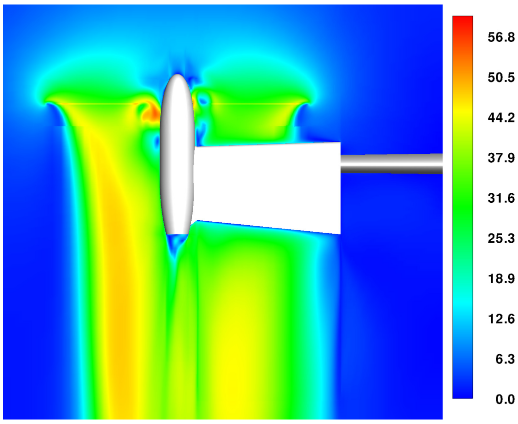

Figure 2.42: *Velocity magnitude distribution, configuration TS1, hover condition.*

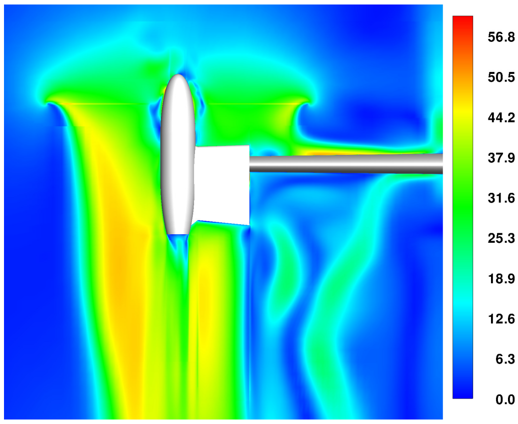

Figure 2.43: *Velocity magnitude distribution, configuration TS4, hover condition.*

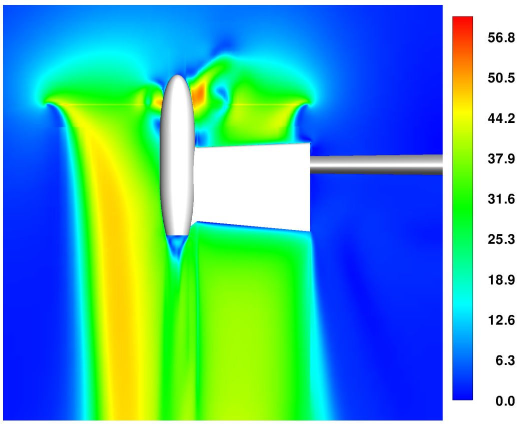

Figure 2.44: *Velocity magnitude distribution, configuration TS2, hover condition.*

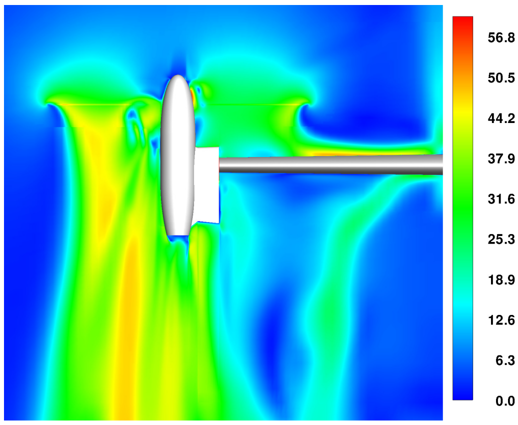

Figure 2.45: *Velocity magnitude distribution, configuration TS5, hover condition.*

of about $0.83\ R$ when the tilt wing section is outside the rotor slipstream (configuration TS 0 and TS 1 and TS 2) while it reaches the value of about $0.94\ R$ when the tilt wing

Wing airfoil section	NACA 64A221
Wing root chord	3.00 m
Wing tilt chord	2.51 m
Wing tip chord	2.08 m
Fixed–wing span	3.74 m
Rotating–wing span	3.17 m
Wing twist	0.0°
Wing dihedral	0.0°
Wing sweep	0.0°

Table 2.8: *Geometric characteristics of the wing in the final configuration (TS 2).*

section is located inside (configuration TS 4 and TS 5). Although configuration TS 3 has the tilt wing section located inside the rotor slipstream, the surface of the untilted wing in which the rotor wake impinges is very low, as shown in Figure 2.41. In this case the rotor wake contraction approaches a minimum value of about $0.88\ R$.

In conclusion, CFD analyses on the whole aircraft reveal that to minimise the drag force that raises on the airframe in helicopter mode it is convenient to locate the tilt wing section in the proximity of the rotor wake boundary, just outside it. Configuration TS 2 seems to be the solution which gives the best aerodynamic performance by minimising the effects of the rotor wake on the wing and the influence that the wing has on the rotor slipstream. For these reasons configuration TS 2 has been finally selected for the test rig design. In Table 2.8 are reported the wing data at full–scale.

CHAPTER 3

Test rig description

Once the main characteristics and the geometrical dimensions of the tiltwing aircraft have been defined at full–scale, an experimental test rig representing one half–wing together with the corresponding rotor and nacelle has been designed for hovering tests. In the present chapter, the 0.25 scaled tiltwing half–model for hover tests is presented and a detailed description of test rig is given.

3.1 Experimental setup

The goal of this work is the study of the aerodynamic interaction between wing and rotor in a non conventional tiltrotor aircraft which belongs to the innovative typology of high–performance tiltwing aircraft. Since the flight conditions in which an aircraft of this kind can operate are very different if compared one to each other, the design and the manufacture of an experimental model that allows to tests every flight condition is a very demanding task. For this reason, we decided to concentrate our attention only on the hover flight condition in helicopter mode because this operative condition is very important inside the flight envelope of a tiltrotor aircraft and only few data are available in literature on this kind of aircraft configuration in hover. Therefore, the experimental test rig described and analysed in the present chapter has been designed by following this idea. In particular, we designed a new test rig which allows to study a tiltwing aircraft in the hover flight condition giving also the possibility to investigate the sensibility of the aircraft to some parameter, as the wing configuration and the relative distance between the wing and the rotor disk.

With the aim to reduce the rotational speed of the blades and to limit the required power of the rotor model, we selected a scale of $1/4$ with respect to the full–scale aircraft. In particular, the 0.25 scaled tiltwing half–model represented the aircraft that

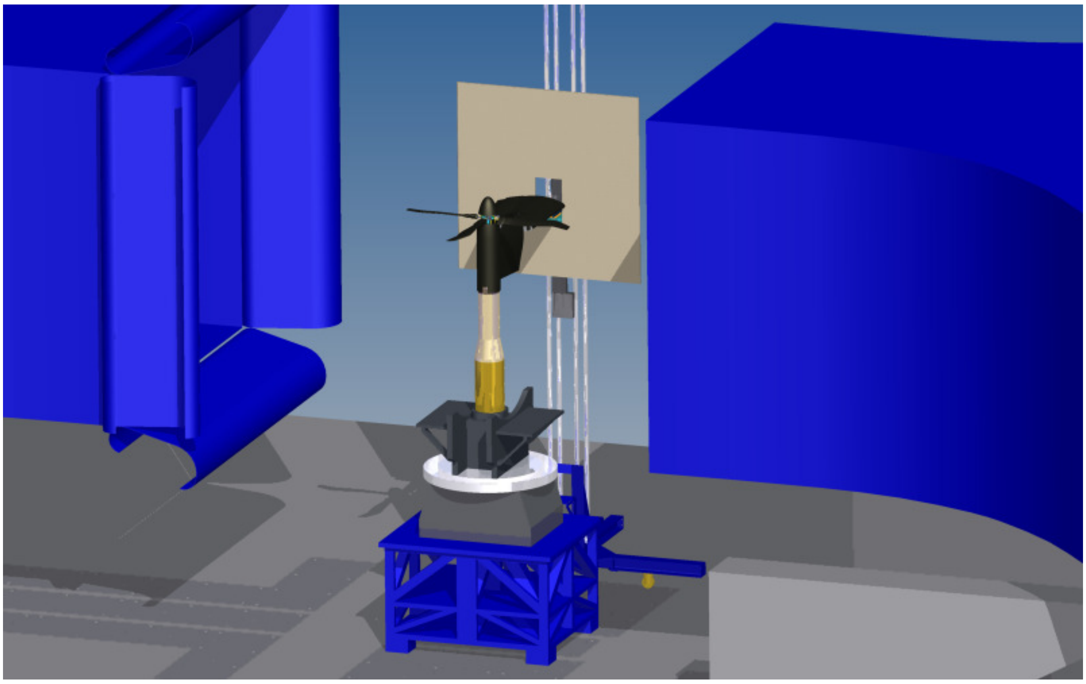

Figure 3.1: *A schematic 3D view of the tiltwing half–model test rig.*

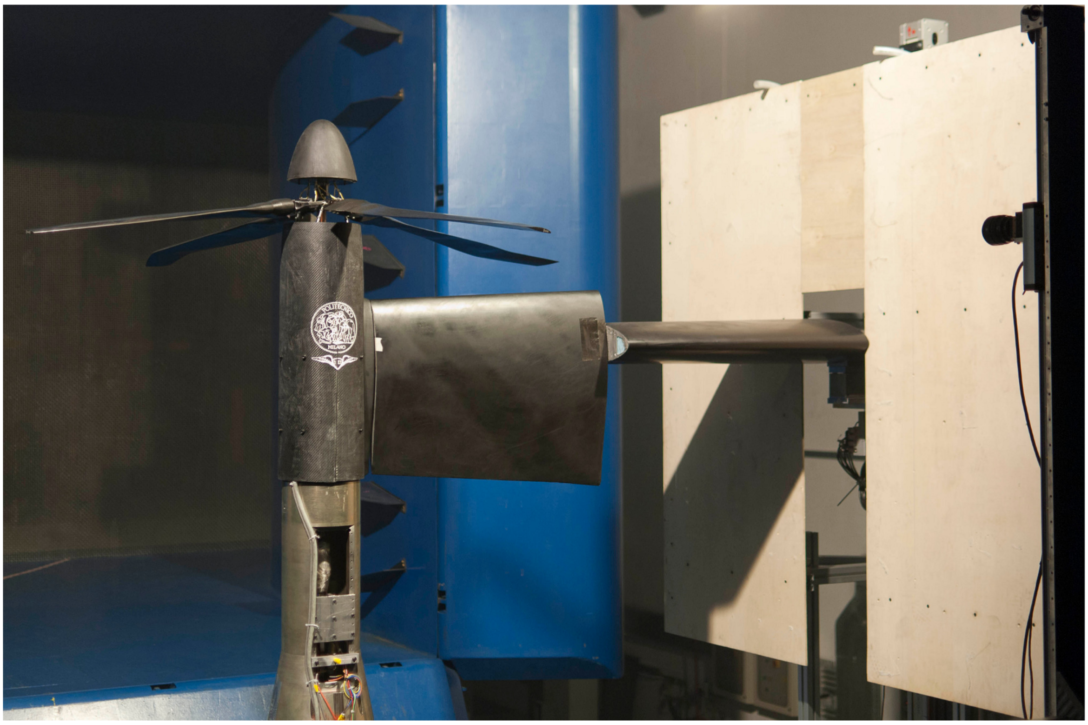

Figure 3.2: *Experimental test rig for hovering tests in the open test section of the Politecnico di Milano Large Wind Tunnel.*

has been described in the previous chapter and consisted of two main components that were the rotor system and the half–wing with an image plane. The experimental model has been realised in the DSTA (Dipartimento di Scienze e Tecnologie Aerospaziali)

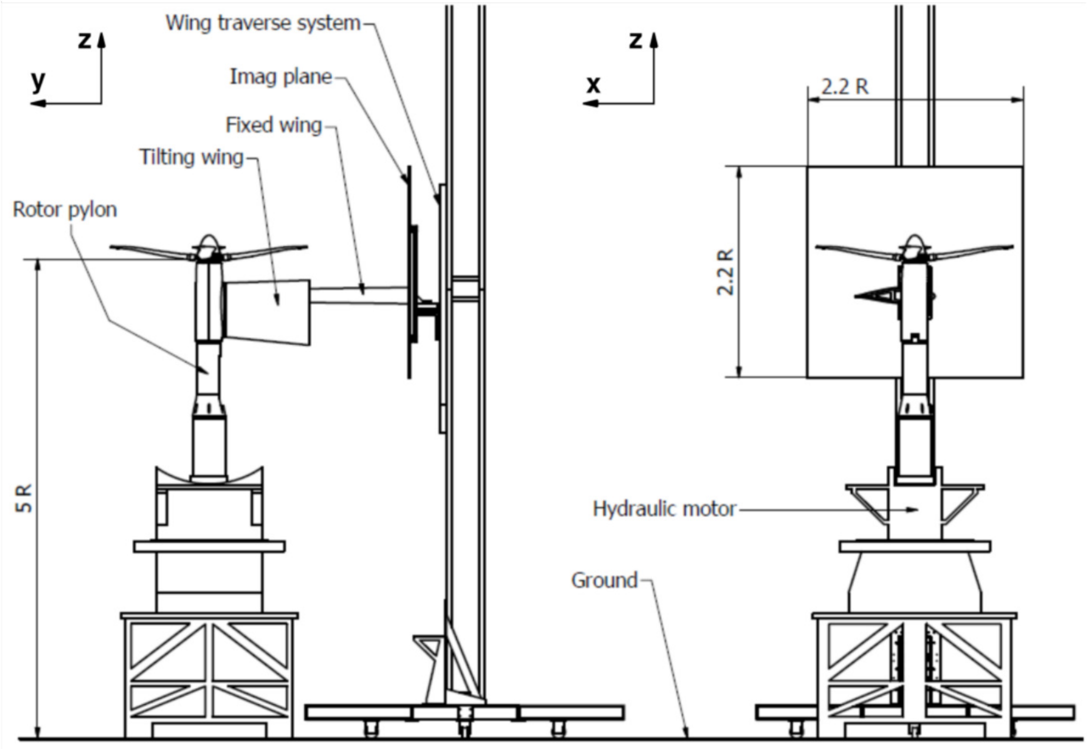

Figure 3.3: *Schematic view of the experimental test rig and model reference system.*

Aerodynamics Laboratory. In Figure 3.1 and 3.2 a schematic view and a photo of the system inside the Large Wind Tunnel of the Politecnico di Milano are shown. Frontal and lateral views of the whole test rig is shown in Figure 3.3, where also the model reference system is reported. With the aim to measure the rotor and the wing loads separately, the two main systems were not linked in any parts. Moreover, the systems have been designed to test both the isolated rotor and the aircraft half–model.

The rotor was powered by an hydraulic motor (maximum power $16\ kW$ at $3000\ rpm$) located inside a swiveling basement with two degrees of freedom which is placed on an aluminium basement. This structure is $2.27\ R$ height. The rotor hub was mounted on a rigid pylon that is composed by three main parts and is located over the hydraulic motor. The first part of the rotor pylon is directly fixed on the motor and a transmission shaft with a diameter of $40\ mm$ pass through it. In the second portion of the pylon, over a second transmission shaft with a diameter of $35\ mm$, is located a 24–channel slip ring (SHR–series by Servotecnica) for the transmission of electrical power and signals form and to the rotating part of the rotor hub, as shown in Figure 3.4 and 3.5. On the shaft has been placed also a magnet and an Hall Effect Sensor has been employed to measure the rotational speed of the rotor. Finally, the third part of the rotor pylon was represented by the rotor hub and the instrumentation to read the loads acting on the system. During the experimental tests, the nominal rotational speed of the rotor, which rotates in anti–clockwise direction, was $n = 1120\ rpm$. The tip Mach number was 0.32 which correspond to $1/2$ the tip Mach number of full–scale aircraft at design point in hover. The rotor had four blades designed in–house, as described in Section 2.2. Since the scale of the model was $1/4$, the rotor radius was $0.925\ m$ and it was placed at an height

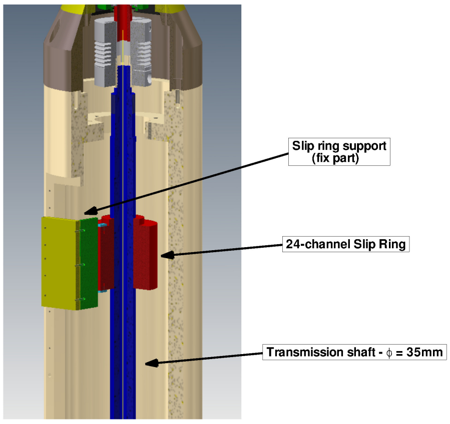

Figure 3.4: *Detail of the Slip Ring on the rotor pylon.*

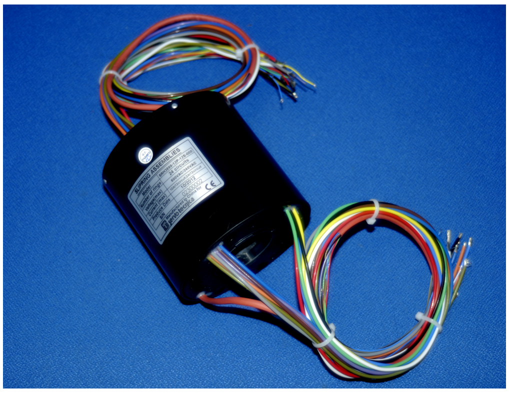

Figure 3.5: *Slip Ring, SRH–series.*

of 5 R from the ground. The thrust given by the rotor has been measured by an holed six–component strain gauge balance (JR3 E Series Force Torque Sensors) located under the rotor hub. The torque has been measured by an in–house instrumented holed shaft which passed through the balance and it was directly linked to the rotor hub shaft by a motoring coupling. The instrumented holed shaft for torque measure and its calibration curve have been reported in Figure 3.6 and 3.7. Under the instrumented shaft, a flexible joint (KTR RADEX–N Joint, model NANA–2, Figure 3.8) has been used to avoid the transfer of axial force F_z^r to the lower part of the transmission shaft providing also compensation for axial, angular and radial misalignments. Before starting with the tests, to verify the joint effects on rotor balance, a static calibration of the system has been carried out on the rotor model (a description of the calibration system can be found in [67]). The estimated load transfer through the rotor shaft due to the flexible joint was in the order of $0.5\ N$ that is less than the balance accuracy ($2.5\ N$). In Figure 3.9 the calibration curve for the axial force F_z^r has been reported.

The carbon fibre nacelle, that has been manufactured in–house, had an external maximum diameter of $0.27\ R$ and it was not weighed because was mounted on the lower part of the rotor pylon. The nacelle air intake has not been taken into account in this study hence it was not present on the nacelle. Also the half–wing model has been manufactured in–house and it was $1.90\ R$ long, where the span of the wing had to be intended from the aircraft symmetry plane (wing root) to the nacelle junction (wing tip). The internal structure of both wing portions were composed by Styrofoam (extruded polystyrene foam) while aluminium formers were placed at the extremities of each part. The external skin of the wing was made by a 2–layers carbon fibre skin. The tilt section was located $1.01\ R$ from the symmetry plane and the external part of the wing could rotate from $0°$ (untilted configuration) to $90°$ (tilted configuration). The system has been realised to allow the possibility to test some intermediate angle configurations (every $15°$). The wing was linearly tapered, untwisted and all sections were aligned with respect to the $25\ \%$ of the local chord, as described in Section 2.3. In Table 3.1 the half–wing model characteristics are listed. The wing was mounted on an independent traversing system and it was not connected to the nacelle and rotor in order to have a more accurate evaluation of the effects due to the impingement of the

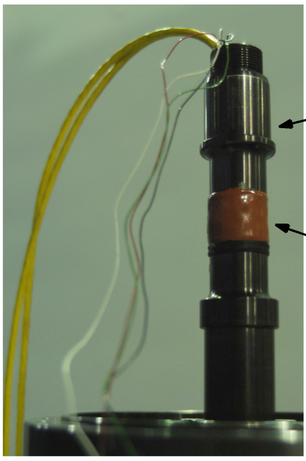

Figure 3.6: *Detail of the instrumented holed shaft for torque measure.*

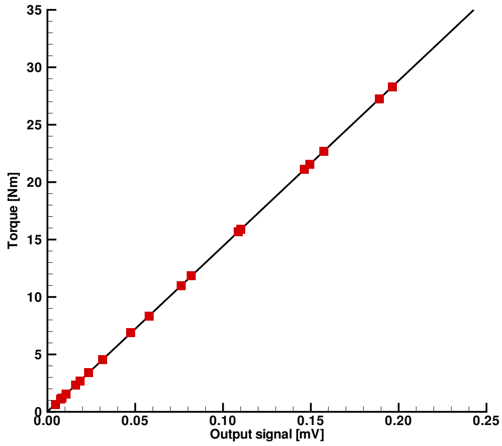

Figure 3.7: *Calibration curve of the instrumented holed shaft for torque measure.*

Figure 3.8: *Detail of the flexible joint which avoids the transfer of axial force F_z^r.*

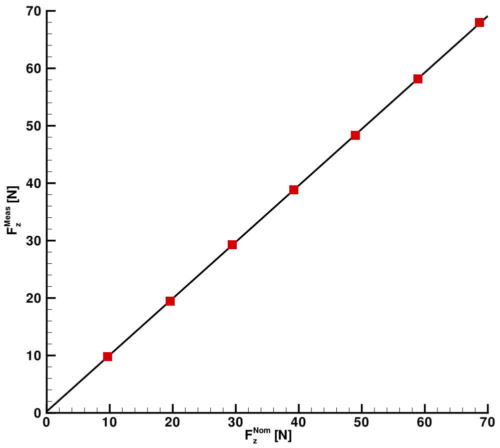

Figure 3.9: *Test curve of the flexible joint for the axial loads (F_z^r).*

rotor wake on the airframe model. Forces and moments on the wing have been mea-

Wing airfoil section	NACA 64A221
Wing root chord	0.750 m
Wing tilt chord	0.625 m
Wing tip chord	0.520 m
Fixed–wing span	0.933 m
Rotating–wing span	0.792 m
Fixed–rotating configuration	0°, 15°, 30°, 45°, 60°, 75°, 90°
Wing twist	0.0°
Wing dihedral	0.0°
Wing sweep	0.0°

Table 3.1: *Geometric characteristics of the half–wing model.*

sured by a seven–component strain gauge balance located at the wing root, as shown in Figure 3.10 and 3.11. In order to restore the symmetry condition on the symmetry

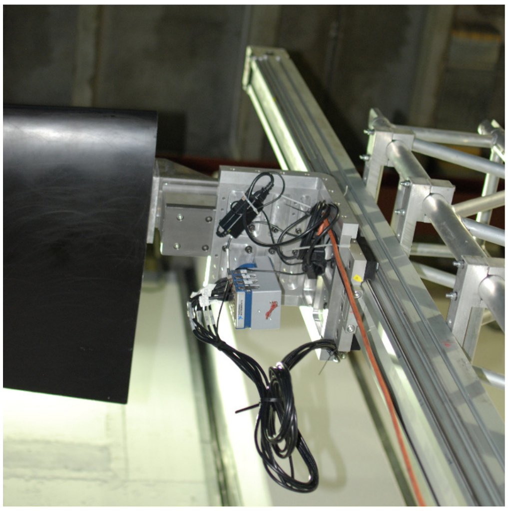

Figure 3.10: *Wing support and balance over the traversing system.*

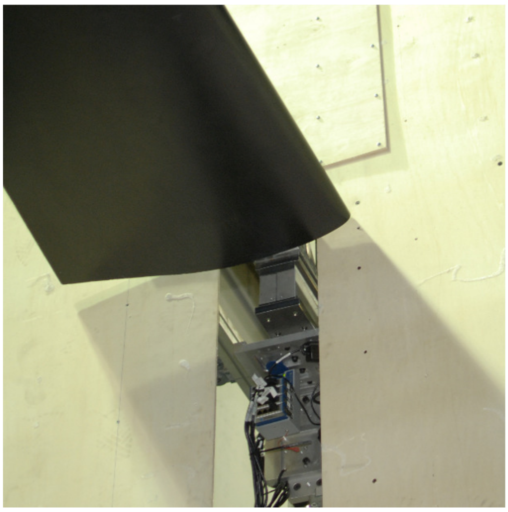

Figure 3.11: *Detail of the wing support over the traversing system with the image plane on.*

plane of the model, an image plane was placed at the fixed wing root and it was $2.2\ R$ high and $2.2\ R$ wide [24], [69]. The image plane was fixed on the support of the wing traversing system and the distance between the image plane upper side and the rotor plane was $0.9\ R$. However, to investigate the influence of the relative distance (h^w) between the rotor and the wing on the aircraft performance, the wing location has been changed along the z–axis by moving the wing support on its traversing system.

3.2 Rotor hub

It is well known [54], [4] that tiltrotor aircraft are subject to the so called rotor/pylon/wing instability in high–speed aircraft mode flight. To prevent this dangerous dynamic phenomenon, a gimballed (stiff in plane) rotor hub design is currently employed in this kind of aircraft. In general a gimballed system is much more sophisticated with respect to common helicopter rotor hub both from a mechanical and dynamic point of view. Fou our purpose however, there is no need to choose a gimballed rotor hub in the experimental model since we are interested only on the hovering flight (and in the next future on the first part of the conversion maneuver at low advance ratio $V_\infty/\Omega R$). In this regard, we decided to mount on the upper part of the pylon a four bladed fully articulated rotor hub which represented a typical helicopter hub.

The collective, longitudinal and lateral pitch controls were provided to the blades by means of three independent electric actuators acting on the swashplate. On each electric actuator, a linear potentiometer has been installed to have a feedback signal on the actual position of each command. Each blade was attached to the rotor hub through the flap, led–lag and pitch hinges located in different positions. A schematic view of the rotor hub is shown in Figure 3.12 while a photo of the rotor hub with the four blades and the ogive is reported in Figure 3.13. The led–lag hinge was located beyond the flap hinge while the feathering bearing was placed further outboard. Even though a large number of helicopters, which use a fully articulated rotor hub, employ mechanical dampers on the lag hinge to increase the damping in the led–lag plane, in

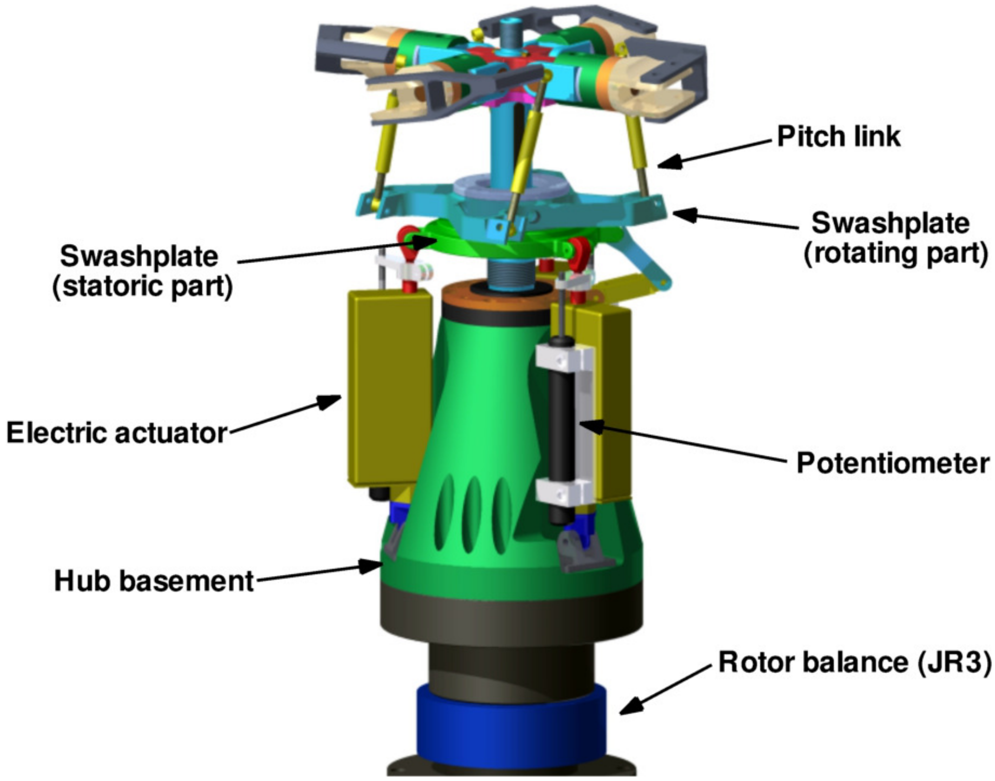

Figure 3.12: *Detailed Schematic of the four bladed rotor hub.*

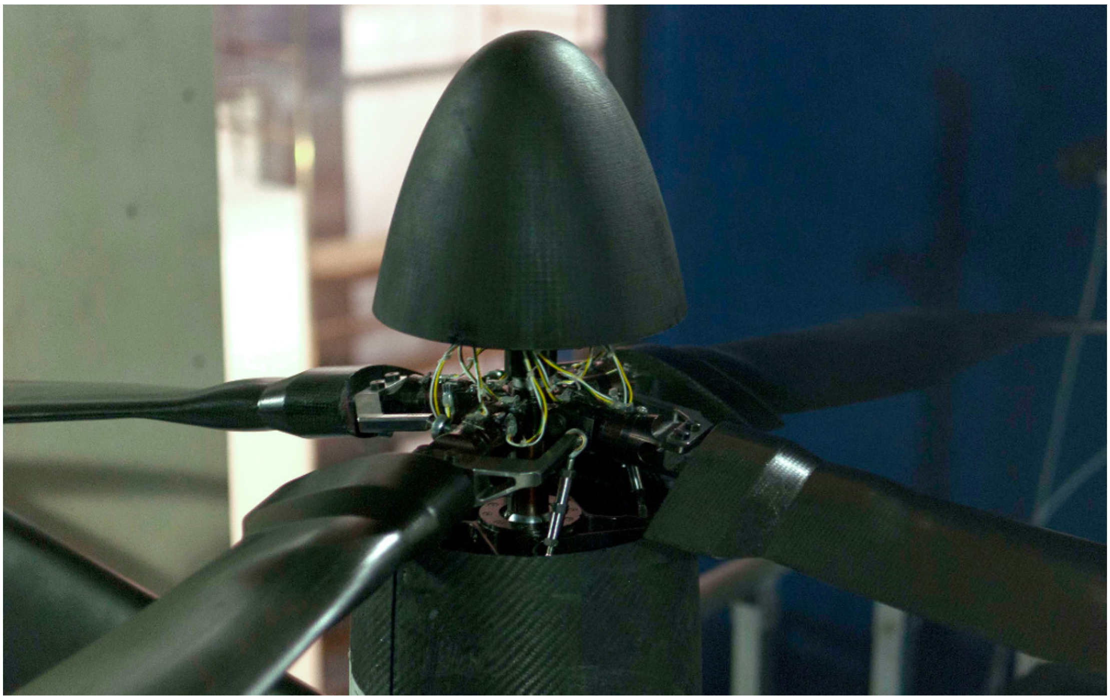

Figure 3.13: *View of the rotor hub with the four blades and the ogive.*

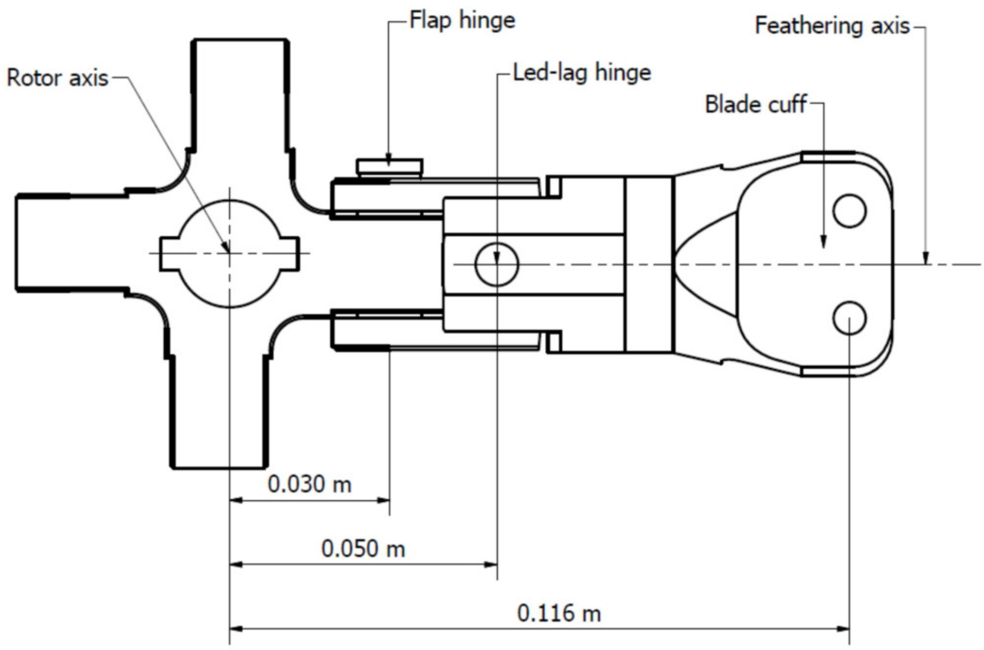

Figure 3.14: *Schematic of the rotor hub hinges (top view).*

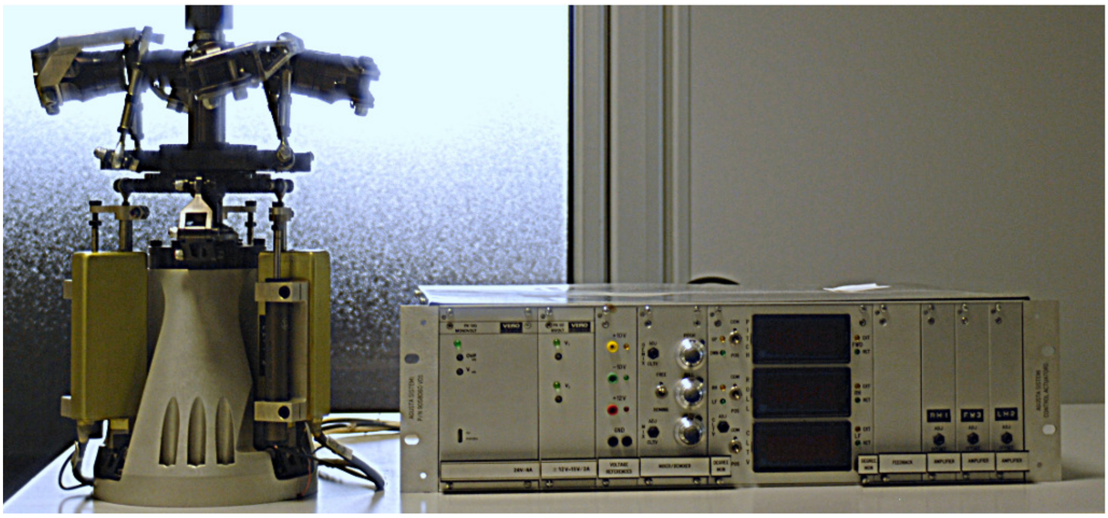

Figure 3.15: *Rotor command console to manage the collective, longitudinal and lateral pitch controls.*

the present case no dampers have been fitted on the led–lag hing of the rotor model. More in detail, the flap hinge had an offset of $e_f = 3.2$ % of the rotor radius while the lag hinge had an offset of $e_{ll} = 5.4$ %, as shown in Figure 3.14. To change the position of the blade, the blade cuff could be rotated around the feathering axis by means of the pitch horn that was attached to the blade cuff outboard of the pitch bearing. The connection between the pitch horn and the pitch link lied on the flap hinge axis assuring no pitch–flap coupling. The electric actuators were controlled by means of a dedicated console that is shown in Figure 3.15.

In order to measure directly the pitch, led–lag and flap angles on the rotor hinges and since the dimensions of the moving parts of the hub were small, Hall effect sensors and

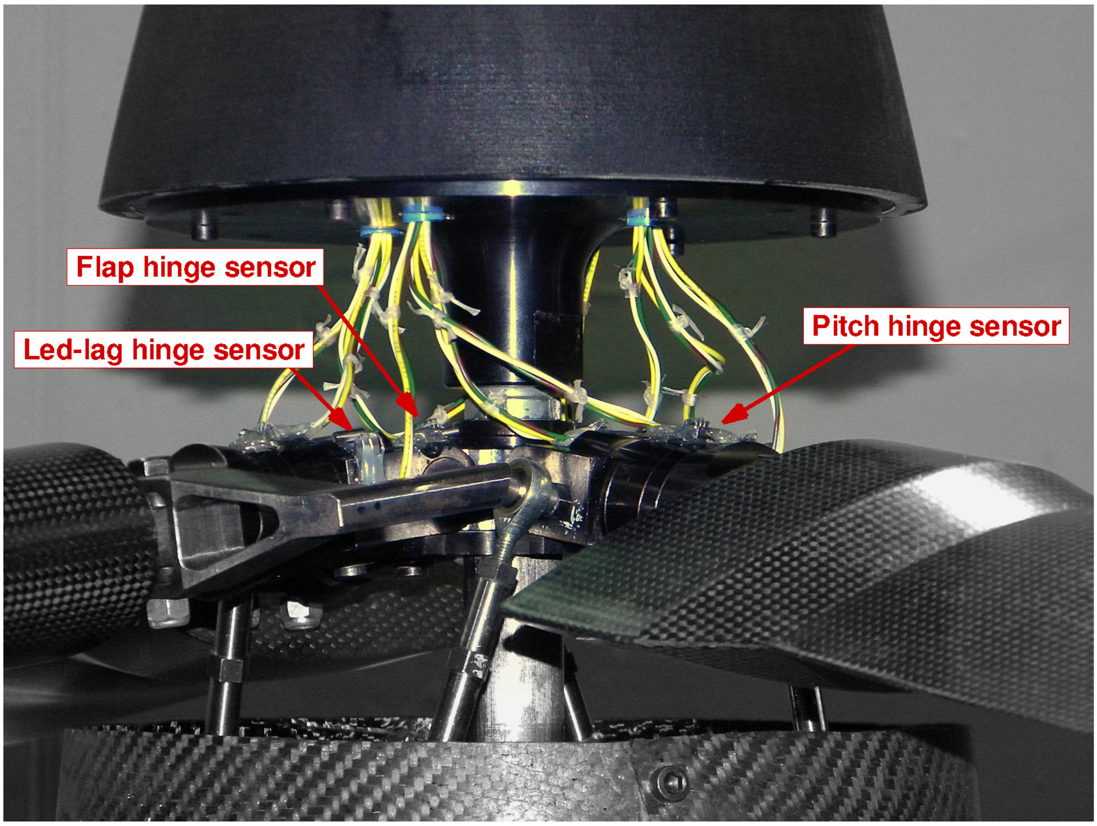

Figure 3.16: *Rotor hub detail: pitch, led–lag and flap hinges with Hall effect sensors.*

Blade hinge		Achievable values		Calibration range	
		Maximum [deg]	Minimum [deg]	Maximum [deg]	Minimum [deg]
Flap angle	β	50	-4.5	10	-4
Led–lag angle	ζ	8	-16	8	-16
Pitch angle	θ	40	-30	22	-10

Table 3.2: *Maximum and minimum angular value achievable by flap, led–lag and pitch hinges.*

Alnico magnets have been employed on each blade hinge, as shown in Figure 3.16. The sensors used were high accuracy SS496A1 model with 3 pin by Honeywell which have a ratiometric output voltage, set by the supply voltage $(4/9\ V)$. It varies in proportion to the strength of the magnetic field produced by the magnet. The sensor integrated circuit chip provide high accuracy (null to $\pm 3\ \%$, sensitivity up to $\pm 3\ \%$) and temperature compensation to reduce null and gain shift over temperature. The power supply (supply current $10\ mA$) and the signal of all the sensors went through the rotor shaft by passing in the ogive and came out from the slip ring. The Hall effect sensors calibration has been carried out insitu of the rotor model only once all the sensors and all the magnets have been placed in their final position. This way of proceeding was necessary in order to avoid modification of the magnetic fields of the magnets. The calibration procedure has been made one hinge by one by blocking the other two hinges in the neutral position and has been repeated for each blade. While the range achievable by each hinge was very wide, we were interested in limited pitch variation $(-2^\circ \div 14^\circ)$ which means also limited variation in flap and led–lag. Due to this and since it is not easy to find a calibration curve for high displacements of the magnet with respect to the sensor, they have been calibrated in a lower angular range. In Table 3.2 are reported both the minimum and the maximum angular values achievable by each hinge and the minimum and the maximum angular values in which the calibration has been carried out for that hinge. In Table 3.2, the flap angle is positive upwards, the led–lag angle is negative ahead and the pitch angle is positive nose up. Finally, it should be noted that different calibration procedures have been adopted for the flap and pitch sensors with respect to the lag sensors. In particular, the flap and pitch sensors have been calibrated with an inclinometer placed on the blade cuff while the calibration of the led–lag sensors have been carried out by means of an optical method. Consequently, the uncertainties have been evaluated from the calibrations as the maximum of the standard deviation (σ). For the flap and pitch sensors this value was $\pm 0.1°$ while for the led–lag sensors it was $\pm 1°$. In the following, every time the flap, led–lag and pitch measured values should be reported, the mean values between the four sensors will be used instead of the single blade value. For this reason, we will use for a given mean angular value an uncertainty that will be equal to the root sum square of the uncertainties of each single value.

3.3 Blade experimental model

The structural design of the experimental blade model has been carried out by means of a FEM (Finite Element Method) approach. Since the model was not aeroelastic, the blade was designed with the goal of being stiff but not too heavy. These requirements have been fulfilled making use of unidirectional (Prepreg carbon fibre with $160\ g/m^2$ of density and $0.153\ mm$ of thikness) and bidirectional (Prepreg carbon fibre with $200\ g/m^2$ of density and $0.180\ mm$ of thickness) high modulus carbon fibre both for the external skin and for the spar. In particular, as shown in Figure 3.17, the internal structure of the blade was made by a spar and a leading edge module. The spar was constituted by a pre–shaped foam core made of Rohacell®WF [5] (with $110\ kg/m^3$ of density and process pressure up to $0.7\ MPa$, temperatures up to $130°\ C$) and covered by 2–layers of unidirectional and 4–layers of bidirectional carbon fibre. The leading edge module was a pre–shaped foam module of Rohacell®WF on which the laminated

Figure 3.17: *A schematic view of the internal and external structure of the blade.*

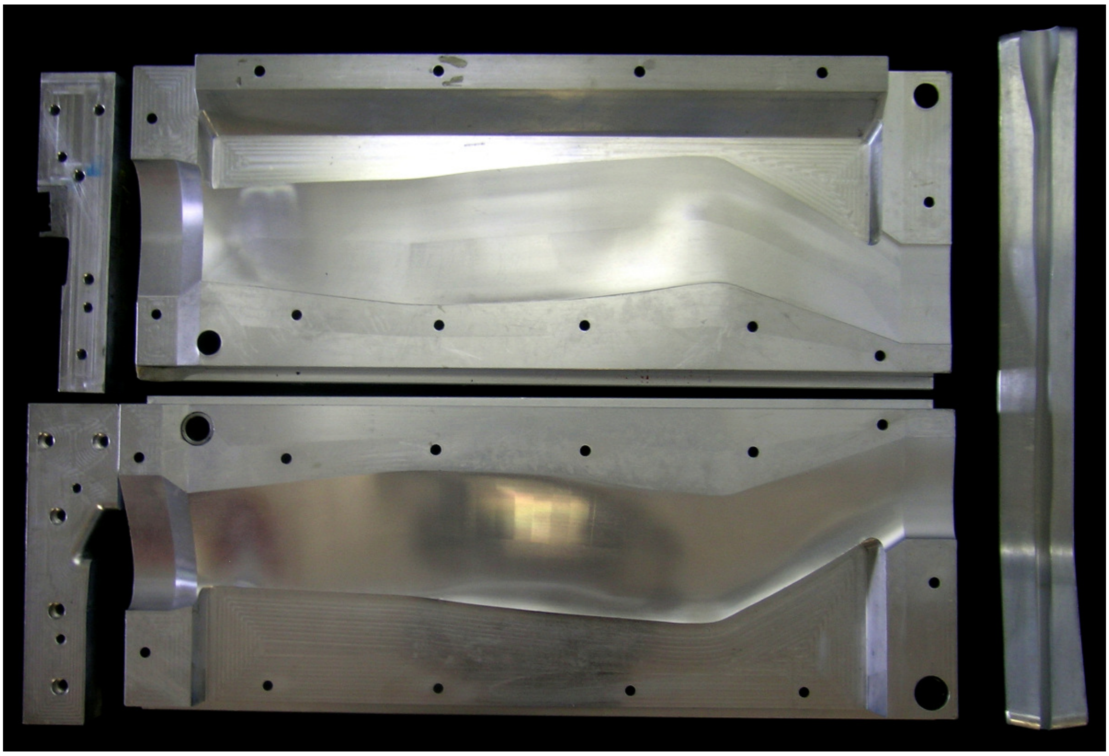

Figure 3.18: *View of the blade mould components.*

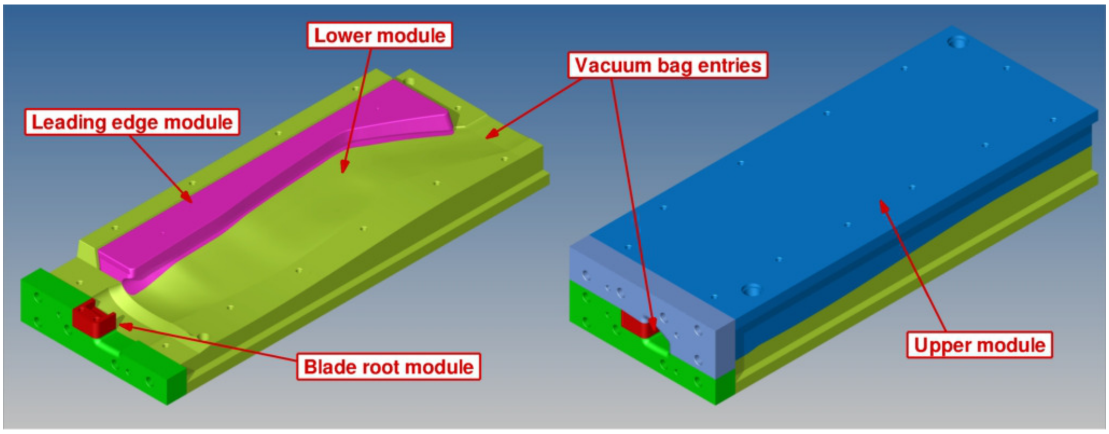

Figure 3.19: *A schematic view of the blade mould with the components highlighted.*

spar was laid down. This composite structure was than inserted in the blade mould together with 3–layers of bidirectional carbon fibre representing the blade external skin. The blade mould, shown in Figure 3.18 and 3.19, was composed by three main components reproducing one the leading edge (to guarantee that the local surface was correctly shaped in this region) and the other two the lower and the upper surfaces of the blade. A small support block (in red in Figure 3.19) was employed to fasten the blade spar on the mould. During the curing process, that has been carried out in the autoclave, a vacuum bag was used instead of a foam module in the rear zone of the blade to adhere the carbon fibre to the mould surface in that region.

3.4 Measurement techniques

As already pointed out in Section 3.1, only the hovering flight condition has been considered in this work. With the aim to describe the phenomena related to the aerodynamic interaction between the half–wing and the corresponding rotor on a tiltwing tiltrotor aircraft, we decided first to study the performance of the aircraft in hover by means of force measurements. Moreover, to better understand how the flow field below the rotor plane changes when the wing is taken into account, we performed PIV (Particle Image Velocimetry) measurements on several planes around the model. No corrections were applied on measurement results.

To drive the rotor system we used two different remote control system devices. The first one was the hydraulic motor driving system which allowed to drive the rotor engine and permitted to verify its rotational speed. The second control device was the rotor command console system which allowed to manage the collective, longitudinal and lateral pitch controls (see Figure 3.15). Since the rotor rotational speed was fixed during all the tests ($n = 1120\ rpm$), in order to change the rotor thrust, only a collective pitch command was given to the blades. When necessary, the rotor trim condition was changed only by managing the collective pitch command on the rotor command console (the three electric actuators were moved together to change the position of the swashplate).

3.4.1 Force measurement setup

The experimental test rig has been designed to study the performance of the tiltwing aircraft by means of rotor and wing force and moment measurements. A PXIe–1078 by NI (National Instruments) has been used to employ the acquisition system and the signals acquisition has been carried out by means of different NI devices. The aerodynamic loads given by the rotor have been measured by the rotor balance (JR3 E Series, accuracy $0.25\ \%$ FS) which has been acquired with the NI PXI–6123 device. The rotor torque signal given by the instrumented holed shaft has been acquired with a NI compact data acquisition system cDAQ–9178 equipped with the 9237 module. On the same NI compact data acquisition system, three NI 9215 modules have been used to measure the 12 blade angles given by the Hall effect sensor signals while a NI 9237 module has been employed to acquire the signal of the Hall effect sensor located in front of the rotor shaft. Forces and moments acting on the wing have been measured by a seven–component strain gauge balance (the maximum estimated error on the measured loads is less than $0.22\ N$) located at the wing root and fixed on a traversing system. The balance signals have been acquired by using a dedicated NI compact data acquisition system cDAQ–9174 equipped with five NI 9237 modules. The software used for the acquisition has been implemented in LabVIEW [38]. The acquisition frequency used by the system to acquire the transducer signals was $2.5\ kHz$ for a time period of $5\ s$. At the end of the acquisition process, all the signals were post–processed by keeping the mean in time of each of them.

3.4.2 PIV measurement setup

To better understand the behaviour of the rotor wake impinging on the wing, an extensive PIV campaign has been carried out on both the isolated rotor and the tiltwing model in the tilted configuration. The PIV setup of the DSTA Aerodynamics Laboratory of Politecnico di Milano [86] has been employed to acquire images of the flow field on vertical planes below the rotor with and without the wing installed. The PIV setup of the DSTA Aerodynamics Laboratory allows for 2D flow field surveys on a give plane window. The PIV system is composed by a Dantec Dynamics Nd:YAG double pulsed laser with $200\ mJ$ output energy and a wavelength of $532\ nm$ and a Imperx double shutter CCD camera with a $12\ bit$, 1952×1112 pixel array. The laser has been alternatively mounted in a vertical position below the rotor to light radial planes and in front of the tilted wing to light different azimuthal planes along the wing span. The camera has been mounted on a single axis traversing system to move the mea-

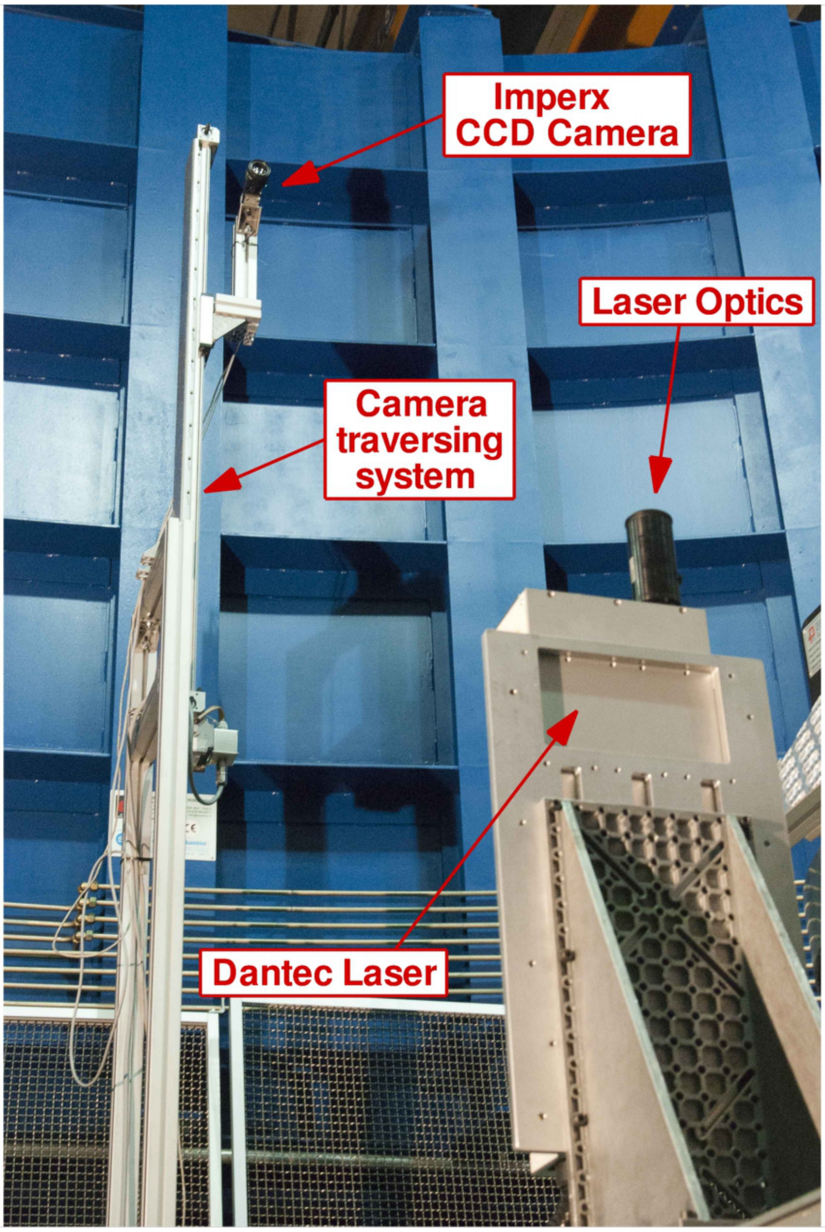

Figure 3.20: *An example of the PIV setup of the DAST Aerodynamics Laboratory.*

surement window in vertical direction. To avoid the transfer of vibrations to the PIV measurement devices, both the laser and the camera were fixed on heavy basements. An example of the PIV setup is given in Figure 3.20. The synchronisation of the two laser pulses with the image pair's exposure has been controlled by a 6 channels Quantum Composer pulse generator. The trigger signal used to drive the laser pulses and the camera was the signal given by the Hall effect sensor placed in front of the rotor shaft. A particle generator PIVpart30 by PIVTEC with Laskin atomizer nozzles has been used for the seeding. PIV surveys were done alternatively in azimuthal and radial planes and for different azimuthal blade angles. For each run the velocity flow fields were phase averaged over 100 image pairs. The image post–processing has been carried out by PIVview 2C software [68] developed by PIVTEC.

CHAPTER 4

Force measurements in hover

In this chapter we present the aerodynamic analysis of the tiltwing half–model described in the previous chapter by means of force and moment measures. The flight condition tested was the hovering flight in helicopter mode. The rotor performance and the influence of the model airframe on the rotor were studied in terms of rotor thrust coefficient C_T and power coefficient C_P, Figure of Merit FM and wing forces. The isolated rotor tests are first discussed to characterise the performance of the rotor without the wing. Then experimental data are compared with steady CFD calculations performed on the isolated blade in the $90°$ cylindrical sector. Hereinafter the wing is taken into account and the effects of the wing on the rotor and vice–versa are described. The influence of the wing configurations (in terms of tilt angle and relative position with respect to the rotor) are also analysed.

4.1 Isolated rotor performance

The first experimental test was conducted on the isolated rotor to characterise the rotor performance at different C_T without the airframe interaction. The experimental data acquired in this case will be use as the reference condition to evaluate the rotor performance of the whole tiltwing half–model. In Figure 4.1 the experimental test rig for the isolated rotor tests is shown. In Figure 4.2 the FM of the rotor has been reported as function of C_T/σ at the nominal tip Mach number $M_{Tip} = 0.32$ while the power coefficient C_P has been shown in Figure 4.3 as function of C_T. In these figures the standard deviations of the rotor coefficients and FM are plotted on the experimental curves. The standard deviation has been evaluated by taking into account the accuracy of the rotor instruments together with the measurement repeatability. The evaluation of the measurement repeatability has been carried out over 40 measurement points acquired

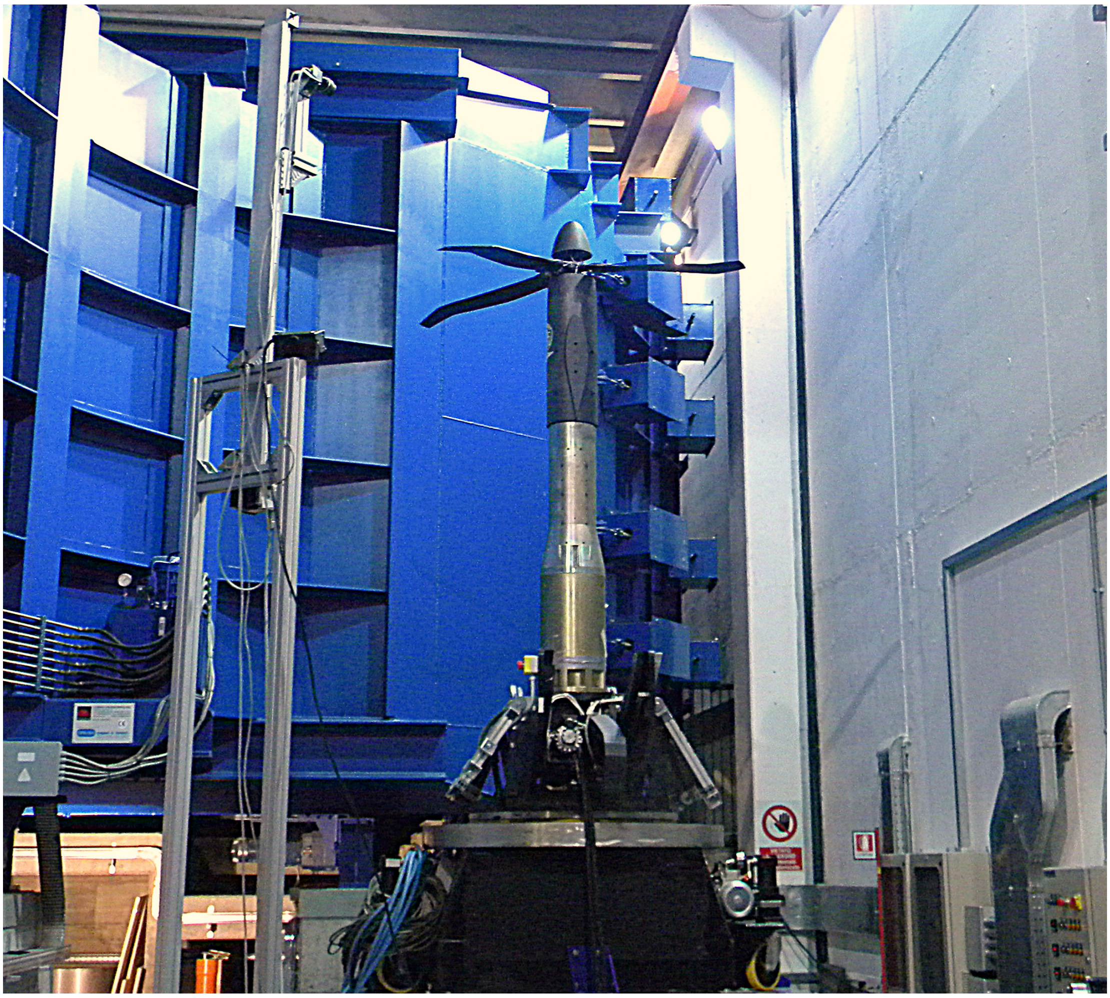

Figure 4.1: *View of the isolated rotor test rig for hover tests.*

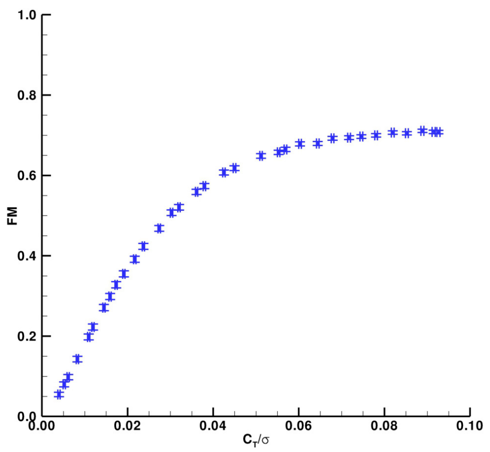

Figure 4.2: *Isolated rotor performance: FM as function of C_T/σ at $M_{Tip} = 0.32$.*

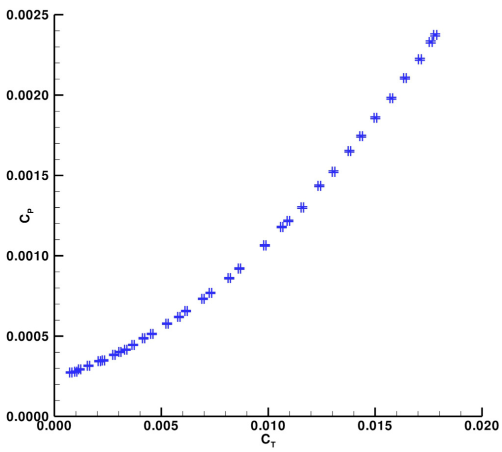

Figure 4.3: *Isolated rotor performance: C_P as function of C_T at $M_{Tip} = 0.32$.*

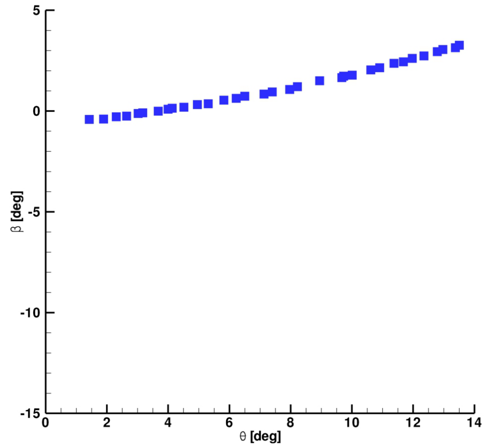

Figure 4.4: *Isolated rotor performance: mean values of β as function of θ at $M_{Tip} = 0.32$.*

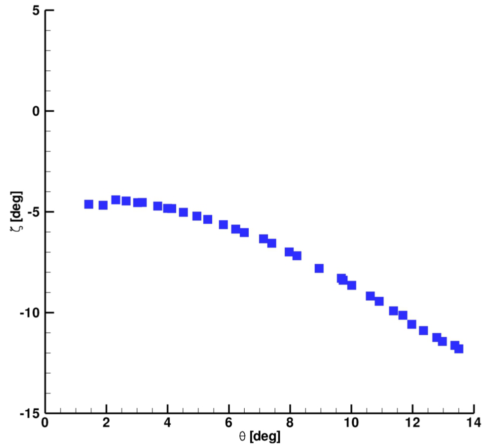

Figure 4.5: *Isolated rotor performance: mean values of ζ as function of θ at $M_{Tip} = 0.32$.*

for $\theta = 12°$. The maximum value of FM achieved during the tests is 0.71 and it was obtained for $C_T = 0.0178$ and for $C_P = 0.0023$. However the maximum value of C_T achieved during the experiments was 0.0180 and was slightly lower than the design value in hover ($C_T^H = 0.0215$). Although the declared maximum power of the hydraulic pump which drove the motor was $16\ kW$, the power given by the motor was limited by the engine capacity. Therefore the maximum power achieved during all the tests was about $8.5\ kW$ at $n = 1120\ rpm$ for a collective pitch of about $13°$. In Figure 4.4 and 4.5 the mean values of the flap β and the led–lag ζ angles of the four blades have been reported as function of the mean value of the blade pitch angle.

4.1.1 CFD calculation for the isolated rotor

For the isolated rotor in hover, numerical simulation have been performed with the CFD code ROSITA (see Appendix A) to validate the numerical predictions on the model case by comparing the results with the experimental data acquired during the test. Moreover, since we are not able to test the real rotor, the comparison between experimental and numerical results for the isolated rotor model allows to verify the quality of the numerical prediction that have been used during the blade design phase (see Section 2.2) for the full–scale aircraft. For this reason, CFD calculations have been carried out by means of the same computational grids that have been previously used in the blade tip refinement process (see Section 2.2.4 for grid details). The isolated rotor performance are shown in terms of FM, C_T and C_P in Figures from 4.6 to 4.9. In particular, Figure 4.6 and 4.7 show respectively the comparison between the FM and the thrust and power coefficients measured in laboratory and predicted by the CFD code. The agreement between the results is quite impressive. The same result can be found by analysing the trend of the thrust and the power coefficients as function of the mean blade pitch angle θ, as shown in Figure 4.8 and 4.9. It has to be noted that only in the range between $7°$ and $10°$ of mean pitch angle, the thrust and the power coefficients are slightly over predicted by the CFD solver.

Since the agreement between experimental data and numerical calculations was very good, the CFD simulations have been carried out for blade pitch angles higher than the highest measured value of θ (that was $13.5°$). In Figures from 4.6 to 4.9 the CFD pre-

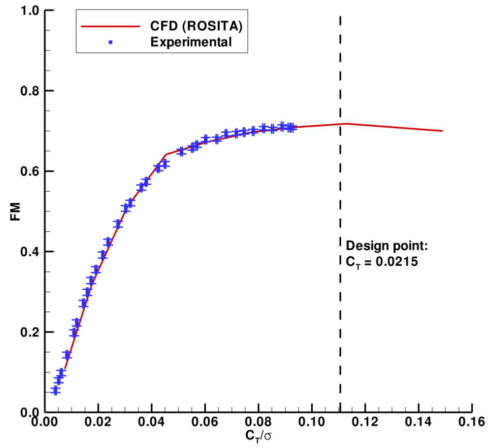

Figure 4.6: *Comparison between experimental data and CFD calculation for the isolated rotor: FM as function of C_T/σ, $M_{Tip} = 0.32$.*

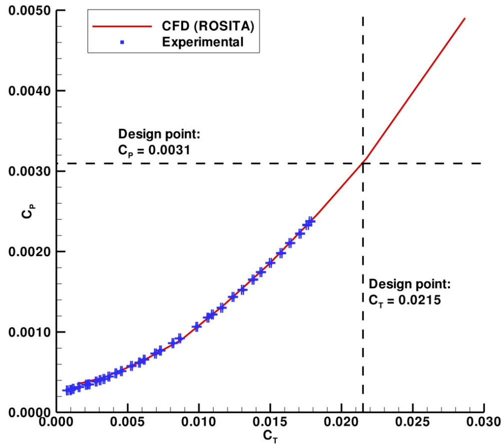

Figure 4.7: *Comparison between experimental data and CFD calculation for the isolated rotor: C_P as function of C_T, $M_{Tip} = 0.32$.*

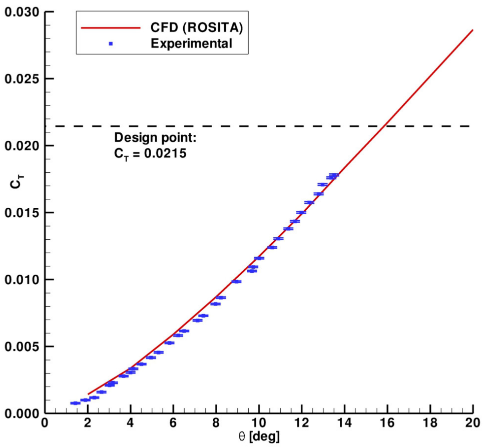

Figure 4.8: *Comparison between experimental data and CFD calculation for the isolated rotor: C_T as function of θ, $M_{Tip} = 0.32$.*

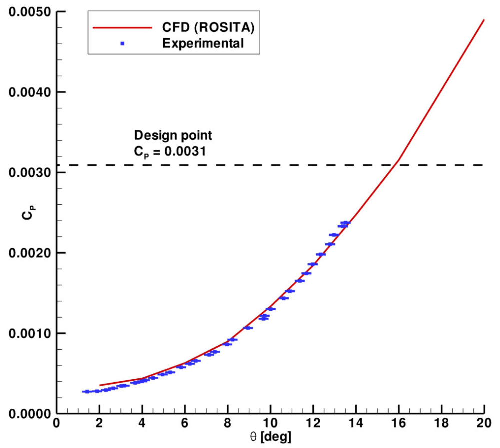

Figure 4.9: *Comparison between experimental data and CFD calculation for the isolated rotor: C_P as function of θ, $M_{Tip} = 0.32$.*

diction are ported for a blade pitch angle up to $20°$. The hover design point is also highlighted in these figures. In this condition however, the power coefficient ($C_P = 0.0031$) and the blade pitch angle ($\theta = 15.5°$) were different with respect to the predicted ones at full–scale. Since in the test condition the tip Mach number was $1/2$ the tip Mach number of full–scale aircraft at design point in hover, the power losses due to compressibility effects at the blade tip were significantly lower than in the full–scale case. Thereby, in the test condition the power required to hover was slightly less than in the full–scale case.

Figure 4.10 and 4.11 show the results of a grid dependence study for the steady simulations on the isolated rotor blade in the $90°$ cylindrical sector. Numerical simulations have been carried out on three different grids (Coarse, Intermediate and Fine) to assess the reliability of the results previously presented in this paragraph. By using the grid described in Section 2.2.4 as the intermediate grid (Baseline grid), the Coarse and Fine

Grid	Blade grid		Background grid		Total
	Blocks	Cells ($\times 10^6$)	Blocks	Cells ($\times 10^6$)	($\times 10^6$)
Baseline	8	3.2	1	1.2	4.4
Coarse	8	1.4	1	0.8	2.2
Fine	8	5.2	1	1.5	6.7

Table 4.1: *Characteristics of the blade grids for the grid dependence study.*

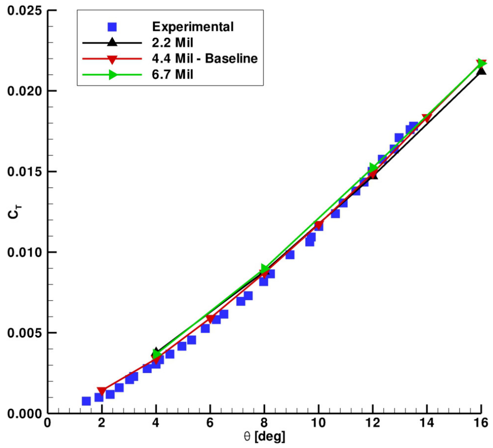

Figure 4.10: *Grid dependence study for the isolated rotor case and comparison with experiments: C_T as function of θ, $M_{Tip} = 0.32$.*

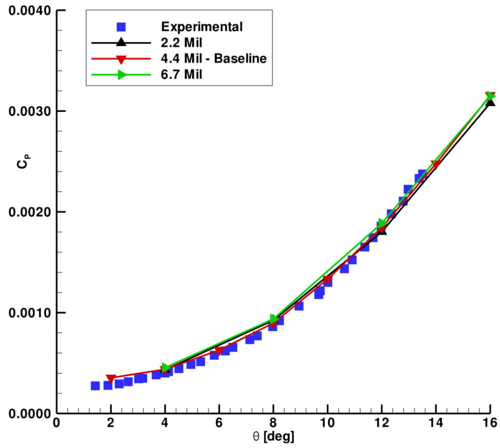

Figure 4.11: *Grid dependence study for the isolated rotor case and comparison with experiments: C_P as function of θ, $M_{Tip} = 0.32$.*

meshes have been respectively obtained starting from this mesh. The total number of grid points ranges from 2.2×10^6 to 6.7×10^6 cells. Grid density has been varied in both the blade and the background grids while the location of their boundaries have not been changed [10]. For these reasons, in order to generate the blade Coarser grid, both the chord–wise and span–wise edges spacing have been relaxed slightly. Also the trailing edge spacing has been relaxed reducing the wake resolution. On the contrary, the finest grid has been designed increasing the edges spacing in all directions. The background grid has been adapted to mach correctly the blade inner grid in both cases. The different grid systems investigated are detailed in Table 4.1. By looking at the thrust and the power coefficient curves, the solutions computed for the different grids were quite similar one to each other. However, numerical results obtained with the Baseline and the Fine grids appeared to be in better agreement than the ones given by the Coarse grid if compared with the experimental data, especially for the higher values of the pitch angle θ. In conclusion, the agreement between the experimental data and the numerical prediction obtained with the Baseline and the Fine grids sustain the numerical results presented.

4.2 Effects of the wing on rotor performance

After the isolated rotor tests, we placed the wing under the rotor to simulate the whole tiltwing aircraft. As already described by McVeigh [57] and by Felker and Light [25], when the wing is taken into account the rotor performance change with respect to the isolated case. In particular, as shown by McCluer and Johnson [56] for the Full–Span Tiltrotor Aeroacoustic Model (FS TRAM), the rotor FM is strongly affected by the presence of the airframe and considerably decreases with respect to the isolated rotor case [45]. To study the effects that the wing yields on the rotor performance, we analysed first the influence of the wing configuration and then the dependence of the rotor performance from the wing–rotor distance (h^w).

The aircraft reference system has been presented in Figure 3.3. As described in Section 3.1, the rotor and the half–wing were independent systems, thus the aerodynamic loads acting on the wing were measured only by the wing balance while the rotor balance measured only the aerodynamic forces generated by the rotor without considering the wing loads. For this reason, to express the effective airloads given by the rotor in the aircraft system, the vertical wing force F_z^w have been added to the rotor thrust F_z^r. The net value of rotor thrust can be expressed as follows:

$$T_{net} = F_z^r + F_z^w, \tag{4.1}$$

and the FM of the rotor in the half–wing model configuration can be calculated using Equation 4.1 for the thrust. In the following, every time the rotor thrust should be used, the net thrust value will be employed instead of the vertical force read by the rotor balance unless otherwise indicated.

4.2.1 Influence of the wing configuration

We started the analysis taking into account the two opposite wing configurations. As shown in Figure 4.12 and 4.13, the untilted ($\theta^{Tilt} = 0°$) and the tilted ($\theta^{Tilt} = 90°$) configurations were tested to understand how the airframe affects the rotor performance in hover. Figure 4.14 shows the rotor FM as function of C_T/σ while Figure 4.15 displays the rotor performance in terms of C_P as function of C_T. In both cases, the two wing configurations are presented together with the isolated rotor case data. Both the rotor FM and the thrust and power coefficients are strongly influenced by the presence of the wing when it was untilted. In particular, it is evident how the rotor thrust is affected by the partial ground effect due to the wing surface. Although the thrust should be positively influenced by the partial ground effect, the vertical force F_z^w developed on the wing in the opposite direction of the rotor thrust had the effect to reduce the net rotor thrust for a given trim condition. A practical consequence of this fact is that for a given thrust, the power required to hover is so much more than in the isolated case (we measured an increment of about 21 $\%$ at $C_T = 0.014$). It follows that also the rotor FM is very low if compared with the isolated case. On the other hand, the tilted wing showed a very different behaviour. In fact, the experimental results demonstrate that minimising the wing surface on which the rotor wake strikes (i.e. by rotating the outer portion of the wing) the influence of the wing on the rotor performance is substantially negligible. So the rotor performance are very similar to the performance of the isolated hovering rotor. Even though this result is rather intuitive, in our opinion it is an interesting result because in the past literature there is no evidence of it. Actually, in the frame of the ERICA project [4], some experimental tests have been carried out on half and full–span models but the data are not public. Furthermore, the experimental evidence of the possibility to neglect the tilted wing influence on the rotor performance

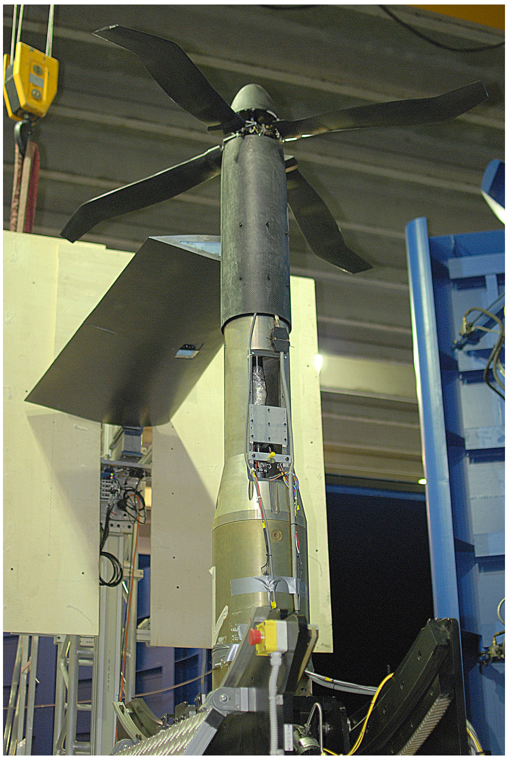

Figure 4.12: *Half–model for hover tests in the untilted configuration.*

Figure 4.13: *Half–model for hover tests in the tilted configuration.*

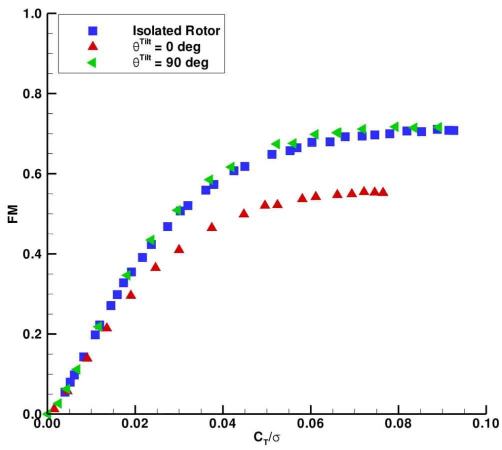

Figure 4.14: *Effect of the wing configuration on the rotor performance: FM as function of C_T/σ, $M_{Tip} = 0.32$.*

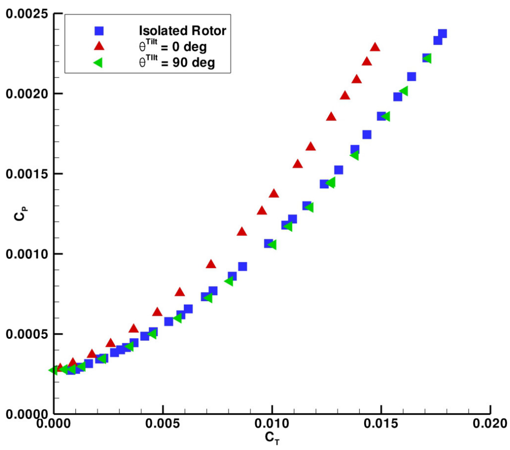

Figure 4.15: *Effect of the wing configuration on the rotor performance: C_P as function of C_T, $M_{Tip} = 0.32$.*

in hover validates the initial hypothesis for the assessment of the required thrust to hover in the blade design (see Flight Condition 1 in Table 2.3 of Section 2.2).

4.2.2 Influence of the wing vertical position

In Section 2.3 we chosen the span–wise location of the tilting section on the half–wing of the full–scale aircraft by taking a plausible value of the wing–rotor distance

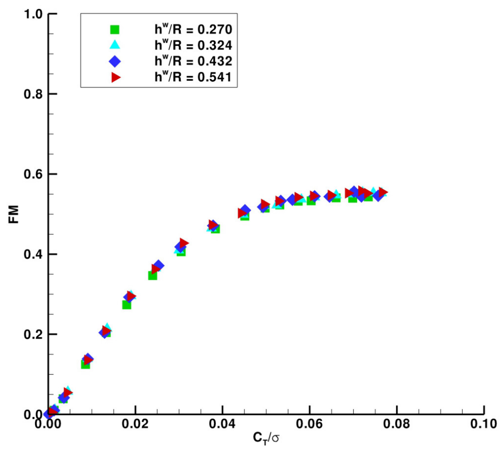

Figure 4.16: *Effect of the wing distance on the rotor performance:* FM *as function of* C_T/σ, $M_{Tip} = 0.32$, $\theta^{Tilt} = 0°$.

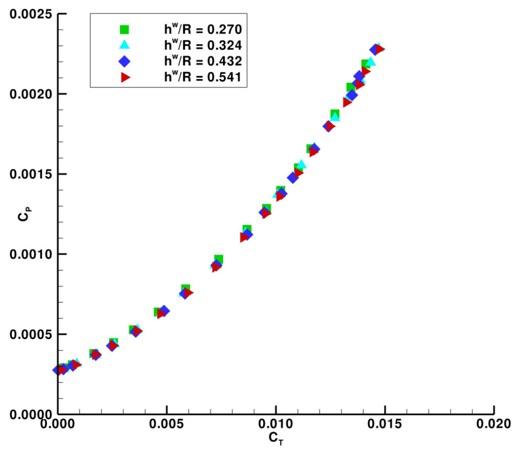

Figure 4.17: *Effect of the wing distance on the rotor performance:* C_P *as function of* C_T, $M_{Tip} = 0.32$, $\theta^{Tilt} = 0°$.

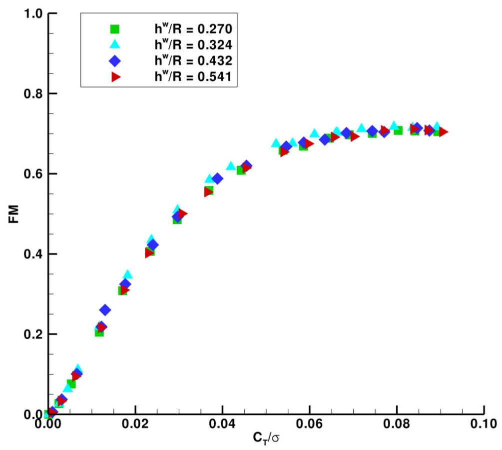

Figure 4.18: *Effect of the wing distance on the rotor performance:* FM *as function of* C_T/σ, $M_{Tip} = 0.32$, $\theta^{Tilt} = 90°$.

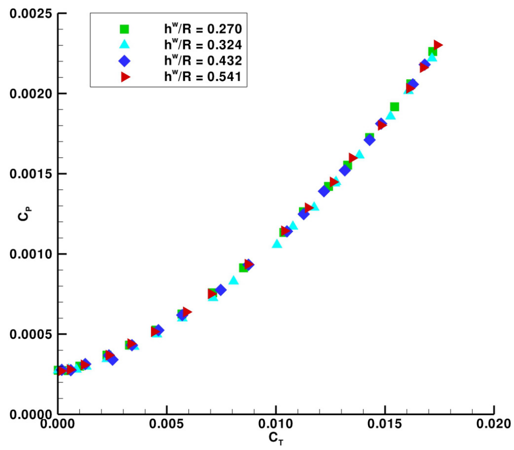

Figure 4.19: *Effect of the wing distance on the rotor performance:* C_P *as function of* C_T, $M_{Tip} = 0.32$, $\theta^{Tilt} = 90°$.

h^w by comparison with the existing tiltrotor models. This choice was made because there are no data available in literature showing the influence of this parameter on both rotor performance and wing loads in hover condition. In this regards, we carried out several experimental tests to study the effects of the variation of h^w keeping the design distance as the reference value. Tests were made at four distances h^w both for the untilted and tilted wing configurations. The rotor FM is presented as function of C_T/σ in Figure 4.16 and the power coefficient is reported ad function of the thrust coefficient in Figure 4.17 for the untilted wing configuration. The same rotor quantities are used to show the results for the tilted case in Figure 4.18 and 4.19. As it is apparent from the results, in the tilted configuration the rotor performance in hover are not affected by the variation of the distance between the rotor and the wing. Also in the untilted configuration no significant changes have been observed with the only exception of the case for $h^w/R = 0.270$ where there is a reduction of about $1\ \%$ in peak of rotor

FM compared to the reference distance $h^w/R = 0.324$. The reduction in performance is attributed to the proximity of the untilted wing surface to the rotor plane. At this distance the rotor slipstream was not completely contracted and the wing surface over which the rotor wake struck was higher than the other cases. As it will be shown in Section 5.1, PIV measurements on the isolated rotor demonstrated that, although the rotor slipstream maximum contraction is reached at an higher distance, the axial velocity component at $h^w/R = 0.270$ is high enough to produce an aerodynamic load on the wing that significantly decreased the rotor net thrust.

4.3 Effects of the rotor wake on the wing

In general, when a tiltrotor aircraft operates in helicopter mode, the rotor wake that strikes on the upper surface of the wing generates a three–dimensional flow producing competing aerodynamic interactions that are responsible for loss of rotor performance (as described in Section 4.2) and wing download. The rotor wake impinging on the airframe creates a non–negligible vertical force pointing in the opposite direction of the rotor thrust. In tiltrotor with conventional aerodynamic layout this contribution is about $10\ \%$ of the rotor thrust [24], [57] when only the wing is considered and about $15\ \%$ [85] when also the airframe is modelled. It is known that the main contributing factors to tiltrotor download are the pressure drag that grows on the wing and the force developed on the fuselage and due to the side–by–side rotor interaction, as described by Wood and Peryea [84]. In a tiltwing aircraft however, the capability to rotate the outer part of the wing minimises the contribution due to the pressure drag on the wing, while the reduced rotor diameter avoids the rotor–rotor interaction in proximity of the fuselage. The reduced aerodynamic force on the wing due to the tiltwing configuration was investigated by analysing two different wing configurations. As already done in the understanding of the rotor performance, the influence of the wing–rotor distance was also analysed.

As stated in Section 3.1, all the experimental tests were conducted at a M_{Tip} that is $1/2$ the full scale M_{Tip}. Nevertheless, the ratio between the aerodynamic forces acting on the wing and the rotor thrust should be independent of the M_{Tip} because there are no important Reynolds number effects present, as shown by McVeigh (Ref. [57]). In fact, from the simple momentum theory [44] we know that for a given thrust coefficient the induced axial velocity in the rotor slipstream is equal to $2\Omega R\sqrt{C_T/2}$. However, the Reynolds number based on the model wing chord and the slipstream velocity is $R_e = 2 \times 10^6$ at the full–scale M_{Tip} and $R_e = 1 \times 10^6$ in the actual test condition. In the following, the forces acting on the wing have been expressed in the reference system illustrated in Figure 3.3.

4.3.1 Influence of the wing configuration

The aerodynamic influence given by the rotor wake impinging on the wing has been investigated for two wing configurations (untilted and tilted). When the rotor wake strikes on the surface of the wing, an aerodynamic force F_z^w parallel to the z–axis (i.e. the thrust direction) was generated, as shown in Figure 4.20. When the untilted configuration was taken into account, the F_z^w on the wing was negative in the aircraft reference system (download) and the highest force/thrust ratio (about $41\ \%$) was obtained at a very low $C_T/\sigma = 0.006$. The force/thrust ratio decreases for higher value of C_T/σ reaching an asymptotic value of $20.1\ \%$ at $C_T/\sigma = 0.063$. The vertical force/thrust ratio trend in the untilted case appears to be in good agreement with the results shown by Young et all. [85] for the V–22 full–span model, even though the measured value for the V–22 model are slightly lower. A drastic reduction of the vertical force F_z^w acting on the wing was observed on the tilted configuration. In spite of the force/thrust ratio is less than $1\ \%$ for all the C_T/σ tested, for C_T/σ greater than 0.058 the force/thrust ratio is slightly positive (upload). Since the rotated part of the wing is immersed in the rotor wake, the flow field is characterised by a non–negligible swirl component. Due to this and thanks to the rotor sense of rotation (counterclockwise), the wing sections have a negative angle of attack with respect to the flow impinging on it. Thereby, the F_z^w component of the aerodynamic force which raises on the wing is pointed upward. However, in the tilted configuration the F_z^w component is not the highest component of the aerodynamic force. In fact, the longitudinal force F_x^w, as shown in Figure 4.21 as a fraction of the rotor thrust, is higher than F_z^w and it is always positive. For C_T/σ higher than 0.02 the longitudinal force/thrust ratio is nearly constant (about $4.5\ \%$). This result means that in hovering flight the aircraft should be subject to a non–negligible aerodynamic force that is pointed backward. Also this effect is due to the non–zero swirl component on the rotor slipstream. On the other hand, in the untilted configuration the longitudinal force on the wing is almost zero.

The present results for the tilted wing configuration ($\theta^{Tilt} = 90°$), together with the results shown in Section 4.2, demonstrate that the tiltwing solution can offer some important advantages with respect to the conventional tiltrotors. In particular, it is evident that the tiltwing configuration requires low thrust and power to hover since the rotor does not have to give extra thrust to balance the wing download because this effect is not present. However, while the small F_z^w upload observed is probably not sufficient to give real benefits in terms of aircraft performance, the longitudinal force F_x^w should produces negative effects in the first part of the conversion phase. As it will be shown in Chapter 5, since the tilted portion of the half–wing is immersed in the rotor slipstream, both the components (F_z^w and F_x^w) of the aerodynamic force acting on the wing are a

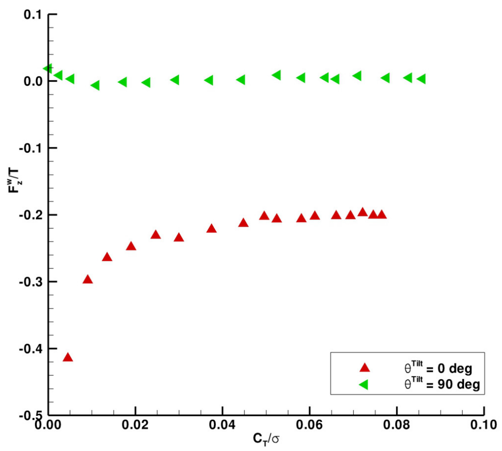

Figure 4.20: *Effect of the wing configuration on its vertical force: F_z^w/T as function of C_T/σ, $M_{Tip} = 0.32$.*

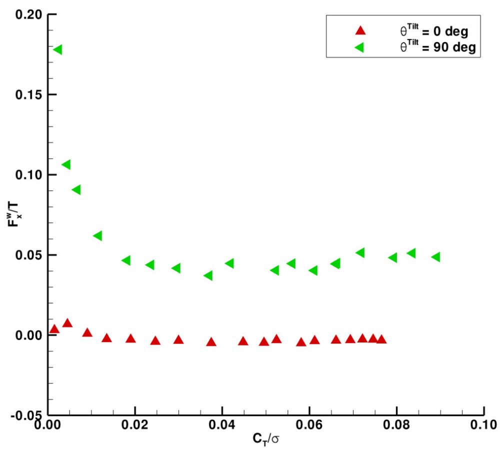

Figure 4.21: *Effect of the wing configuration on its longitudinal force: F_x^w/T as function of C_T/σ, $M_{Tip} = 0.32$.*

consequence of the swirl component of the rotor wake. It is also true that, to reduce the effect of the swirl, the tilt angle θ^{Tilt} in hover should be changed in order to have a zero induced angle of attack on the main part of the tilted wing.

4.3.2 Influence of the wing position

Using the traversing system of the wing, the relative distance between wing and rotor has been changed and several wing positions have been investigated. The wing–rotor distance analysed were the same of Section 4.2.2. Figure 4.22 and 4.23 show the vertical and lateral loads acting on the wing as function of C_T/σ at four different wing–rotor distances h^w/R for the untilted case. Figure 4.24 and 4.25 show the same results for the tilted wing configuration. Apparently, the variation of the rotor–wing distance has no significant effects on trend of the aerodynamic force components of the wing in

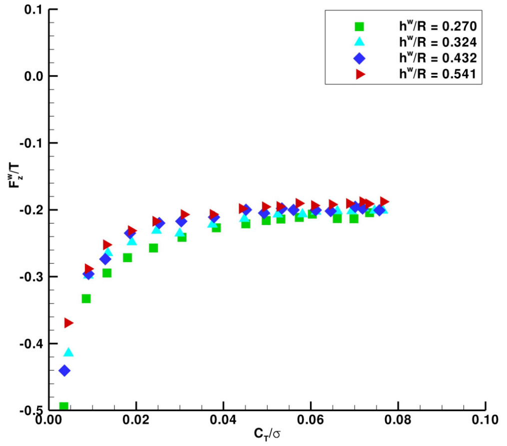

Figure 4.22: *Effect of the wing distance on its vertical force: F_z^w/T as function of C_T/σ, $M_{Tip} = 0.32$, $\theta^{Tilt} = 0°$.*

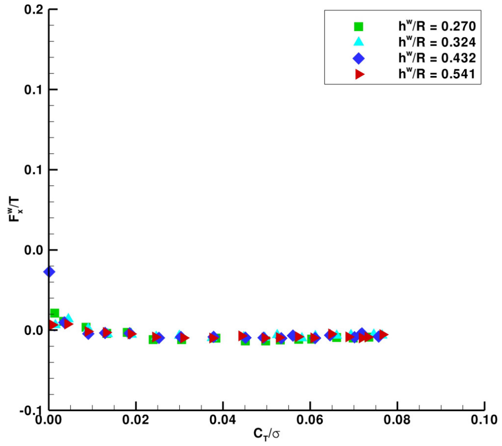

Figure 4.23: *Effect of the wing distance on its longitudinal force: F_x^w/T as function of C_T/σ, $M_{Tip} = 0.32$, $\theta^{Tilt} = 0°$.*

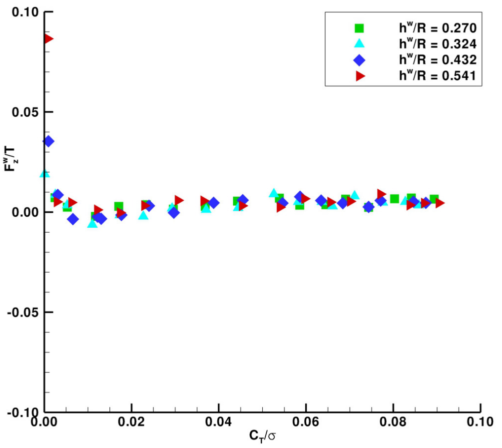

Figure 4.24: *Effect of the wing distance on its vertical force: F_z^w/T as function of C_T/σ, $M_{Tip} = 0.32$, $\theta^{Tilt} = 90°$.*

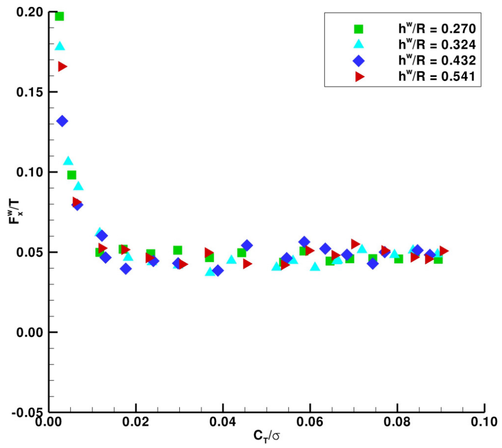

Figure 4.25: *Effect of the wing distance on its longitudinal force: F_x^w/T as function of C_T/σ, $M_{Tip} = 0.32$, $\theta^{Tilt} = 90°$.*

the titled configuration. However, while the vertical load assumes essentially the same value for a given C_T/σ in all the configurations tested, for $C_T/\sigma > 0.02$ the lateral load varies between a maximum value of 5.6 % for $h^w/R = 0.432$ (at $C_T/\sigma = 0.058$) to a minimum value of 3.9 % for $h^w/R = 0.324$ (at $C_T/\sigma = 0.038$). On the other hand, when the untilted wing configuration is analysed the effects of different wing–rotor distances were apparent only for F_z^w/T. In fact, while the vertical load on the wing diminishes as the distance increases, as shown in Figure 4.22, the longitudinal load is the same for all the distances considered, as reported in Figure 4.23.

4.3.3 Comparisons between CFD and experiments

The vertical and lateral load have been predicted by means of CFD calculations for the design wing–rotor distance $h^w/R = 0.324$ in the tilted configuration. Numerical simulations have been performed with the CFD code ROSITA (see Appendix A). As already done for the design of the tilt wing section, an half–model configuration reproducing one half–wing together with the rotor and the nacelle has been taken into account to build the computational grid. Steady calculations have been used to numerically evaluate the effects of the rotor wake on the wing at several C_T/σ in the experimental tests conditions. However, since the flow field in which the wing is immersed is completely unsteady, steady computations allow to resolve the mean loads developing on the wing without give any information on the loads time dependency. Moreover, steady simulations cannot take into account the effects that the wing has on the rotor loads. For these reasons, an unsteady simulation have been carried out for a given trim condition of the rotor ($\theta = 12°$, $\beta = 2.5°$, $\zeta = -9.8°$) to verify whether or not there are marked differences between the predicted aerodynamic loads. With the aim to compare the results, we decided to use the same computational grid both for steady and unsteady simulations and to change the meshes with respect to the ones employed in Section 2.3. This need belongs to the fact that the unsteady calculations are much more complex than steady simulations and the computational time required to reach a converged solution in time is much higher than in the steady case. Using the grids of Section 2.3 as the starting point for the new ones, we refined the new grids by increasing the mesh quality around the bodies and by limiting the spatial extension of each mesh. Due to this and in order to reduce the final mesh size and then the computational cost of each run, we slightly decreased the the number of cells of each grid. The final mesh for the steady simulations is then composed by 7 structured multi–block grids, for a total of 8.50×10^6 cells. As in the previous case, the background grid is composed by 2 different grids, one fine (the inner grid) and one coarse (the outer grid). The grids of the two wing portions and of the nacelle, contained inside the finest background grid, are C grid. The outer boundaries are located $0.2\ R$ away from the bodies except in the wake direction where the boundaries are located $1.4\ R$ from the trailing edge. A symmetry condition has been applied to the aircraft symmetry plane, whereas both wings and the nacelle have been modelled through no–slip boundary conditions.

We now turn to the discussion of the numerical results. We begin by inspecting the steady simulations that have been carried out by reproducing the effects of the rotor with an actuator disk. As already described in Section 2.3, a cylindrical O–H grid is used to represent the actuator disk. The disk without thickness, on which the desired force (per unit area) distribution is given [12], has been placed on the tip path plane of

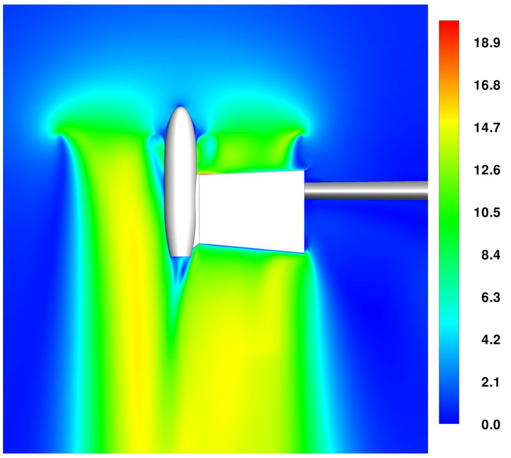

Figure 4.26: *Velocity magnitude distribution for the tilted wing configuration at* $C_T/\sigma = 0.049$*,* $h^w/R = 0.324$*,* $M_{Tip} = 0.32$*, steady simulation.*

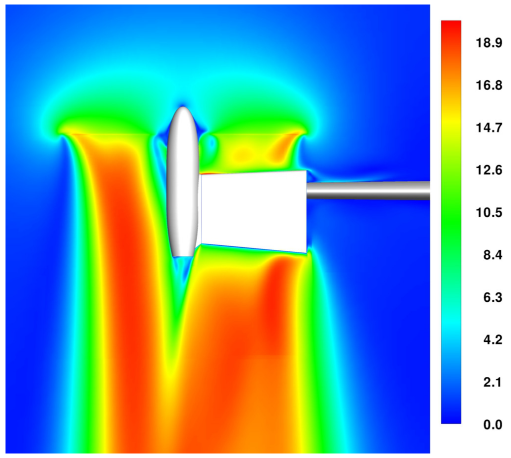

Figure 4.27: *Velocity magnitude distribution for the tilted wing configuration at* $C_T/\sigma = 0.102$*,* $h^w/R = 0.324$*,* $M_{Tip} = 0.32$*, steady simulation.*

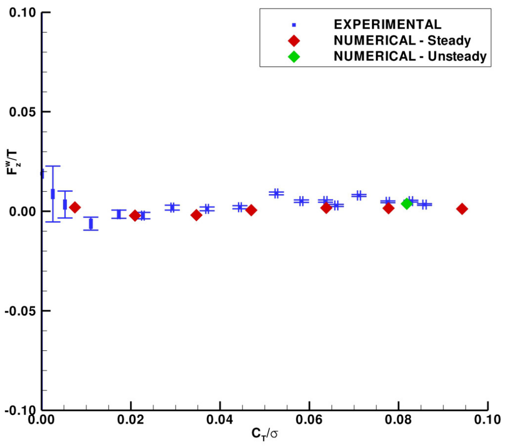

Figure 4.28: *Comparison between experimental data and steady CFD calculation for the half–model:* F_z^w/T *as function of* C_T/σ*,* $M_{Tip} = 0.32$.

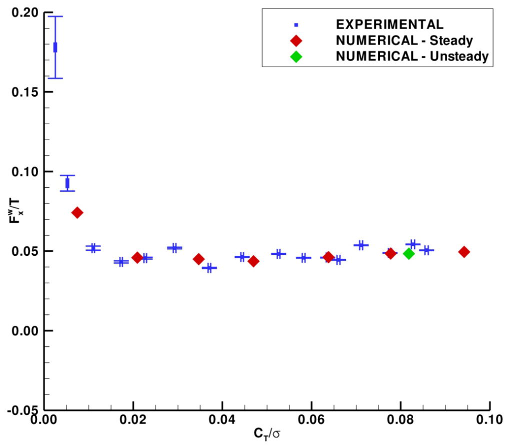

Figure 4.29: *Comparison between experimental data and steady CFD calculation for the half–model:* F_x^w/T *as function of* C_T/σ*,* $M_{Tip} = 0.32$.

the rotor. Since this plane is defined by the rotor trim condition, the spatial location of the disk changed for every $C_T\sigma$ analysed. The force distribution on the disk has been computed from knowledge of the load distributions on the blade (previously computed). Examples of flow fields in terms of velocity magnitude distribution in a vertical plane parallel to the thrust direction at two different C_T/σ are given in Figure 4.26 and 4.27. Figure 4.28 and 4.29 show the comparison between experimental and numerical results for the vertical and lateral loads acting on the wing as function of C_T/σ at the design wing–rotor distance h^w/R. In both figures the standard deviations of the vertical and longitudinal wing loads are plotted on the experimental curves (vertical bars) together with the standard deviation of the thrust coefficient. The evaluation of the standard deviation has been carried out by taking into account the accuracy of the instruments as well as the measurement repeatability. The latter source of uncertainty has been

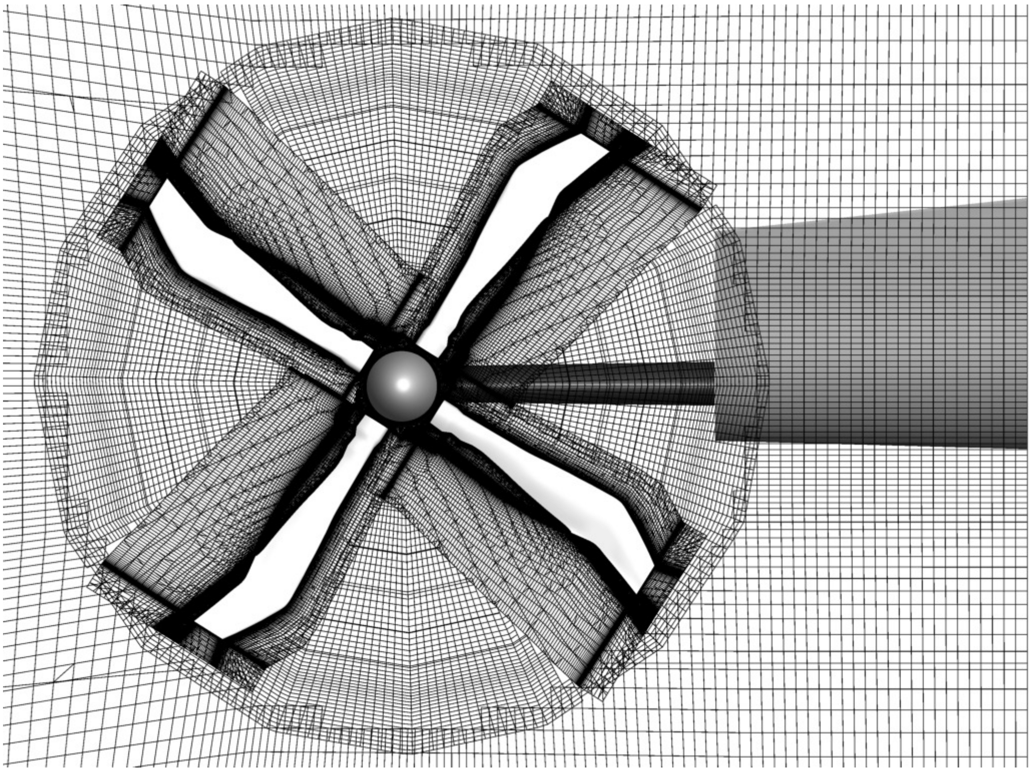

Figure 4.30: *Example of grids system for unsteady CFD calculations: top view of the half–model.*

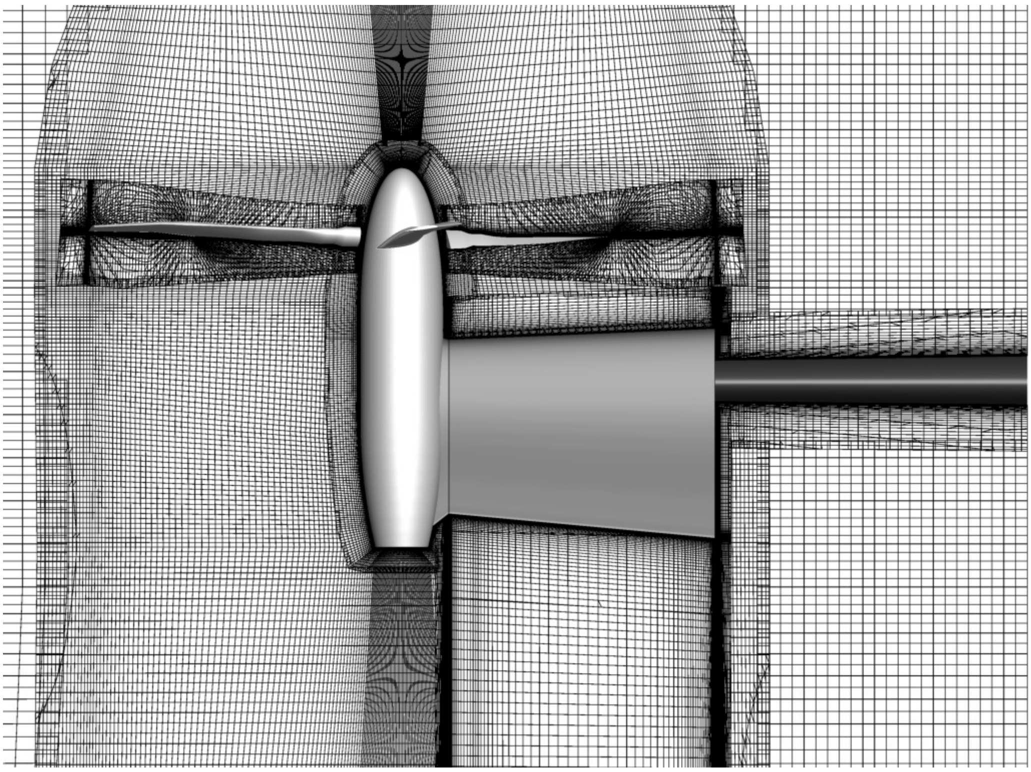

Figure 4.31: *Example of grids system for unsteady CFD calculations: lateral view of the half–model.*

evaluated over 40 measurement points acquired for $\theta = 12°$. The agreement between numerical calculations and experimental data is rather good in both cases demonstrating that the CFD code ROSITA is capable to predict the loads of the whole aircraft. However, for C_T/σ higher than 0.06, the values of the vertical force component F_z^w predicted by the CFD code are slightly lower with respect to the experimental data. An upload effect is still present but the predicted force/thrust ratio is less than 0.3 %.

The unsteady simulation has been performed on a final grid of a total of 15×10^6 cells. As previously mentioned, the computational mesh for the unsteady simulation has been obtained by replacing the actuator disk grid with four identical grids. Each grid was composed by 1.7×10^6 cells and contained one blade. Two different examples of the grid system for the unsteady calculation are shown in Figure 4.30 and 4.31. The simulation has been carried out on a total of 10 rotor revolutions [71]. Every time step the blades and their grids were rotated of $2°$. To start the unsteady simulation, an

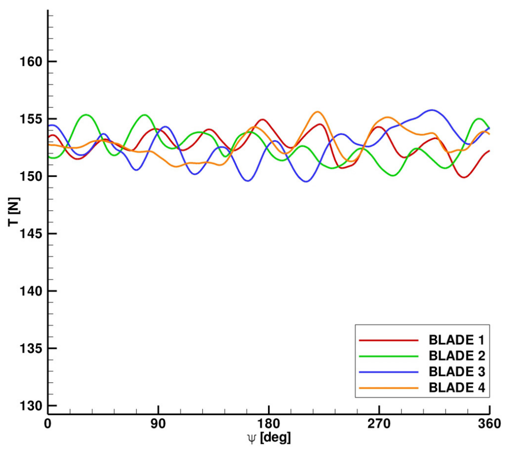

Figure 4.32: *Half–model: unsteady CFD calculations, blade T as function of ψ, $M_{Tip} = 0.32$.*

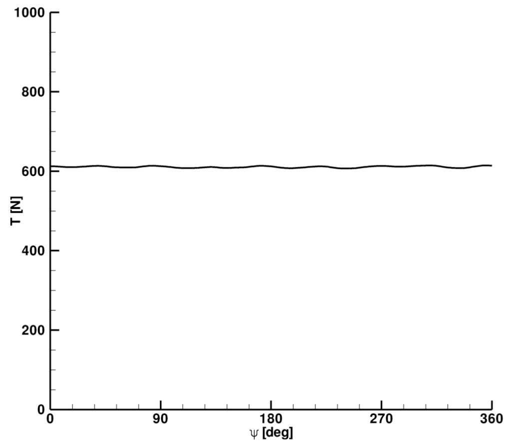

Figure 4.33: *Half–model: unsteady CFD calculations, rotor T as function of ψ, $M_{Tip} = 0.32$.*

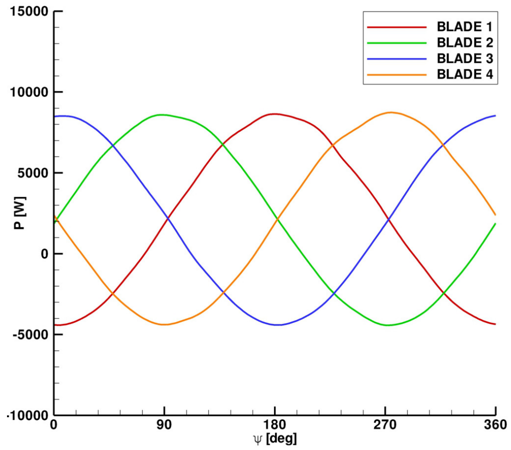

Figure 4.34: *Half–model: unsteady CFD calculations, blade P as function of ψ, $M_{Tip} = 0.32$.*

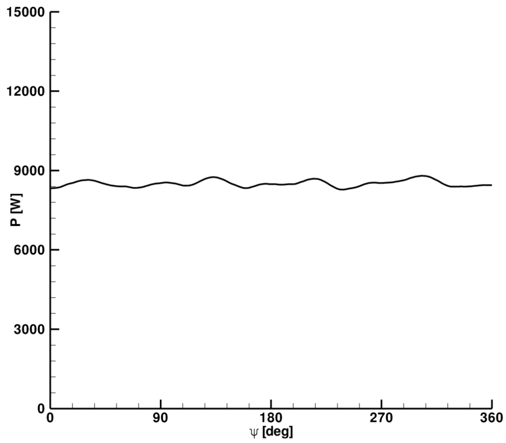

Figure 4.35: *Half–model: unsteady CFD calculations, rotor P as function of ψ, $M_{Tip} = 0.32$.*

impulsive start has been used at the first time step. The variation of the rotor forces became nearly periodic after the fourth revolution. However, since the free stream velocity is zero in hovering, the rotor wake system needed more than four revolutions to reach a fully developed state. After 6 rotor revolutions the wing was fully immersed in the rotor wake and also wing forces became nearly periodic. After 8 the rotor wake has been convected sufficiently far downstream from the wing system and both the rotor and the wing loads reached a converged state, demonstrating however a dependence on the blade azimuthal position. This is confirmed by looking at the temporal history of the forces induced by the rotor wake system on the rotor itself and on the wing surfaces. The time history of the rotor loads during the tenth revolution are shown in Figure 4.32, 4.33, 4.34 and 4.35 respectively for thrust and power and are expressed in terms of azimuthal blade angle ψ. In Figure 4.36 is reported the rotor FM while

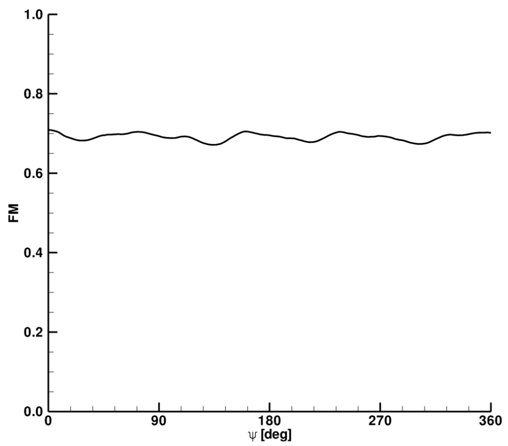

Figure 4.36: *Half–model: unsteady CFD calculations, FM as function of ψ, $M_{Tip} = 0.32$.*

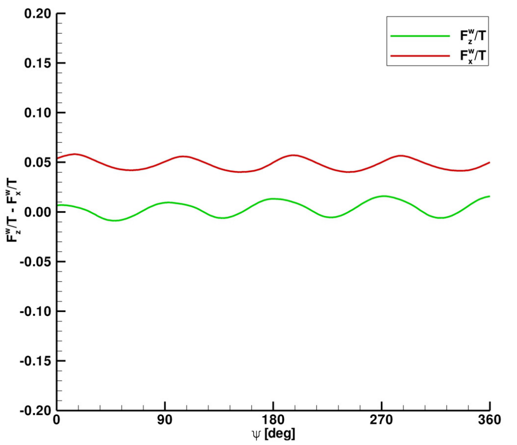

Figure 4.37: *Half–model: unsteady CFD calculations, F_x^w/T and F_z^w/T as function of ψ, $M_{Tip} = 0.32$.*

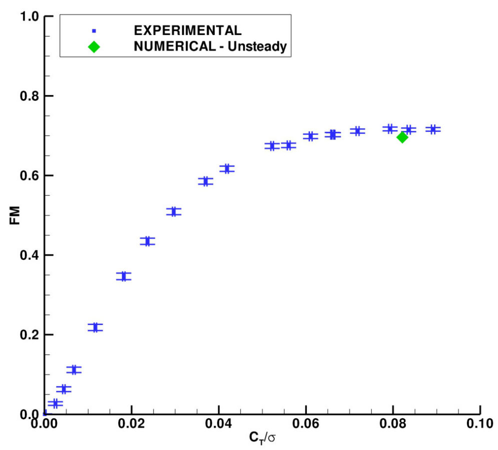

Figure 4.38: *Comparison between experimental data and unsteady CFD calculation for the half–model: C_P as function of C_T, $M_{Tip} = 0.32$.*

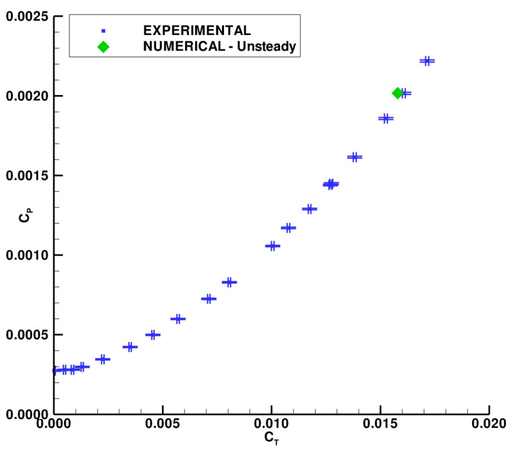

Figure 4.39: *Comparison between experimental data and unsteady CFD calculation for the half–model: C_P as function of C_T, $M_{Tip} = 0.32$.*

in Figure 4.37 is reported the time history of the wing vertical and longitudinal loads. It is interesting to observe how the predicted forces on the wing surfaces exhibited the characteristic frequency of 4 cycles per revolution, typical of a four-bladed rotor. The wing loads predicted by the unsteady calculation have been shown as function of C_T/σ in Figure 4.28 and 4.29 where they are also compared with experimental results and steady calculations. The values of F_x^w/T and F_z^w/T reported in these figures are the mean values calculated over the last rotor revolution. As shown in Figure 4.28 and

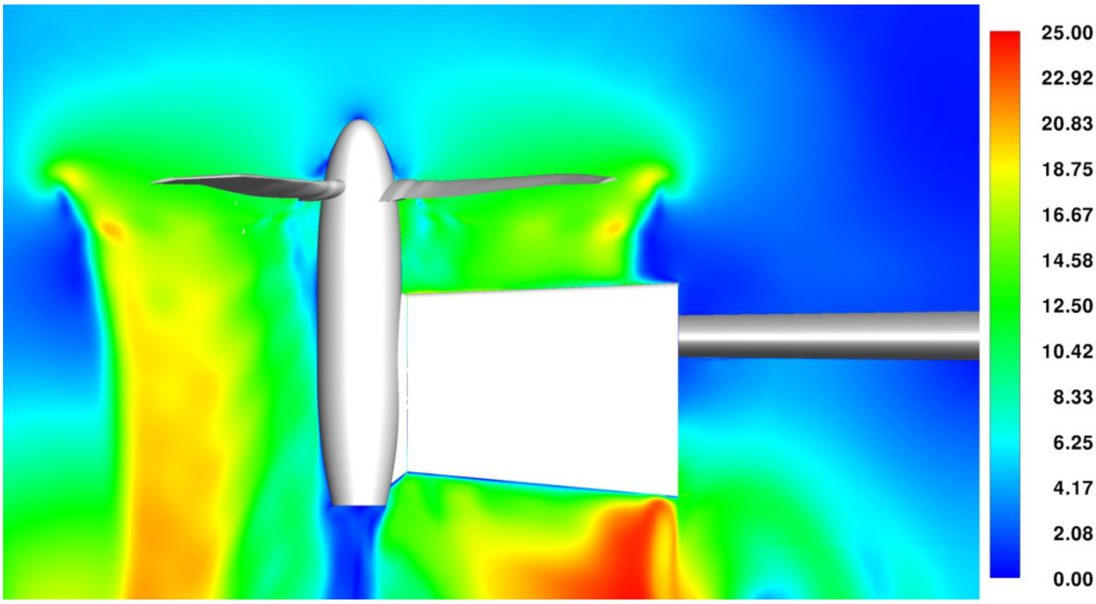

Figure 4.40: *Unsteady velocity magnitude contours for the tilted wing configuration at* $\psi = 45°$, $h^w/R = 0.324$, $M_{Tip} = 0.32$.

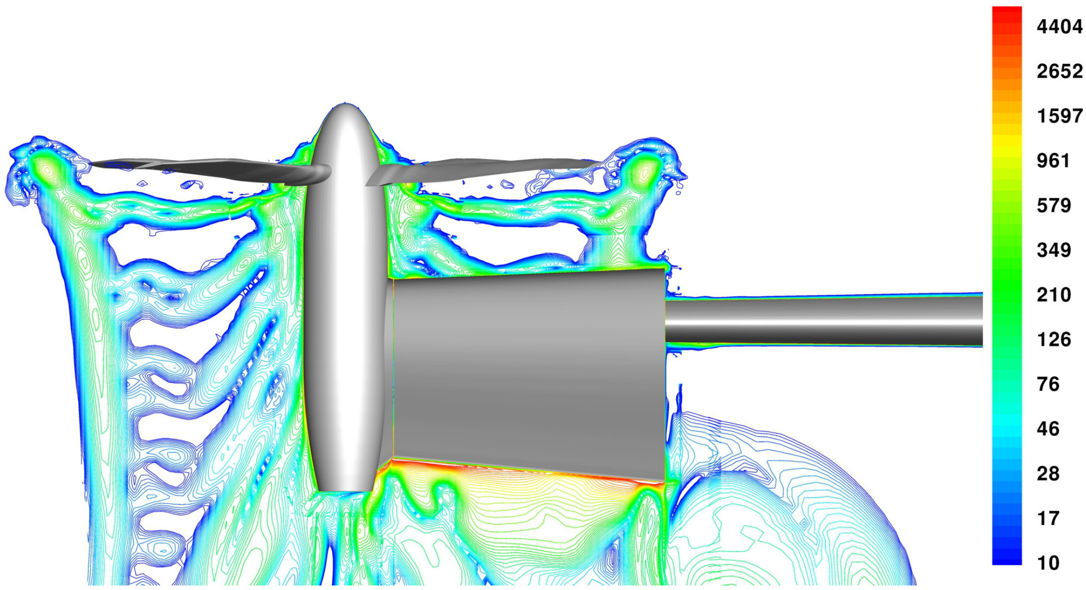

Figure 4.41: *Unsteady vorticity magnitude contours for the tilted wing configuration at* $\psi = 45°$, $h^w/R = 0.324$, $M_{Tip} = 0.32$.

4.29, wing loads are well predicted by the unsteady CFD simulation. In the first case, the agreement between the present result and the experimental data is rather good and slightly better than in the steady case. On the other hand, the longitudinal force value F_x^w/T is almost equal to the steady results. A rather good agreement has been found also for rotor loads. The rotor hover performance are shown in Figure 4.38 and 4.39, detailing the FM and power coefficient trends with thrust coefficient. In these cases, the discrepancies between numerical results and experimental data are mostly due to

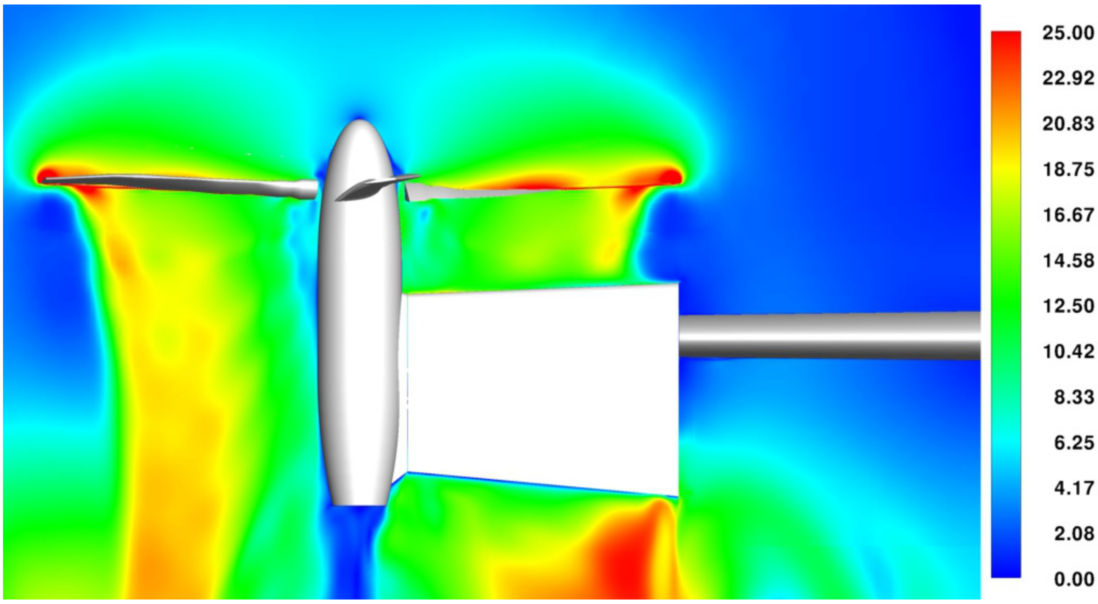

Figure 4.42: *Unsteady velocity magnitude contours for the tilted wing configuration at* $\psi = 90°$, $h^w/R = 0.324$, $M_{Tip} = 0.32$.

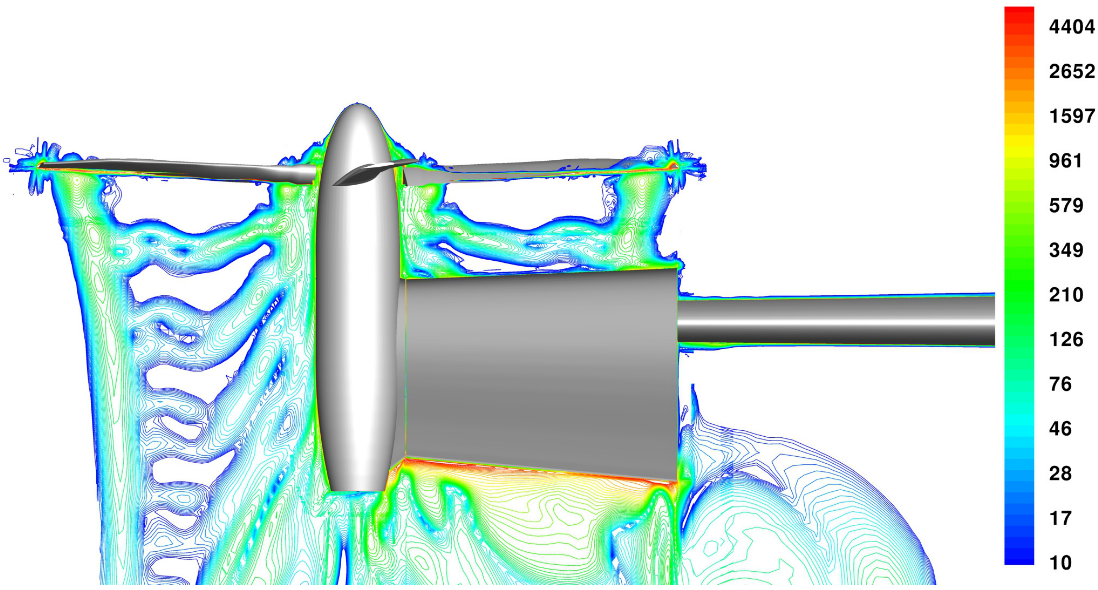

Figure 4.43: *Unsteady vorticity magnitude contours for the tilted wing configuration at* $\psi = 90°$, $h^w/R = 0.324$, $M_{Tip} = 0.32$.

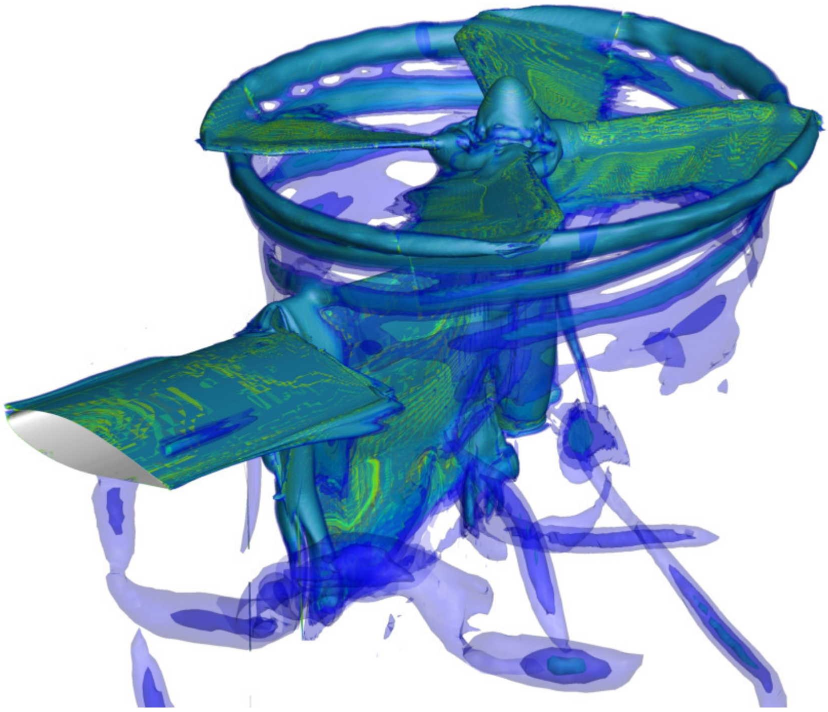

Figure 4.44: *Isosurfaces of the vorticity, giving a picture of the complex vortical structures shed by the rotor,* $\psi = 45°$, $h^w/R = 0.324$, $M_{Tip} = 0.32$.

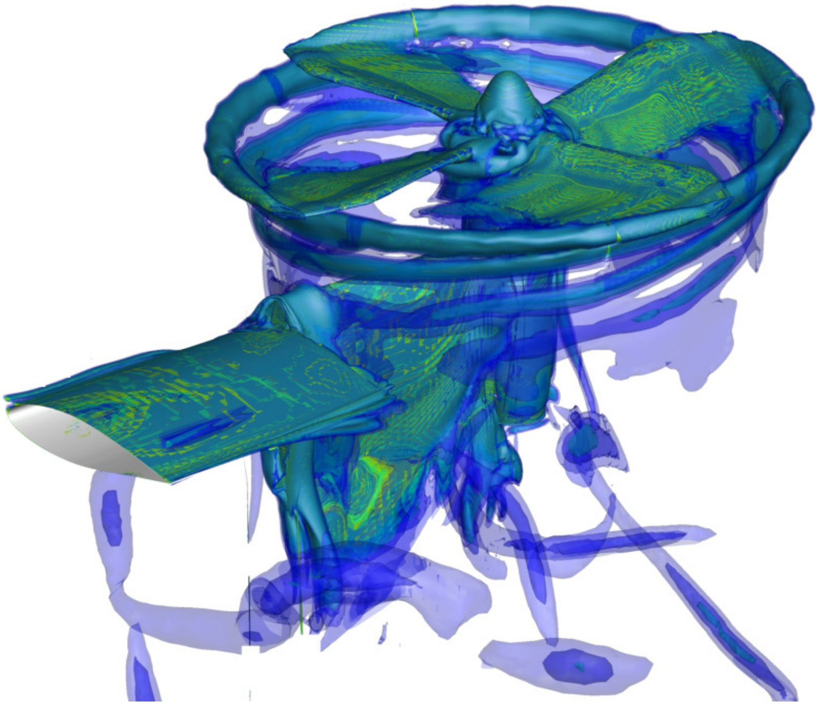

Figure 4.45: *Isosurfaces of the vorticity, giving a picture of the complex vortical structures shed by the rotor,* $\psi = 90°$, $h^w/R = 0.324$, $M_{Tip} = 0.32$.

the fact that the rotor loads are subjected to a more irregular variations with respect to wing loads possibly indicating a lack of spatial or temporal resolution. Even though the tilted wing is immersed in the rotor wake system, the load variations on the wing are more regular, as demonstrated by comparing Figure 4.37 with Figure 4.32. This may be justified by looking at Figure 4.40, 4.41, 4.42, and 4.43, where the velocity magnitude contours and the isolines of the vorticity vector modulus are plotted in correspondence of a slice of the flow field parallel to the rotor axis for two different blade phases ($\psi = 45°$ and $\psi = 90°$). These figures suggest that the tilted wing is subject to the forcing of rotor wake system that is almost periodic. Indeed, blade tip vortices are convected downstream from the rotor and strike on the leading edge of the tilted wing with a frequency of 4 cycles per revolution. On the other hand, the interaction which occur between a blade and a tip vortex of the preceding one seems to be higher in the region above the wing with respect to other azimuthal blade positions, as shown in Figure 4.41 and 4.43. This phenomenon can be observed also in Figure 4.44 and 4.45 where a three dimensional view of the isosurfaces of the vorticity is given for the same blade phases of the previous images.

CHAPTER 5

PIV measures in hover

Since in hover flight the interference between the rotor wake and the wing is very complex and totally unsteady, force measurements may give only partial information about the physics of the phenomena due to this kind of aerodynamic interaction. Therefore, in the present chapter we describe the analysis of the hover flight condition by means of Particle Image Velocimetry measurements. Both the isolated rotor and the tiltwing half–model were tested.

5.1 Introduction

As known, in hover the vortex structures generated at the blade tip follow helical trajectories below the rotor and are convected downstream in the rotor wake. Even though the wake structure is relatively complicated, at list in principle the wake of an isolated hovering rotor is radially axisymmetric [47]. However, when a given body is placed inside the wake under the rotor, as for instance an helicopter fuselage or a tiltrotor wing, the rotor wake geometry may change significantly. Moreover, the interaction between the rotor wake and the given body may produce negative effects on the aircraft, decreasing for example its performance. As already shown in Chapter 4, the main effect of the wing on a tiltrotor with conventional configuration is the drastic reduction of the aircraft FM which means an increase of the thrust required to hover for the rotor. In this frame, we also demonstrated the capability of a tiltwing aircraft to minimise the loss of aircraft performance in hover because of the reduced frontal section of the tilted wing portion which is immersed in the rotor wake. Apart form these global effects, the interaction between the rotor wake and the wing is responsible for the growth of unsteady phenomena that could have negative effects on the aircraft, as for example high load oscillations on the wing. Therefore, an correct characterisation of the rotor wake geometry together with extensive description of the flow field between the rotor plane and the wing can help the engineers during the design process of a tiltrotor aircraft. In this regards however, experimental and numerical databases on tiltwing aircraft are very few and not public. On the other hand, many experimental works have been done during last years on tiltrotors with conventional configuration. For example, Darabi et all. [16] gave descriptions of the mean and time–dependent rotor wake flow over a XV–15 tiltrotor model in hover using stereoscopic PIV while Grife et all. [32] proposed the use of active flow control to reduce hover download on a scaled V–22 model. Numerical works on tiltrotor with conventional configuration in hover is more limited. A numerical investigation of the flow impinging on the wing surface of the XV–15 has been given by Kjellgren et all. [3] while CFD simulation on the V–22 whole aircraft have been carried out by Meakin [60] and by Potsdam and Strawn [71].

Due to the lack of information on the rotor wake flow field over a tiltwing model in hover, the purpose of the PIV measurements presented in the following of this chapter is to give a detailed and useful description of the flow field around a tiltwing aircraft in order to understand the mechanism through which the blade tip vortex strikes in such a way on the surface of the wing.

5.2 PIV setup

The PIV setup of the DSTA Aerodynamics Laboratory has been used to investigate the flow field below the rotor and the effects of the wing on the rotor wake (for a description of the PIV setup see Section 3.4.2). To describe how the wing modifies the rotor wake geometry, we took into account both the isolated rotor and the tiltwing half–model in the tiled configuration. PIV surveys were made in rectangular domains located in several vertical planes. In particular, azimuthal planes containing the rotor axis and perpendicular to the rotor disk have been used to measure the velocity flow field below the rotor without and with the wing. In both cases the PIV measurement area was $0.45\ R$ wide and $0.90\ R$ high and was composed by four measurement windows ($0.42 \times 0.22\ m$) with a small overlapping region between them. The outer edge of the measurement area was placed in correspondence of the tilt wing section while the upper edge was located $0.15\ R$ over the rotor centre. Radial planes, containing the wing chord, have been employed only for the tiltwing model to evaluate the tangential (or swirl) velocity component in the rotor wake flow over the leading edge of the tilted wing. In this case, the PIV measurement area was $0.27\ R$ wide and $0.35\ R$ high and was composed by three ($0.25 \times 0.12\ m$) measurement windows. When the azimuthal planes were acquired, the Dantec laser was located in a vertical position under the rotor and was mounted on a single axis traversing system fixed on the aluminium basement, as shown in Figure 5.1. The same setup was also used for the tiltwing half–model when a vertical plane parallel to the tilted wing chord and located in front of the lower surface of the wing is considered. In this condition, the laser has been moved together with the camera of $0.073\ m$ in the negative direction along the x–axis (see the test rig reference system, Figure 3.3). Indeed, the setup relocation was due to the presence of the wing that prevented the possibility to light the flow field area above the leading edge of the tilted wing. However, the displacement of the laser was so small that the windows with and without the wing are still comparable. When radial planes were studied, the PIV

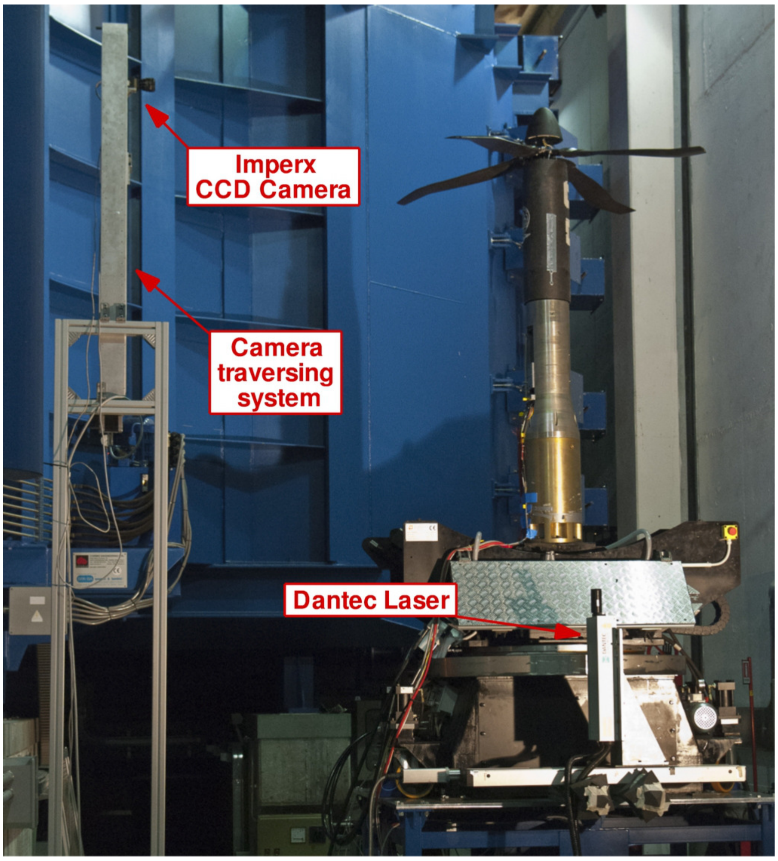

Figure 5.1: *View of the PIV setup for the isolated rotor system.*

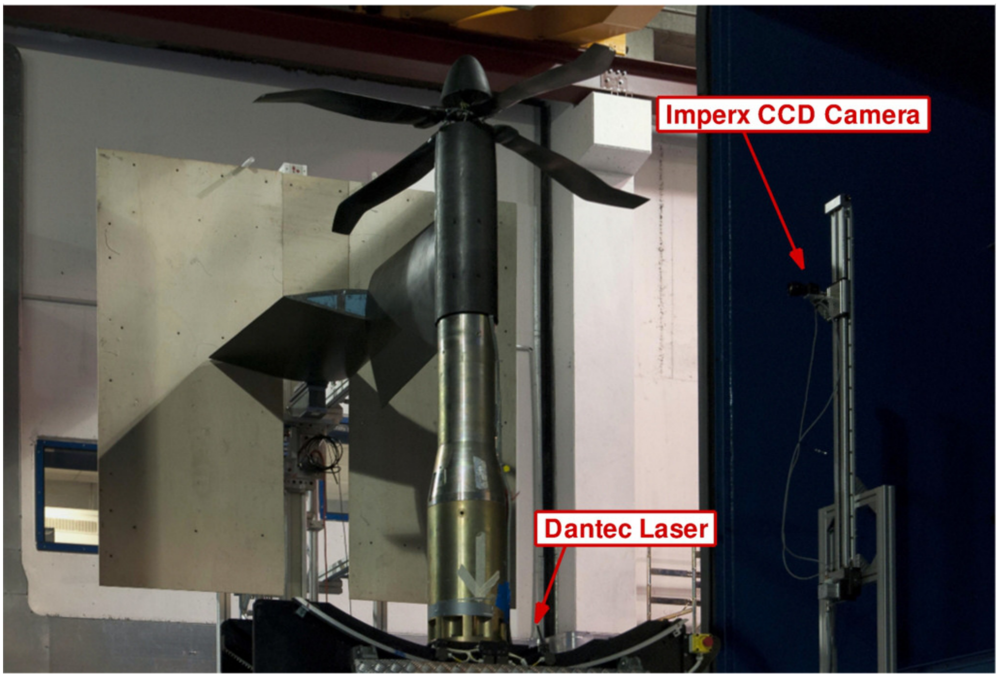

Figure 5.2: *View of the PIV setup for the half–model system.*

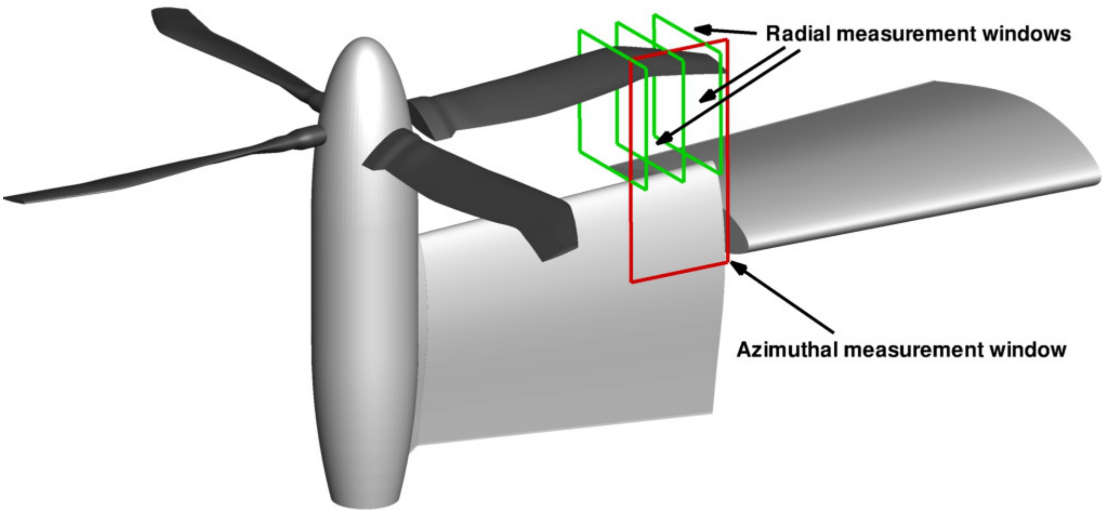

Figure 5.3: *Schematic view of the PIV planes for the half–model system.*

setup was rearranged in such a way to properly light the measurement planes. In particular, the laser was placed on the wind tunnel floor and the laser sheet was aligned with the tilted wing chord. Three different planes at different radial locations from the rotor axis have been analysed by moving the laser in the wing span direction. The camera, mounted on a single axis traversing system fixed on the wing support, was located over the fixed wing upper surface and below the image plane. An example of the PIV setup for the half–model is shown in Figure 5.2. A schematic view of the PIV azimuthal and radial planes for the half–model system is reported in Figure 5.3. PIV measurements were acquired for every configuration tested and phase-locked data was taken by synchronising the laser pulses with a prescribed azimuthal position of a selected rotor blade. Six different phase–locked data sets were taken in the $90°$ interval between adjacent rotor blades and for each run the velocity flow field was phase averaged over 100 image pairs. All the PIV results are presented in a cylindrical coordinate system originating at the rotor hub, with the coordinate z that is normal to the rotor disk, coincident with its axis and pointing upwards, the radial coordinate r that goes along the span of the blades and the tangential coordinate ψ that is positive counterclockwise. All the PIV measurements have been carried out on the same test condition in which the tip Mach number was $M_{Tip} = 0.32$ and the collective blade pitch was $\theta = 12°$.

5.3 Isolated rotor wake

PIV measurements on the isolated rotor system have been acquired in a vertical plane for six different prescribed azimuthal phase of the selected reference blade. In the following, PIV results are reported in terms of velocity magnitude and vorticity contours. In Figure 5.4, 5.6, 5.8, 5.10, 5.12, 5.14, the phase-locked velocity magnitude contours in the wake flow below the isolated rotor are reported for each blade phase considered. These figures show the evolution of the flow field in the rotor slipstream for further blade phases. In particular, the radial position of the tip vortices contracts progressively. The maximum contraction of the isolated rotor wake is reached at an axial

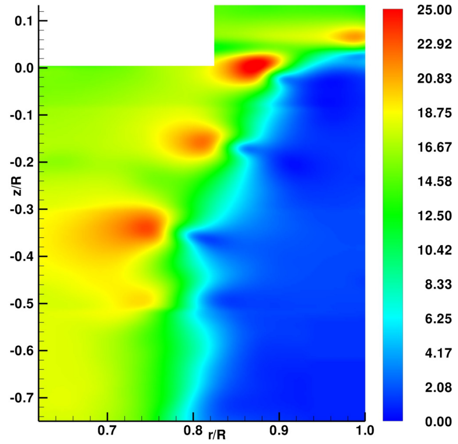

Figure 5.4: *Isolated rotor: phase-locked velocity magnitude contours,* $\psi = 15°$.

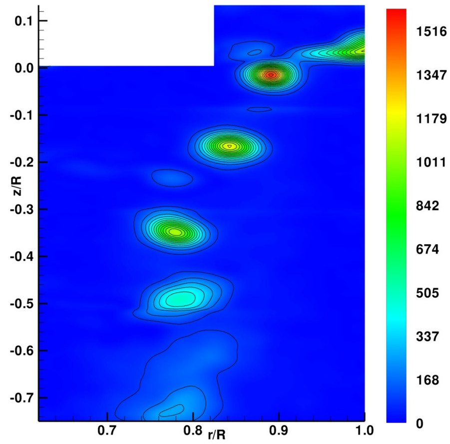

Figure 5.5: *Isolated rotor: phase-locked vorticity contours,* $\psi = 15°$.

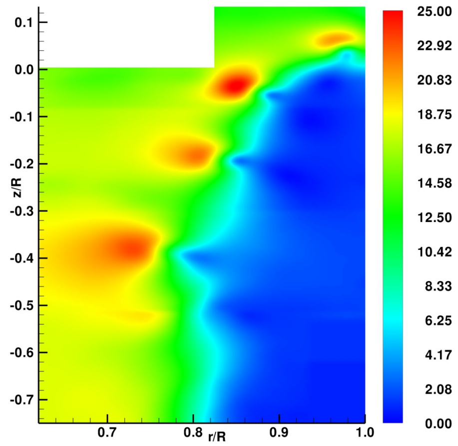

Figure 5.6: *Isolated rotor: phase-locked velocity magnitude contours,* $\psi = 30°$.

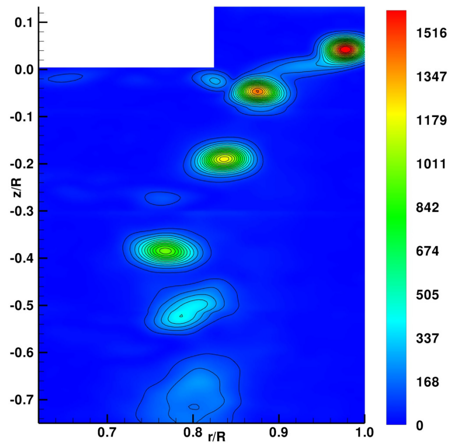

Figure 5.7: *Isolated rotor: phase-locked vorticity contours,* $\psi = 30°$.

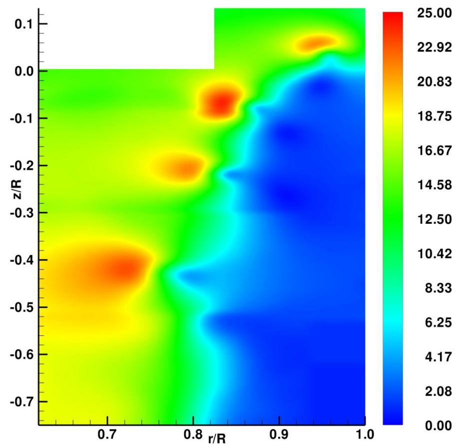

Figure 5.8: *Isolated rotor: phase-locked velocity magnitude contours,* $\psi = 45°$.

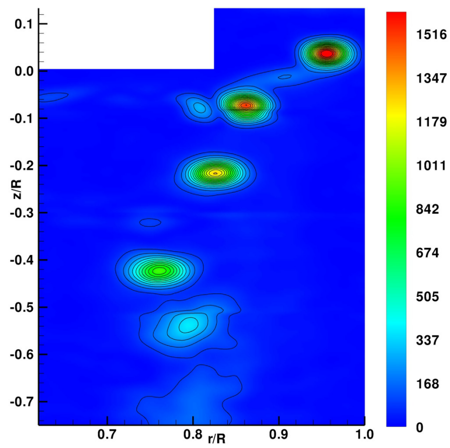

Figure 5.9: *Isolated rotor: phase-locked vorticity contours,* $\psi = 45°$.

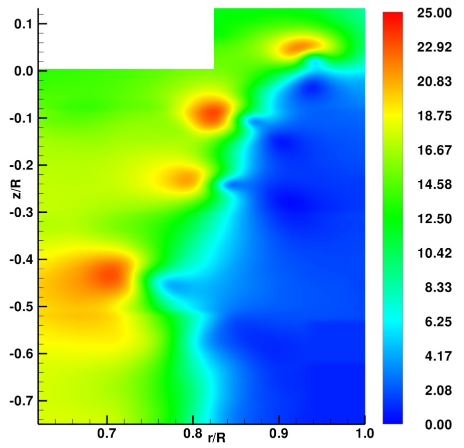

Figure 5.10: *Isolated rotor: phase-locked velocity magnitude contours, $\psi = 60°$.*

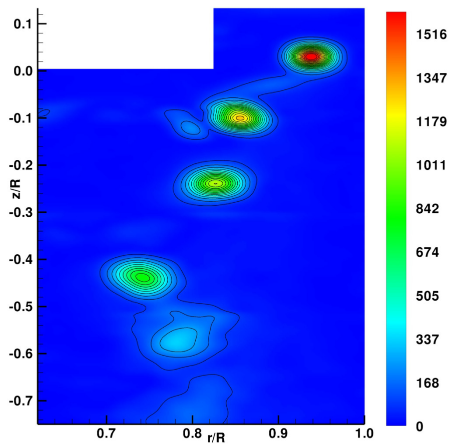

Figure 5.11: *Isolated rotor: phase-locked vorticity contours, $\psi = 60°$.*

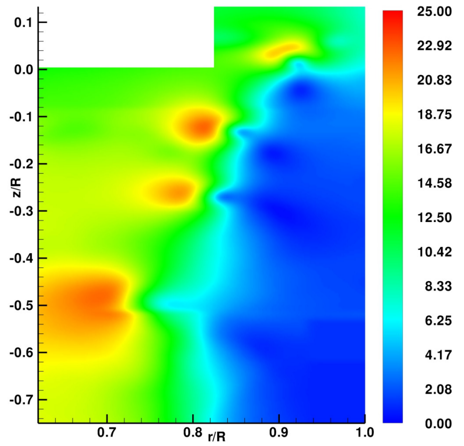

Figure 5.12: *Isolated rotor: phase-locked velocity magnitude contours, $\psi = 75°$.*

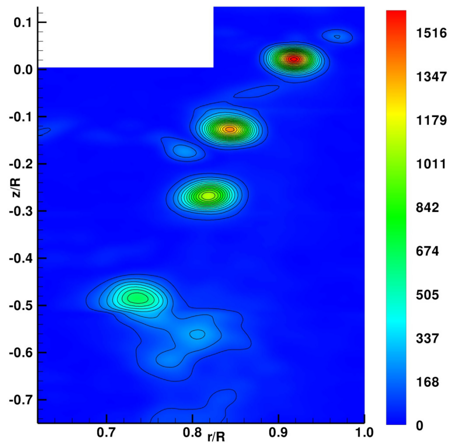

Figure 5.13: *Isolated rotor: phase-locked vorticity contours, $\psi = 75°$.*

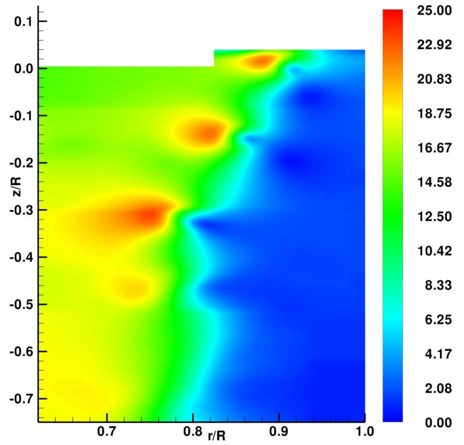

Figure 5.14: *Isolated rotor: phase-locked velocity magnitude contours, $\psi = 90°$.*

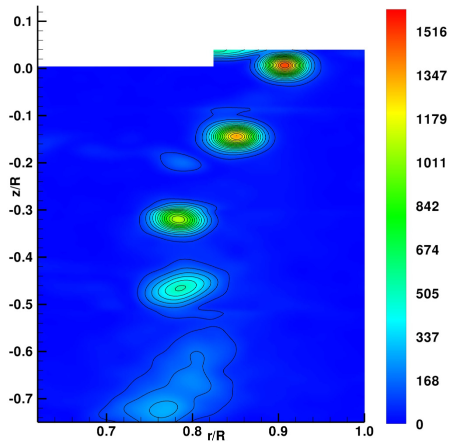

Figure 5.15: *Isolated rotor: phase-locked vorticity contours, $\psi = 90°$.*

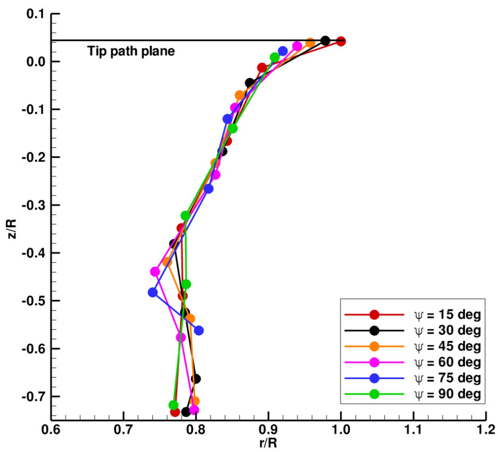

Figure 5.16: *Tip vortex displacements in a r/R–z/R plane: isolated rotor wake boundaries at different blade phases.*

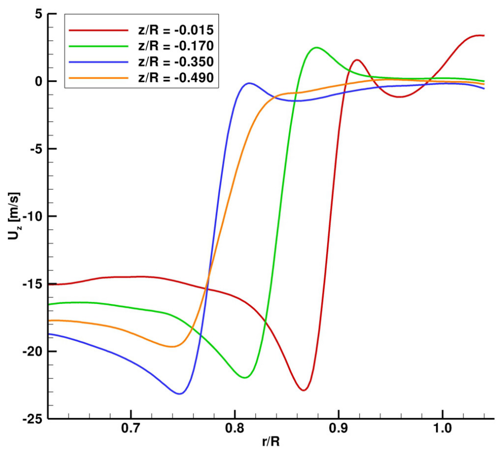

Figure 5.17: *Isolated rotor: profiles of the axial velocity component U_z at several distances from the rotor disk, $\psi = 15°$.*

distance of about $z/R = 0.4$ from the rotor disk where it approaches its asymptotic value. This value can be quantitatively estimated looking at the phase–locked vorticity contours in the same measurement planes, as shown in Figure 5.5, 5.7, 5.9, 5.11, 5.13, 5.15. The vorticity highlights the rotor wake boundary thus, referring to the spatial location of the vortex cores in the flow field, that are the regions where peaks of vorticity are present, the maximum wake contraction can be evaluated. However, small changes in the wake boundary can be observed from the comparison of the vorticity contours at different blade phases. This observed trend for the isolated hovering rotor demonstrated the presence of a little instability in the wake of the isolated rotor which can be related to the tip vortex instability and depends on the blade phase, as shown by Bhagwat and Leishman [8]. The evolution of the isolated rotor wake boundary can be better analysed in the z/R–r/R plane by plotting together the tip vortex displacements at different blade phases, as shown in Figure 5.16. Only when the azimuthal position of the blade is $\psi = 60°$ and $\psi = 75°$ a small variation in the radial location of the tip vortex become visible (respectively at $z/R = 0.45$ and 0.55). In general, after an axial distance of about $z/R = 0.4$ from the rotor disk, the radial displacement of the tip vortex is rather constant. From that point, the maximum contraction of the rotor wake assumes a constant value of $0.78\ R$.

The radial distribution of the axial velocity component U_z at several locations below the rotor has been reported in Figure 5.17 for an azimuthal blade phase of $\psi = 15°$. The figure show that in the inner part of the rotor wake the axial velocity accelerates from a minimum value of $15\ m/s$ in the proximity of the rotor disk to a maximum of $19\ m/s$ at $z/R = 0.35$. Moreover, the velocity gradient across the wake boundary tends to decrease at high axial distance ($z/R = 0.49$) because the tip vortices generated by the previous blades are convected downstream losing progressively their intensity.

5.4 Half–model with tiled wing

Figures from 5.18 to 5.29 show the velocity magnitude and vorticity contours in the wake flow below the rotor in the tiltwing half–model in the design configuration

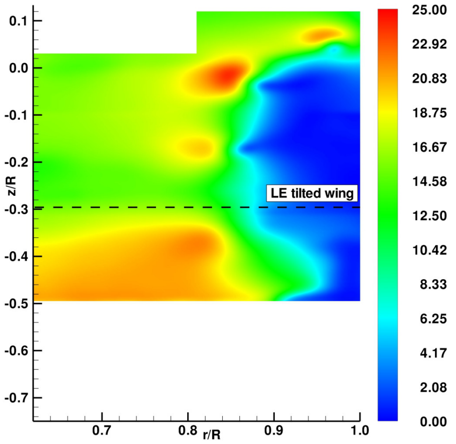

Figure 5.18: *Model: phase-locked velocity magnitude contours, $\psi = 15°$, $h^w/R = 0.324$.*

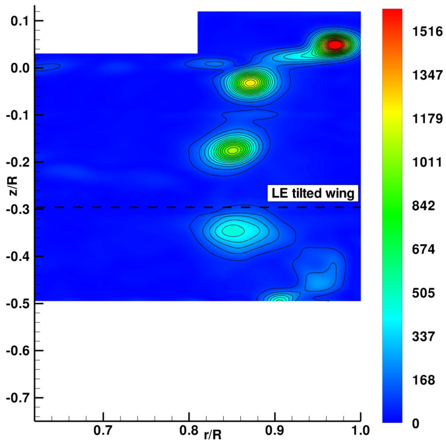

Figure 5.19: *Model: phase-locked vorticity contours, $\psi = 15°$, $h^w/R = 0.324$.*

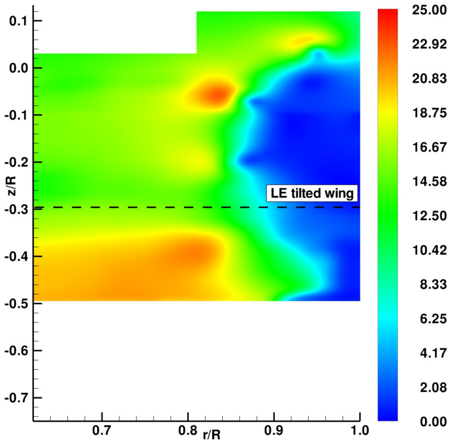

Figure 5.20: *Model: phase-locked velocity magnitude contours, $\psi = 30°$, $h^w/R = 0.324$.*

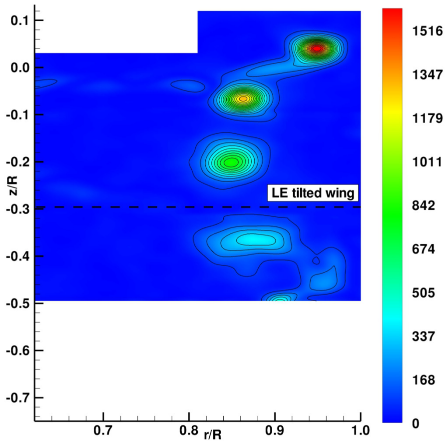

Figure 5.21: *Model: phase-locked vorticity contours, $\psi = 30°$, $h^w/R = 0.324$.*

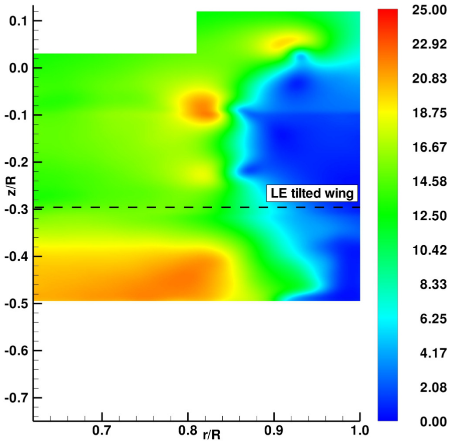

Figure 5.22: *Model: phase-locked velocity magnitude contours, $\psi = 45°$, $h^w/R = 0.324$.*

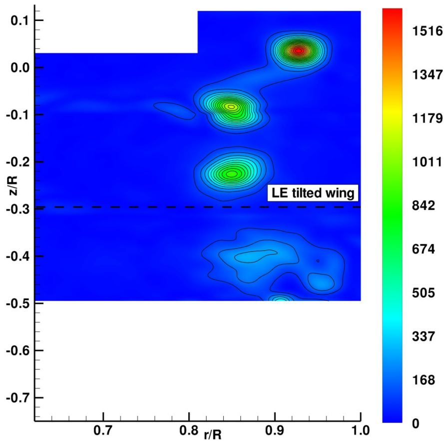

Figure 5.23: *Model: phase-locked vorticity contours, $\psi = 45°$, $h^w/R = 0.324$.*

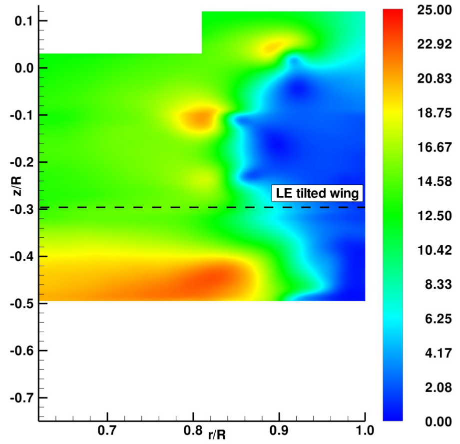

Figure 5.24: *Model: phase-locked velocity magnitude contours, $\psi = 60°$, $h^w/R = 0.324$.*

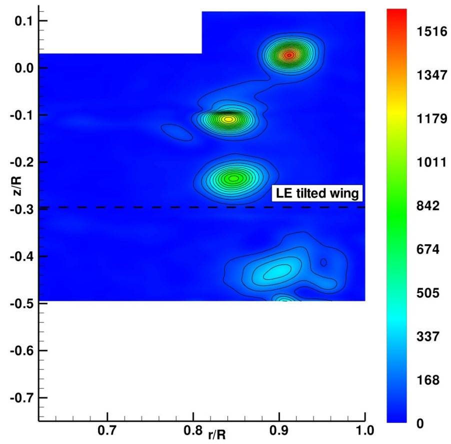

Figure 5.25: *Model: phase-locked vorticity contours, $\psi = 60°$, $h^w/R = 0.324$.*

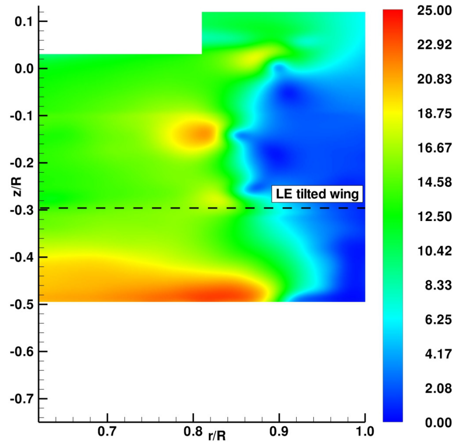

Figure 5.26: *Model: phase-locked velocity magnitude contours, $\psi = 75°$, $h^w/R = 0.324$.*

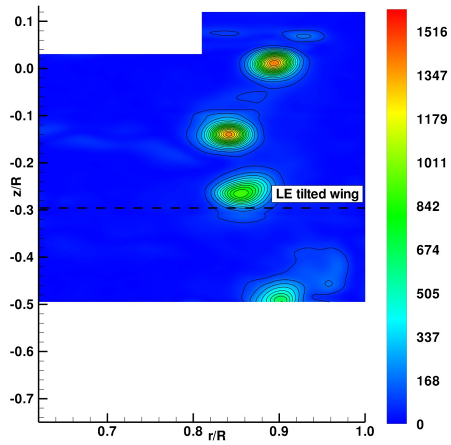

Figure 5.27: *Model: phase-locked vorticity contours, $\psi = 75°$, $h^w/R = 0.324$.*

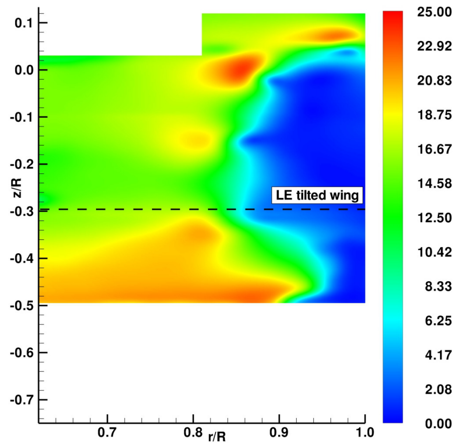

Figure 5.28: *Model: phase-locked velocity magnitude contours, $\psi = 90°$, $h^w/R = 0.324$.*

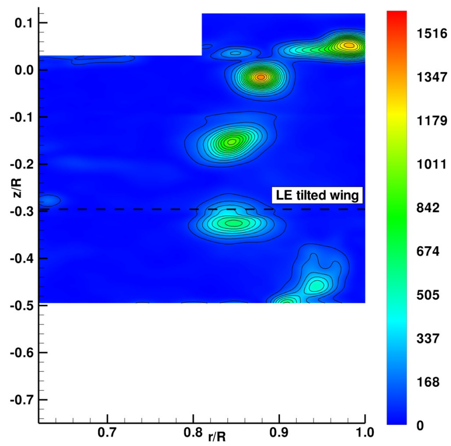

Figure 5.29: *Model: phase-locked vorticity contours, $\psi = 90°$, $h^w/R = 0.324$.*

$h^w/R = 0.324$. Since we are interesting on the description of the flow field around the tilted wing configuration, only the tilted wing condition at $\theta^{Tilt} = 90°$ has been taken into account in this part of the activity. In all the figures reported, the position of the leading edge of the tilted wing is shown. Looking at the vorticity contours reported in Figures 5.19, 5.21, 5.23, 5.25, 5.27 5.29, the evolution of the flow field in the rotor slipstream can be analysed. The maximum contraction of the rotor wake flow that impinges on the wing is reached at an axial distance from the rotor of $z/R = 0.14$. Following the same procedure adopted in the isolated rotor case, by referring to the spatial location of the vortex cores in the flow field, the maximum wake contraction approaches to a radial value of $0.85\ R$. The tip vortex displacements of the rotor wake in the half–model configuration has been reported in Figure 5.60 together with the tip vortex displacements of the isolated rotor wake. In this case it is apparent that when the rotor wake is approaching on the tilted wing, the presence of the wing in the flow field prevents the natural wake contraction. However, this effect is clear only when the tip vortices go below the axial distance from the rotor of $z/R = 0.11$. Moreover, once the rotor wake has reached the leading edge of the tilted wing, the tip vortex impinging on it is broken and convected downstream over the lower surface on the wing. An increase in the axial velocity is observed in the region immediately below the leading edge of the wing ($z/R = 0.35$) as shonw in Figure 5.43. Here, the radial distribution of the axial velocity U_z in the rotor wake has been reported in this test condition at several distance from the rotor disk for an azimuthal blade phase of $\psi = 15°$.

The numerical results of the unsteady simulation described in Section 4.3.3 are reported in the following both in terms of velocity magnitude and vorticity contours on the same plane of the PIV measurements on the tiltrotor half–model. In particular, Figures from 5.30 to 5.40 shown the velocity magnitude contours for several blade phases while in Figures from 5.31 to 5.41 the vorticity contours have been reported in the same conditions. Comparing the numerical results with the experimental measurements, a rather good agreement can be found between them. In particular, even if the vorticity field predicted by the CFD code is slightly less intense, the tip vortex displacements in the rotor wake flow are very similar. Moreover, the velocity distribution on the measurement area are quite the same.

As described in Section 2.3, the span–wise location of the tilt wing section has been defined trying to minimising the vertical load that raises on the wing in hover and vertical climb in helicopter mode flight. As consequence, in order to satisfy the requirements, the rotated part of the wing should be immersed in the rotor wake flow when the aircraft works in the tilted configuration. In this operating condition, the upload effect which develops on the wing (see Figure 4.20) could be explained by the fact that the flow field below the rotor is characterised by a non negligible swirl component. Due to this and thanks to the rotor sense of rotation (counterclockwise), the wing sections experience a positive angle of attack with respect to the flow impinging on it. Thereby, the vertical component F_z^w of the aerodynamic force which raises on the wing is pointed upward with respect to the aircraft reference system of Figure 3.3. To evaluate the tangential velocity component U_θ in the rotor wake over the leading edge of the tilted wing, PIV measurements have been carried out in three different radial planes near the wake rim ($r/R = 0.69$, 0.79 and 0.89) at the design wing–rotor distance $h^w/R = 0.324$. Figure 5.44 and 5.45 show the streamlines and the mean flow

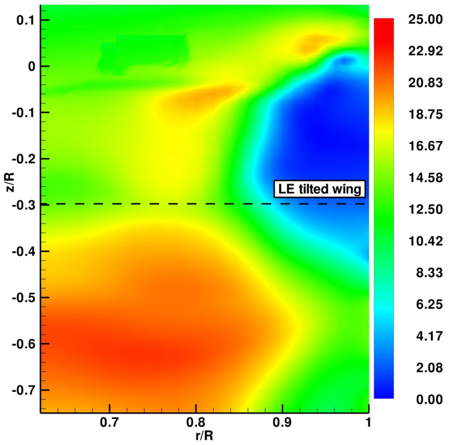

Figure 5.30: *CFD: phase-locked velocity magnitude contours, $\psi = 15°$, $h^w/R = 0.324$.*

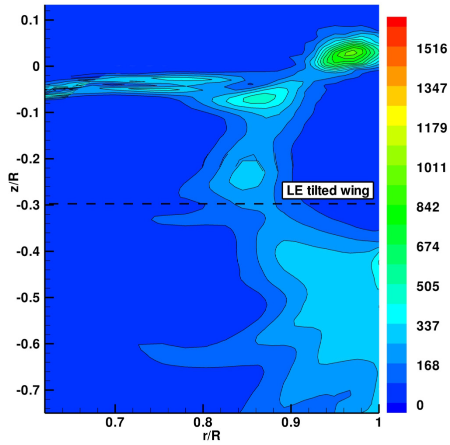

Figure 5.31: *CFD: phase-locked vorticity contours, $\psi = 15°$, $h^w/R = 0.324$.*

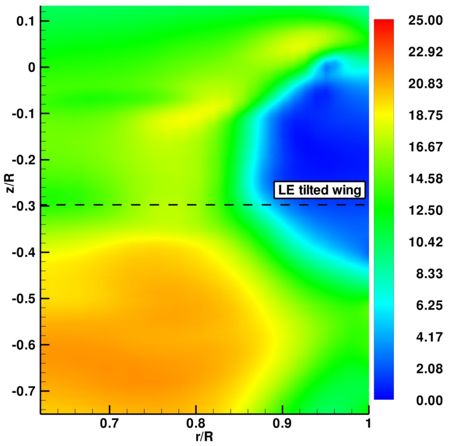

Figure 5.32: *CFD: phase-locked velocity magnitude contours, $\psi = 30°$, $h^w/R = 0.324$.*

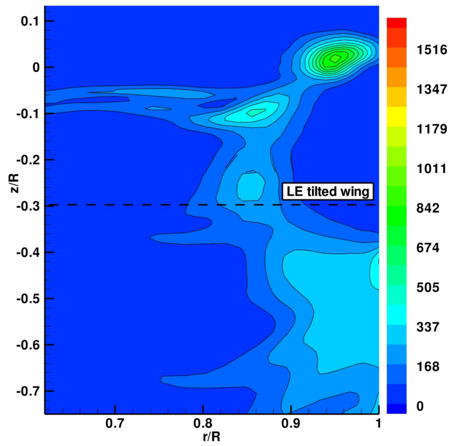

Figure 5.33: *CFD: phase-locked vorticity contours, $\psi = 30°$, $h^w/R = 0.324$.*

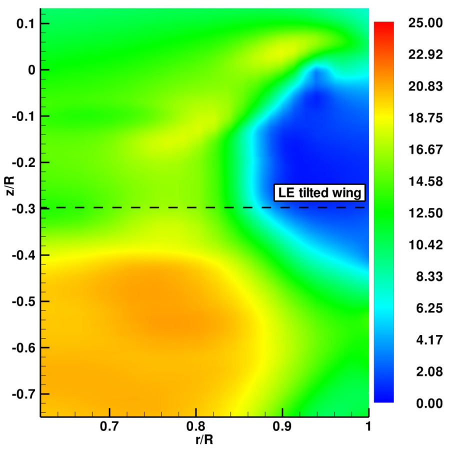

Figure 5.34: *CFD: phase-locked velocity magnitude contours, $\psi = 45°$, $h^w/R = 0.324$.*

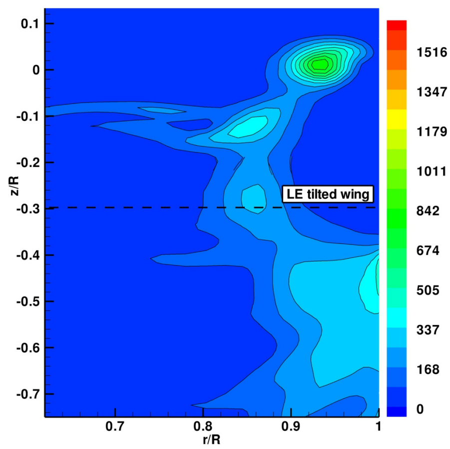

Figure 5.35: *CFD: phase-locked vorticity contours, $\psi = 45°$, $h^w/R = 0.324$.*

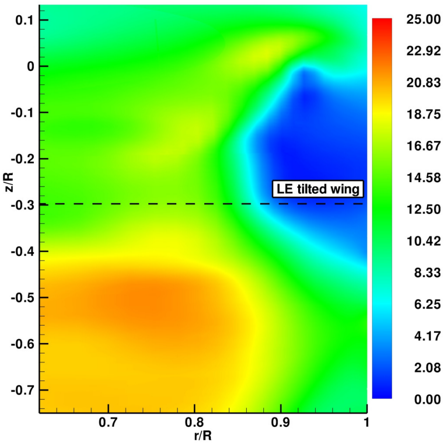

Figure 5.36: *CFD: phase-locked velocity magnitude contours, $\psi = 60°$, $h^w/R = 0.324$.*

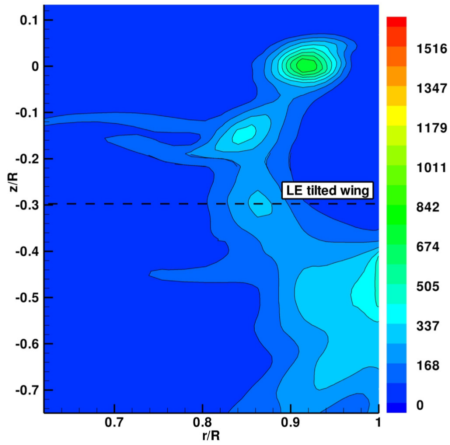

Figure 5.37: *CFD: phase-locked vorticity contours, $\psi = 60°$, $h^w/R = 0.324$.*

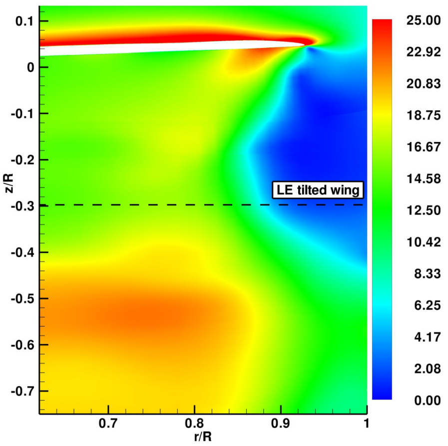

Figure 5.38: *CFD: phase-locked velocity magnitude contours, $\psi = 75°$, $h^w/R = 0.324$.*

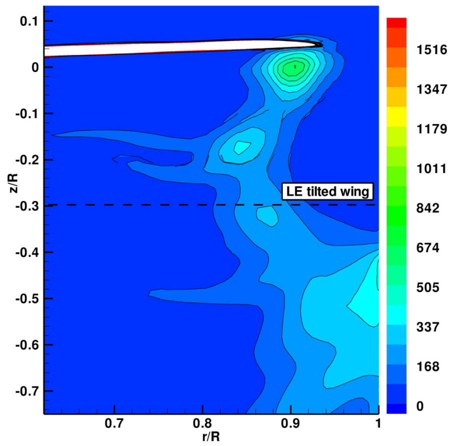

Figure 5.39: *CFD: phase-locked vorticity contours, $\psi = 75°$, $h^w/R = 0.324$.*

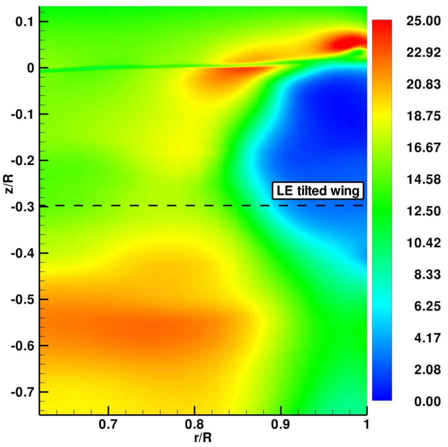

Figure 5.40: *CFD: phase-locked velocity magnitude contours, $\psi = 90°$, $h^w/R = 0.324$.*

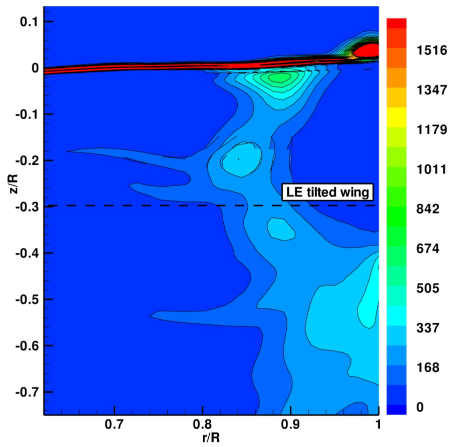

Figure 5.41: *CFD: phase-locked vorticity contours, $\psi = 90°$, $h^w/R = 0.324$.*

field that have been obtained by averaging acquired images for several blade phases. The streamlines within the rotor wake demonstrate that the flow strikes on the leading edge of the wing with a positive angle of attack with respect to the wing. Moreover, to quantify the magnitude of the swirl component in the wake, axial profiles of the tangential velocity component U_θ have been extracted in correspondence to the leading edge of the wing from the mean velocity fields acquired on the radial planes. As shown in Figure 5.46, the mean tangential velocity profile is rather constant in the inner measurement plane ($r/R = 0.69$) assuming a value of about $3\ m/s$. In the intermediate plane ($r/R = 0.79$), the mean tangential velocity profile varies from a minimum value of $1\ m/s$ just above the rotor to a maximum value of $3\ m/s$ at $z/R = -0.23$. In the outer plane the mean tangential velocity is close to zero near the wing and the same behaviour has been observed for the corresponding mean axial velocity component profile U_z, as shown in Figure 5.47. In the intermediate plane the mean axial velocity component reaches the maximum value of $19\ m/s$ while in the inner plane its maximum value

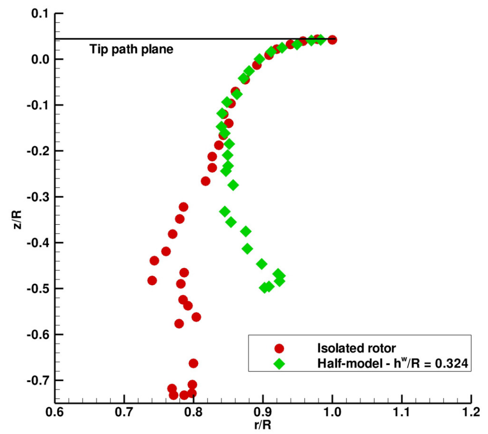

Figure 5.42: *Tip vortex displacements in a r/R–z/R plane: comparison between the isolated rotor and the half–model at $h^w/R = 0.324$.*

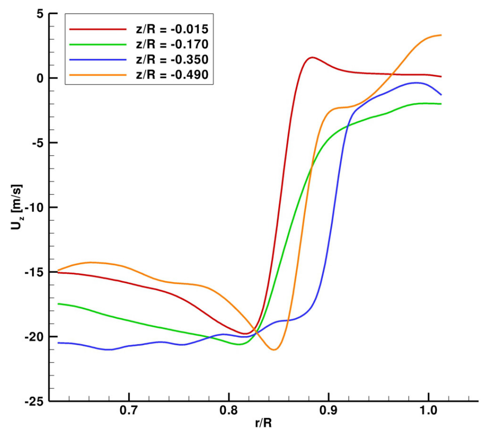

Figure 5.43: *Model: profiles of the axial velocity component U_z at several distances from the rotor disk, $\psi = 15°$.*

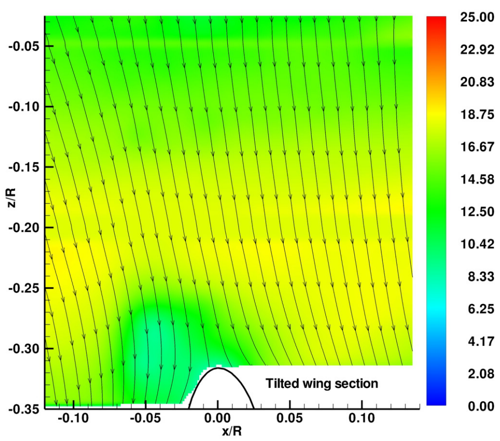

Figure 5.44: *Model: streamlines and the mean velocity magnitude contours, $r/R = 0.79$.*

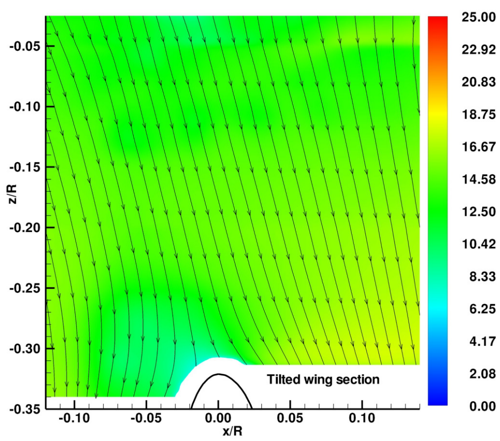

Figure 5.45: *Model: streamlines and the mean velocity magnitude contours, $r/R = 0.69$.*

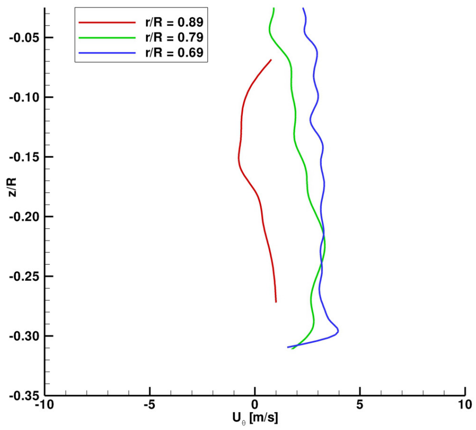

Figure 5.46: *Model: mean tangential velocity U_θ at three different radial positions.*

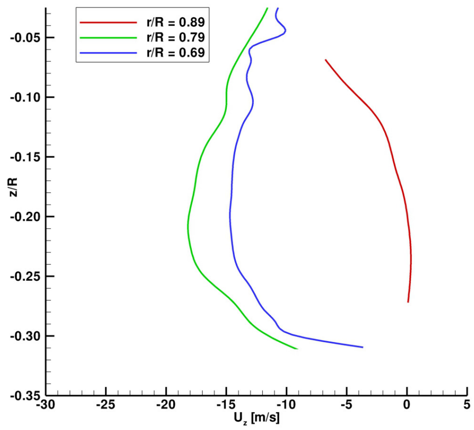

Figure 5.47: *Model: mean axial velocity U_z at three different radial positions.*

is 15 m/s. Taking into account the value of axial and tangential velocity components on these measurement planes, the estimated induced angle of attack of the wing are equal to $11°$ in the inner plane and to $9°$ in the intermediate plane. By assuming that the velocity components fall to zero at the wing–nacelle junction and by taking sectional lift coefficients of 1.1 and 0.95 for the wing sections located at $r/R = 0.69$ and 0.79 (with drag coefficients of 0.033 and 0.021), the resulting vertical and lateral forces are respectively $F_z^w = 6\ N$ and $F_x^w = 38\ N$. These values are very close to the loads measured with the balance demonstrating that the upload effect on the wing is due to the rotor wake impinging on it.

5.4.1 Effects of the wing vertical position

To investigate the effect of the distance between the leading edge of the wing and the rotor plane in the tilted configuration, PIV measurements have been carried out on two different relative rotor–wing distances. Apart from the reference condition $h^w/R = 0.324$ which has been described in the previous section, in the following the measurement results for the configuration at $h^w/R = 0.520$ are reported. In Figure 5.48, 5.50, 5.52, 5.54, 5.56, 5.58 the velocity magnitude contours have been shown at several blade phases while in Figure 5.49, 5.51, 5.53, 5.55, 5.57, 5.59 the vorticity contours have been reported in the same azimuthal positions. The evolution of the tip vortices demonstrates an influence of the wing on the rotor wake flow that is rather different with respect to the previous case. Looking at the comparison between the tip vortex displacements with respect to the design case and the isolated rotor, as shown in Figure 5.60, the rotor wake boundary in the present case seems to be not affected by the wing. In fact, the tip vortex displacements has a trend that is very similar to the isolated rotor case. However, if the radial distributions of the axial velocity component U_z are taken into account, as reported in Figure 5.60, a different trend can be observed with respect to the isolated rotor case. In particular, in the isolated rotor case (see Figure 5.16) in the inner part of the rotor wake the axial velocity accelerates going downstream from the rotor disk. In this case however, the axial velocity slightly decreases when approaching to the leading edge of the wing.

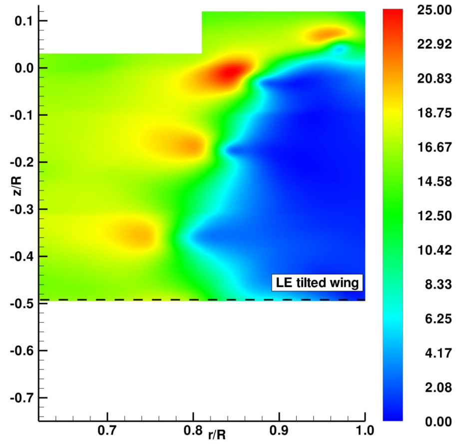

Figure 5.48: *Model: phase-locked velocity magnitude contours, $\psi = 15°$, $h^w/R = 0.520$.*

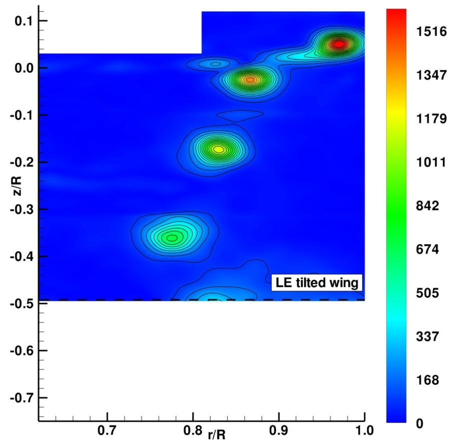

Figure 5.49: *Model: phase-locked vorticity contours, $\psi = 15°$, $h^w/R = 0.520$.*

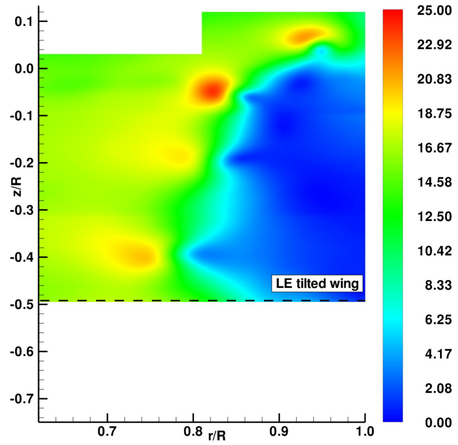

Figure 5.50: *Model: phase-locked velocity magnitude contours, $\psi = 30°$, $h^w/R = 0.520$.*

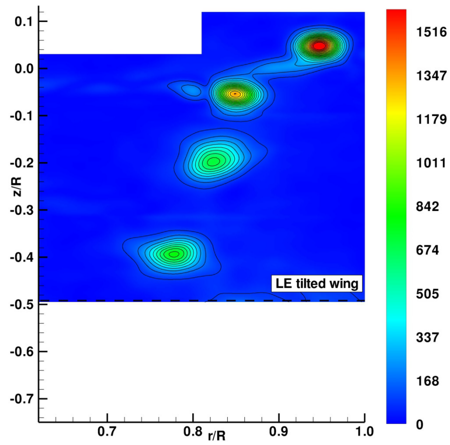

Figure 5.51: *Model: phase-locked vorticity contours, $\psi = 30°$, $h^w/R = 0.520$.*

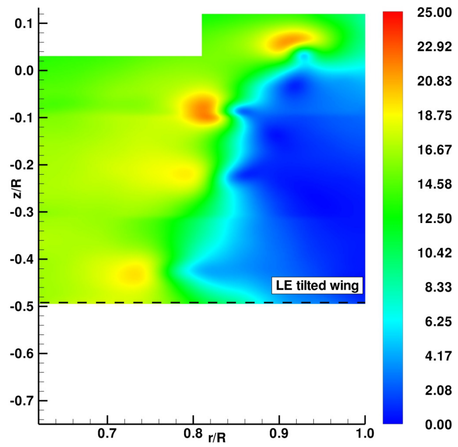

Figure 5.52: *Model: phase-locked velocity magnitude contours, $\psi = 45°$, $h^w/R = 0.520$.*

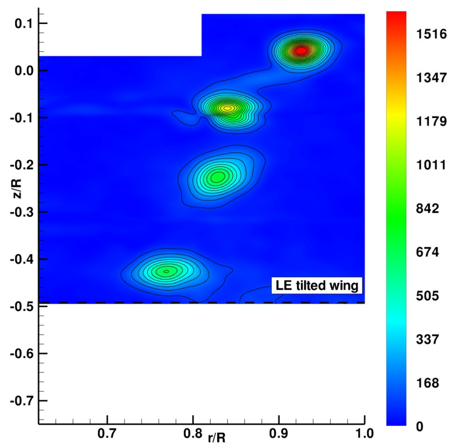

Figure 5.53: *Model: phase-locked vorticity contours, $\psi = 45°$, $h^w/R = 0.520$.*

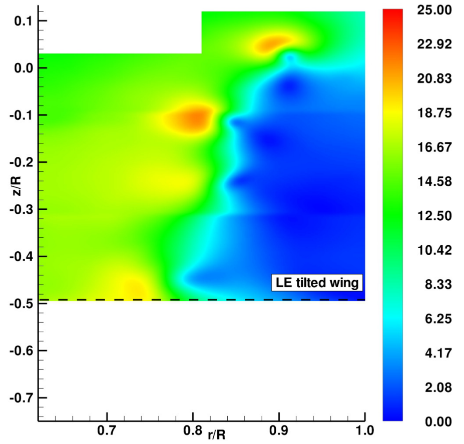

Figure 5.54: *Model: phase-locked velocity magnitude contours, $\psi = 60°$, $h^w/R = 0.520$.*

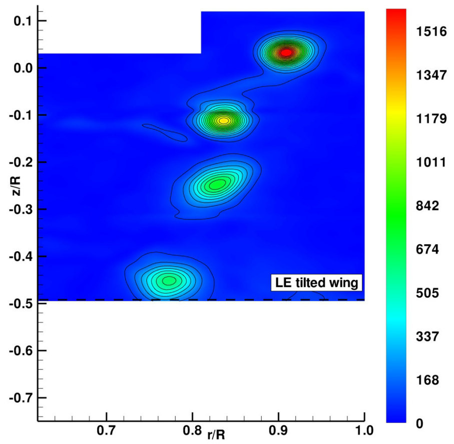

Figure 5.55: *Model: phase-locked vorticity contours, $\psi = 60°$, $h^w/R = 0.520$.*

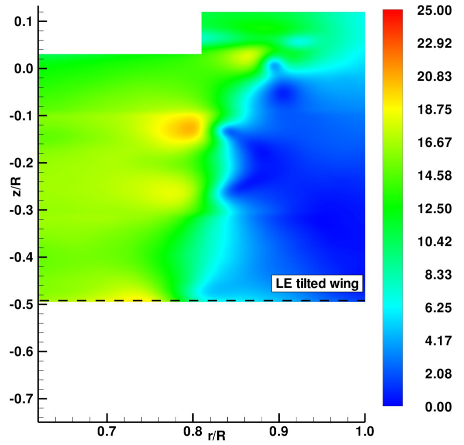

Figure 5.56: *Model: phase-locked velocity magnitude contours, $\psi = 75°$, $h^w/R = 0.520$.*

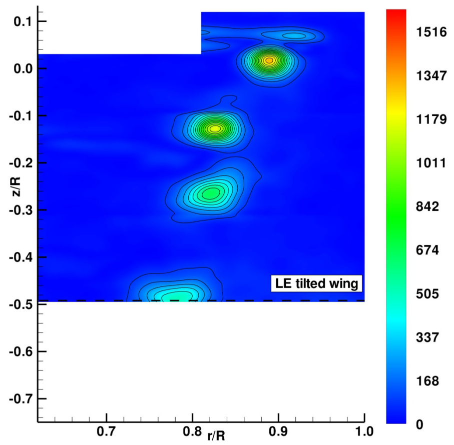

Figure 5.57: *Model: phase-locked vorticity contours, $\psi = 75°$, $h^w/R = 0.520$.*

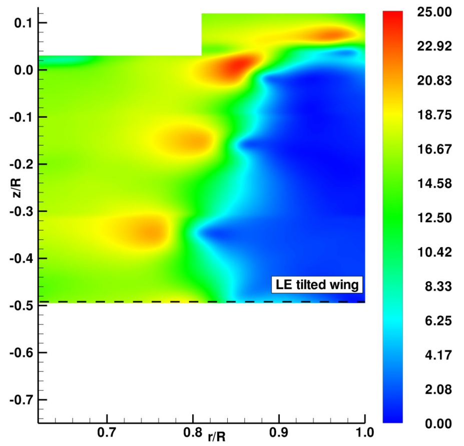

Figure 5.58: *Model: phase-locked velocity magnitude contours, $\psi = 90°$, $h^w/R = 0.520$.*

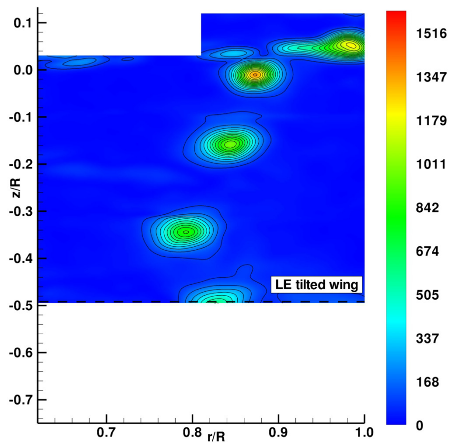

Figure 5.59: *Model: phase-locked vorticity contours, $\psi = 90°$, $h^w/R = 0.520$.*

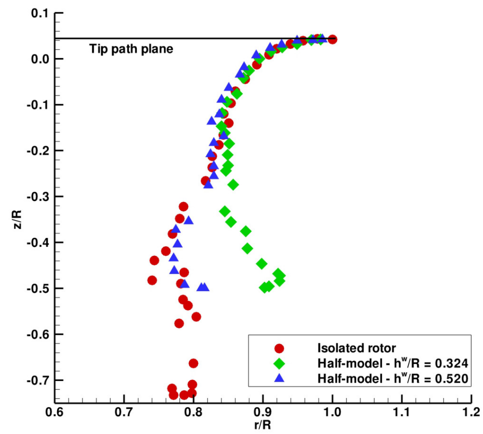

Figure 5.60: *Tip vortex displacements in a r/R–z/R plane: half–model, effect of the wing distance, $h^w/R = 0.324$, $h^w/R = 0.520$.*

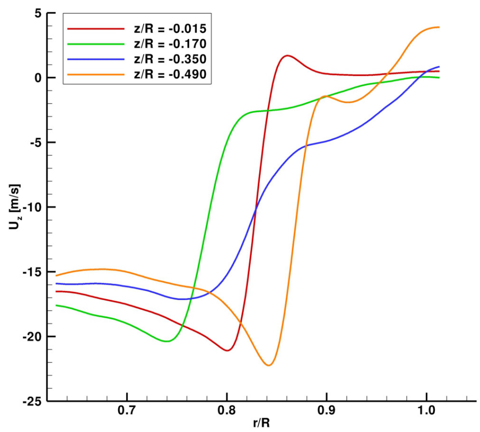

Figure 5.61: *Model: profiles of the axial velocity component U_z at several distances from the rotor disk, $\psi = 15°$.*

CHAPTER 6

Conclusions

After about 50 years of research, tiltrotor aircraft are today a reality in the modern rotorcraft scenario combining together the advantages and the peculiarities of helicopters with modern propeller aircraft and representing a concrete possibility to overcome the main limitations of both of them. For these reasons and thanks to their high versatility, tiltrotor aircraft represent nowadays a very attractive compromise for the civil industry. However, some important limitations are still present in conventional tiltrotor design. For instance, from an aerodynamic point of view, the interaction which occurs in helicopter mode between the wing and the rotors negatively affects the hovering performance and the lifting capability of the aircraft. With the aim of over–passing these problems and to increase the aircraft performance, as for instance the maximum cruise speed reachable and the operative range, non conventional tiltrotor configurations have been investigated during the years. An interesting and promising solution, the tiltwing concept, has been proposed in the frame of the project ERICA founded by the European Community at the beginning of 2000s. However, many aspects of this configuration, as same quite basic aspect of the aerodynamics of wing–rotor interaction, have to be further analysed.

In the present work we gave a detailed description of the phenomena related to the aerodynamic interaction between wing and rotor which arise on a high–performance tiltwing aircraft in hover flight condition. The use of different reliable experimental and numerical tools gave the possibility to describe the problem from different points of view. In particular, the performance of the aircraft and the flow field between the wing and its rotor have been analysed making use of a new experimental test rig designed and manufactured to study tiltrotor aircraft in hover condition. Several measurement campaigns have been carried out on the aircraft model by means of different experimental techniques. A comprehensive and detailed experimental database has been created to allow the study of the phenomena that characterise the wing–rotor aerodynamic interaction in tiltwing aircraft. Since the aircraft geometry is completely public, the experimental database could be used for numerical codes validation. Numerical calculations have been carried out to design the main components of the aircraft (i.e. the rotor blade and the wing) but also they helped the description and the understanding of the physics of the aerodynamic wing–rotor interference problem.

Once the main characteristics and the geometrical dimensions of the aircraft have been defined, a new set of blades have been efficiently designed making use of a two–level optimisation procedure. In the first part of the process, a multi–objective optimizer has been employed in the frame of genetic algorithms to select the chord, the twist and the airfoil distributions along the span of the blade. The choice of a multi–objective optimizer has been dictated by the fact that the operative conditions in which a tiltrotor aircraft works are very different with one another. Indeed the same propulsive system must be used both in helicopter and aircraft mode flight. Since the optimisation process may require a long computational time because it has to evaluate many individuals for each generation, we decided to couple the multi–objective optimizer, based on a controlled elitist genetic algorithm founded NSGA–II (Non–dominated Sorting Genetic Algorithm II) algorithm, with a BEMT (Blade Element Momentum Theory) aerodynamic solver which is mathematically parsimonious and agrees reasonably well with experimental data. At the end of the multi–objective optimisation process, we selected from the Pareto–optimal front the blade which shown the best compromise in terms of rotor performance both in helicopter and aircraft mode flight. In the second step of the optimisation procedure, the chosen blade has been refined introducing a non–linear sweep angle distribution along its span to reduce the power losses due to onset of compressibility effects in the outer part of the blade. The resulting swept blade exhibited a small but not completely negligible increase of the rotor performance with respect to the unswept blade. The comparison between the pressure coefficient C_p distributions on several tip sections of both blades confirmed that the sweep angle distribution delays the onset of compressibility effects on the outer sections of the blade and limits the power losses in this region in aircraft mode. However, the different hover performance between the unswept and swept blades can be justified by the presence of a sort of anhedral effect in the swept blade due to the introduction of the sweep angle distribution along the radius. The consequent modification of the position of the tip vortex emission avoid the interaction between the tip vortex with the following blade, otherwise present. To assess the quality of the resulting swept blade, it has been compared with similar rotors (the ERICA rotor in hover condition and an high–speed propeller in cruise flight) demonstrating good performance with respect to them despite its very complex aerodynamic shape.

As known, to reduce the negative effects due to the wing–rotor interaction in helicopter mode, a possible approach could be represented by the reduction of the wing surface on which the rotor wake strikes. Following the tiltwing concept, we achieved this objective by designing a wing divided in two portions one of which, the external part, can be tilted. Although it is rather obvious that the tilting part of the wing needs to have span that is almost equal to the rotor radius, during the design of the wing we quantified the effects of the rotor wake on several wing configurations. In this way, we demonstrated that even if the span of the tilting wing is slightly smaller than the rotor radius, the vertical loads on the wing increases abruptly both in hover and in vertical climb. Moreover, from numerical calculations carried out with the CFD (Computational Fluid Dynamics) code ROSITA (ROtorcarft Software ITAly) we understood that in proximity of the leading edge of the tilted wing, the rotor wake is modified in such a way that leads to lower values of the wake boundary contraction. These preliminary analysis has been performed using steady simulations and reproducing the effects of the rotor with a simplified actuator disk model (which accounted only for axial load without simulating the swirl effect given by the blade rotation). However, further experimental measurements and more accurate calculations demonstrated the validity of this approach.

The new experimental test rig represented the 0.25 scaled tiltwing half–model and consisted of two main independent components that were the rotor system and the half–wing with an image plane. Since a tiltwing aircraft has small rotors compared with the span of the wing, close to the aircraft symmetry plane wing–rotor and rotor–rotor interference are rather small and thus an half–model configuration can be used instead of the full–span one. The use of different experimental techniques, as force and torque measurements and PIV (Particle Image Velocimetry), allowed to give a detailed description of the interaction between wing and rotors in a tiltwing aircraft.

All the tests of this activity have been conducted at a tip Mach number that was 0.32 and correspond to $1/2$ the tip Mach number of full–scale aircraft at design point in hover. The first tests on the isolated rotor gave us the possibility to characterise the rotor system. On this system we carried out CFD simulations to validate the numerical approach used in the blade design. The agreement that we found from the comparison between numerical predictions and the experimental data was very good, demonstrating the validity of the CFD analysis carried out on the rotor at full–scale. By comparing the isolated rotor performance with the performance aircraft in the half–model configuration, we were able to quantify the influence of the wing on the rotor in terms of thrust and power. When the wing is untilted, we saw that it gave a sort of partial ground effect on the pure rotor performance, increasing slightly the rotor thrust, while the effect of the tilted wing configuration is negligible. On the other hand, if we analysed the whole aircraft performance, the net thrust produced by the rotor in a given trim condition was significantly less than the required value for that condition in the untilted case. However, when the tilted wing configuration was taken into account, the performance of the aircraft were very similar to the performance of the isolated hovering rotor. This result is interesting because, even if it is rather intuitive, in public literature there are no demonstrations of this fact. Moreover, the same results have been found modifying the relative distance between the wing and the rotor. Therefore, from the rotor point of view, the most important and limiting factor for its performance is clearly the wing configuration. Force measurements allowed also to quantify the effects of the rotor wake on the wing in terms of aerodynamic loads. In particular, we focused our attention on two force components acting on the wing: the vertical force, that was parallel to the rotor thrust, and the longitudinal force, that was parallel to the ideal horizontal aircraft axis. When the untilted wing configuration was considered, while the longitudinal force was almost zero, the vertical force was high when compared with the rotor thrust. Moreover, since the latter force component was directed in the opposite direction of the rotor thrust (download), the rotor should produce much more thrust to hover with respect to the isolated case. The results found in this work for the untilted wing case agrees well with the download measurements on conventional tiltrotor models. On the other hand, the effect of the rotor wake on the tilted wing was very different. In fact, in this case the vertical force acting on the wing was small but not completely negligible. Moreover, both experimental measurements and numerical calculations demonstrated that the vertical force that raised on the wing in the tilted configuration was positive (upload). In particular, by reproducing the effects of the rotor with an actuator disk model which included the swirl effect, steady CFD simulation have been carried out in the experimental conditions. The good agreement between the numerical prediction and the experimental data for the wing loads allowed to validate the computational approach used in the design phase. Moreover, a good agreement was also found by comparing these results with the results of an unsteady simulation in a given aircraft trim condition ($\theta = 12°$, $\beta = 2.5°$, $\zeta = -9.8°$, $M_{Tip} = 0.32$). The unsteady results are in agreement also with the rotor data.

Due to the lack of information on the rotor wake flow field over a tiltwing aircraft in hover, the purpose of the PIV measurements was to give a detailed and useful description of the flow field around a tiltwing aircraft in order to understand the mechanism through which the blade tip vortex strikes in such a way on the surface of the wing. Several azimuthal and radial measurement planes have been considered in correspondence of the rotor blade tip with and without the wing. PIV surveys on the isolated rotor system shown that the rotor wake boundary assumed an asymptotic value at an axial distance of about $z/R = 0.4$ from the rotor disk, where the maximum contraction of the wake was $0.78\ R$. Different results were found when the tilted wing was placed below the rotor. A strong variation on the rotor wake flow boundary was observed when the wing was located at the design distance from the rotor ($h^w/R = 0.324$). In particular, the maximum contraction of the wake was achieved at $z/R = 0.14$ assuming a value of $0.85\ R$. This result shows that, even though the rotor wake is modified by the presence of the wing, the tilted portion of the wing remains inside the wake boundaries assuring low values of vertical force acting on it. The analysis of the radial distributions of the axial velocity component U_z at several distance from the rotor demonstrated that the flow accelerated once it reached the leading edge of the tilted wing. PIV measurements on three different plane in the radial direction allowed to verify the presence of a non negligible swirl component inside the rotor slipstream. This velocity component has been quantified over the leading edge of the tilted wing demonstrating the presence of an upload force on the tilted wing in hover. When a lower position of the wing was accounted ($h^w/R = 0.520$), the evolution of the tip vortices demonstrates an influence of the wing on the rotor wake flow that was rather different with respect to the design case. While the rotor wake boundary seemed to be not affected by the wing in this case, a different trend of the radial distributions of the axial velocity component U_z is observed. By comparing the flow field, PIV measurements validated also the unsteady simulation on the hovering aircraft.

In conclusion, the activity described in the present work successfully contributs to the research in the field of tiltrotor and tiltwing aircraft by giving interesting results about the aerodynamic interaction between wing and rotor in this kind of aircraft.

APPENDIX *A*

ROSITA CFD Software

The CFD code ROSITA (ROtorcraft Software ITAly) [11] numerically integrates the unsteady Reynolds Averaged Navier–Stokes Equations (RANS) equations, coupled with the one–equation turbulence model of Spalart–Allmaras [76]. Multiple moving multi–block grids can be used to form an overset grid system by means of the Chimera technique, as described in the following. To simplify the solution of the flow field in overset grid systems, the Navier–Stokes equations are formulated in terms of the absolute velocity, expressed in a relative frame of reference RF linked to each component grid. The equations are discretized in space by means of a cell–centred finite–volume implementation of the Roe's scheme [73]. Second order accuracy is obtained through the use of MUSCL extrapolation supplemented with a modified version of the Van Albada limiter introduced by Venkatakrishnan [80]. The viscous terms are computed by the application of the Gauss theorem and using a cell–centred discretization scheme. Time advancement is carried out with a dual–time formulation [39], employing a 2^{nd} order backward differentiation formula to approximate the time derivative and a fully unfactored implicit scheme in pseudo–time. The equation for the state vector in pseudo–time is non–linear and is solved by sub–iterations [10]. In the dual–time method, there is no stability limit with respect to the size of the physical time step Δt and this approach can lead to a large reduction in CPU time compared to a fully implicit method in physical time. The physical time step Δt is here only limited by solution accuracy requirements. However, there is a stability condition on the pseudo–time step, as shown by Hirsch [37] for viscous flow calculations. The generalised conjugate gradient (GCG), in conjunction with a block incomplete lower–upper preconditioner, is used to solve the resulting linear system.

The connectivity between the (possibly moving) component grids is computed by means of the Chimera technique. The approach adopted in ROSITA is derived from that originally proposed by Chesshire and Henshaw [14], with modifications to further improve robustness and performance. The domain boundaries with solid wall conditions are firstly identified and all points in overlapping grids that fall close to these boundaries are marked as holes (seed points). Then, an iterative algorithm identifies the donor and fringe points and lets the hole points grow from the seeds until they entirely fill the regions outside the computational domain. To speed up the search of donor points, oct-tree and ADT (alternating digital tree) data structures are employed.

The ROSITA solver is fully capable of running in parallel on computing clusters. The parallel algorithm is based on the message passing programming paradigm and the parallelization strategy consists in distributing the grid blocks among the available processors. Each grid block can be automatically subdivided into smaller blocks by the CFD solver to attain an optimal load balancing.

Numerical computations have been carried out alternatively on two different cluster. The first one is the Lagrange cluster at CINECA, made up of 208 bi-processor Intel® Xeon QuadCore $3.166\ GHz$ nodes interconnected by an Infiniband $4X$ Double Data Rate with capacity of $20\ Gb/s$. The second one is the Eurora cluster at CINECA, made up of 32 bi–processor eight–core Intel® Xeon® CPU E5–2658 at $2.10\ GHz$ with $16\ GB$ RAM and 32 bi–processor eight–core Intel® Xeon® CPU E5–2687 at $3.10\ GHz$ with $16\ GB$ RAM interconnected by a Qlogic QDR Infiniband high–performance network with capacity of $40\ Gb/s$. Numerical activities on the latter cluster has been carried out in the frame of the project ISCRA named IscrC_ASTRO.

APPENDIX $\mathcal{B}$

Blade Element Momentum Theory

The use of a genetic algorithm implied a huge number of fitness function evaluations in the optimisation procedure. Moreover, every time the fitness function had to be evaluated, the aerodynamic performance of a blade needed to be computed several times during the analysis for each flight condition considered. Because CFD computations are very time consuming, to reduce the computational cost of the whole process, the multi–objective optimizer has been coupled with an aerodynamic solver based on the BEMT (Blade Element Momentum Theory) approach [48]. Even though this aerodynamic model is very simple, it is mathematically parsimonious [49] and suitable to predict reasonably well the performance of helicopter rotor [21], aircraft propeller [34] and proprotor [51].

As known, the BEMT aerodynamic solver employed a physicomathematical rotor model which is based on a combination of the simple momentum theory (MT) with the classical blade element theory (BE). The coupling between these two methods allows to alleviate the limitations of the first approach and leads to a model which is more accurate and accounts for non–uniform induced velocity distribution along the blade. Therefore the BEMT rotor model is able to predict, as precisely as possible, the aerodynamic forces and moments acting on different blade sections. As shown in Figure B.1, the rotor disk is represented by several elementary annuli of width dr and radius r. According to the generalised differential momentum theory [30], each narrow element produces a thrust dT^{MT} and a torque dQ^{MT} that can be expressed as functions of the induced velocity components as follows:

$$dT^{MT} = 4\pi r\rho\left(V_\infty + v_i\right)v_i\mathbb{F}dr, \tag{B.1}$$

$$dQ^{MT} = 4\pi r^3\rho\left(V_\infty + v_i\right)w_i\mathbb{F}dr, \tag{B.2}$$

where V_∞ is the free stream axial velocity of the rotor, v_i is the induced axial velocity

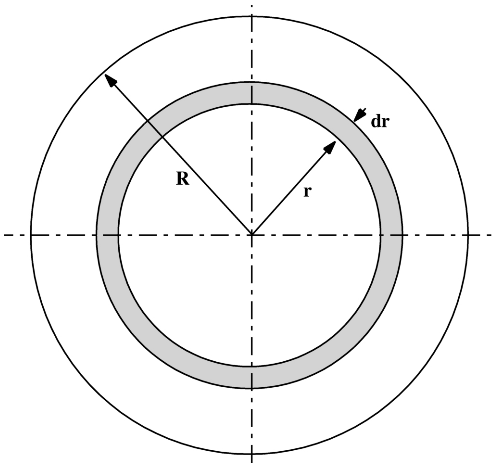

Figure B.1: *Rotor disk elementary annuli.*

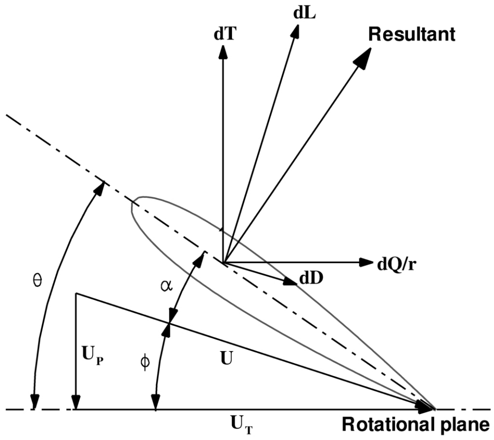

Figure B.2: *Rotor blade section.*

component while w_i the swirl component. Equation B.1 and B.2 have been written for a rotor in axial flight and the hovering state beings the lower limit with null free stream axial velocity. $\mathbb{F}$ represents the Prandtl's approximate function for the tip loss correction [31], defined as:

$$\mathbb{F} = 2\pi \cos^{-1}(\exp^{-f}), \tag{B.3}$$

where f is a function of the induced inflow angle ϕ, the local radius r and the number of blades N_b:

$$f = \frac{N_b}{2}\frac{R-r}{r\sin\phi}. \tag{B.4}$$

According to the blade element analysis of helicopter rotors in hover and axial flight [48], the resultant velocity U on a blade section of radius r is given by the vectorial sum of the axial velocity component normal to the rotor, equal to the sum of the free stream velocity with the induced axial velocity ($U_P = V_\infty + v_i$), and the azimuthal velocity component, expressed by the sum of the local azimuthal velocity with the induced swirl ($U_T = (\Omega + w_i) r$). For a given blade section, as shown in Figure B.2, the induced inflow angle will be:

$$\phi = \tan^{-1}\frac{V_\infty + v_i}{(\Omega + w_i)\, r}. \tag{B.5}$$

As consequence, the aerodynamic angle of attack of a given blade section is the difference between the local pitch angle and the induced inflow angle ($\alpha = \theta - \phi$). The elementary contribution to the rotor thrust dT^{BE} and the corresponding elementary contribution to the rotor torque dQ^{BE} will be:

$$dT^{BE} = \frac{1}{2}\rho U^2 N_b \left(C_l \cos\phi - C_d \sin\phi\right) c dr, \tag{B.6}$$

$$dQ^{BE} = \frac{1}{2}\rho U^2 N_b \left(C_l \sin\phi + C_d \cos\phi\right) c r dr, \tag{B.7}$$

where $U = \sqrt{U_P^2 + U_T^2}$ is the resultant velocity modulus seen by the blade element and C_l and C_d are respectively the lift and drag coefficient of the airfoil section of local chord c.

Equation B.1 and B.2 from momentum analysis can be respectively equated together with Equation B.6 and B.7 given by the blade element theory. After same algebra, the following relationships for the induced axial velocity and swirl component arise:

$$v_i = \frac{(\Omega - w_i)\, N_b c\, (C_l \cos\phi - C_d \sin\phi)}{8\mathbb{F}\pi \sin\phi \cos\phi}, \tag{B.8}$$

$$w_i = \frac{\Omega N_b c\, (C_l \sin\phi + C_d \cos\phi)}{8\mathbb{F}\pi r \sin\phi \cos\phi + N_b c\, (C_l \sin\phi + C_d \cos\phi)}. \tag{B.9}$$

Given the blade geometry and section aerodynamic characteristics, the induced velocity components may be evaluated at different radii by solving Equation B.8 and B.9. Since the aerodynamic coefficients of a section depend on the aerodynamic angle of attack α which is related to the ratio between the axial and azimuthal velocity components, Equation B.8 and B.9 can be efficiently solved recursively for each blade element. The BEMT solver extracts from a database interpolated values of the aerodynamic characteristics of airfoil sections. Airfoil data have been stored in tables for a wide range of angle of attack, Reynolds and Mach number, collecting together wind tunnel data [1] and two–dimensional CFD results. Finally, thrust and torque elementary contributions are computed using Equation B.6 and B.7 and rotor global loads are evaluated integrating the different blade element contributions.

Bibliography

[1] I.H. Abbott and A.E. Von Doenhoff. *Theory of Wing Sections, Including a Summary of Airfoil Data*. McGraw–Hill Book Co., Inc. (Reprinted by Dover Publications, 1959), New York, 1949.

[2] C.W.J. Acree. Jvx proprotor performance calculations and comparisons with hover and airplane–mode test data. Technical Report TM–2009–215380, NASA, 2009.

[3] Download alleviation for the XV-15: computation and experiments of flows around the wing. P. kjellgren and a. hassan and j. sivasubramanian and l. cullen and d. cerchie and i. wygnanski. In *AIAA–2002–6007*, Williamsburg, Virginia, USA, November 5–7 2002. 2002 Biennial International Powered Lift Conference and Exhibit.

[4] P. Alli, F. Nannoni, and M. Cicalè. Erica: The european tiltrotor design and critical technology projects. In *AIAA/ICAS*, Day-ton, Ohio, USA, 14–17 July 2005. International Air and Space Symposium and Exposition: The Next 100 Years.

[5] Anonymous. Evonik industrries web site. `http://www.rohacell.com`, 2013. [Online; accessed 12–November–2013].

[6] P. Beaumier, J. Decours, and T. Lefebvre. Aerodynamic and aeroacoustic desing of moder tilt–rotors: the onera experience. In *ICAS*, Anchorage, Alaska, USA, 14–19 September 2008. 26^{th} International Congress of the Aeronautical Sciences.

[7] J.A.J. Bennett. The fairey gyrodyne. *Journal of the Royal Aeronautical Society*, 53, 1949.

[8] M.J. Bhagwat and G.J. Leishman. On the aerodynamic stability of helicopter rotor wakes. *AIAA Journal*, 38(2):301–308, 2000.

[9] E. Bianchi, A. Russo, F. Kiessling, R. Ferrer, O. Dieterich, M . Frisoni, R. Bakker, V. Riziotis, D. Petot, and M. Lanz. Numerical whirl–flutter investigation of the european tiltrotor concept: current status and future prospects. Marseilles, France, 14–16 September 2004. 30^{th} European Rotorcraft Forum.

[10] M. Biava. *RANS computations of rotor/fuselage unsteady interactional aerodynamics*. PhD thesis, Politecnico di Milano, Milano, Italy, 2007.

[11] M. Biava, A. Pisoni, A. Saporiti, and L. Vigevano. Efficient rotor aerodynamics predictions with an euler method. Friedrichshafen, Germany, 16–18 September 2003. 29^{th} European Rotorcraft Forum.

[12] M. Biava, M. Valentini, and L. Vigevano. Trimmed actuator disk modeling for helicopter rotor. Moscow, Russia, 3–6 September 2013. 39^{th} European Rotorcraft Forum.

[13] C. Bottasso, L. Trainelli, P. Abdel-Nour, and G. Labó. Titlrotor analysis and design using finite element multibody procedures. Bristol, UK, 17–20 September 2002. 28^{th} European Rotorcraft Forum.

[14] G. Chesshire and W. D. Henshaw. Composite overlapping meshes for the solution of partial differential equations. *Journal of Computational Physics*, 90:1–64, 1990.

[15] W.L. Cook and P. Poisson-Quinton. A summary of wind tunnel research on tilt rotors from hover to cruise flight. Marseille, France, 1972 September 13–15. AGARD, Fluid Dynamics Panel Specialists' Meeting on the Aerodynamics of Rotary Wings.

[16] A. Darabi, A. Stalker, M. McVeigh, and I. Wygnanski. The rotor wake above a tiltrotor airplane–model in hover. In *AIAA*, Orlando, Florida, USA, 23–26 June 2003. 33^{rd} AIAA Fluid Dynamics Conference.

[17] K. Deb. *Optimization for Engineering Design: Algorithms and Examples*. Prentice–Hall of India Private Limited, New Delhi, 1995.

[18] K. Deb. A fast and elitist multiobjective genetic algorithm: Nsga–ii. *IEEE Transactions on Evolutionary Computation*, 6(2):182–197, April 2002.

[19] K. Deb. *Multi–objective optimization using evolutionary algorithms*. John Wiley and Sons Ltd, Southern Gate, Chichester, West Sussex, United Kingdom, 2008.

[20] J. Decours, S. Burguburu, and F. Falissard. Performance assessment of the erica tilt-rotor in cruise. Paris, France, 7–9 September 2010. 36^{th} European Rotorcraft Forum.

[21] G. Droandi, G. Gibertini, G. Campanardi, D. Grassi, C. Macchi, and L. Peveroni. Wind–tunnel rotor model for hover and forward flight tests. Naples, Italy, 9-12 September 2013. AIDAA XXII Conference.

[22] A.J. Evans and G. Liner. A wind–tunnel investigation of the aerodynamic characteristics of a full–scale supersonic–type three–blade propeller at mach numbers to 0.96. Technical Report TR–1375, NACA, 1958.

[23] J. Everett-Heath. *British Military Helicopters*. Arms and Armour Press, London, UK, 1986.

[24] F. Felker. Wing download results from a test of a 0.658-scale v–22 rotor and wing. *Journal of the American Helicopter Society*, 37(4):58–63, October 1992.

[25] F. Felker and J. S. Light. Aerodynamic interactions between a rotor and wing in hover. *Journal of the American Helicopter Society*, pages 53–61, April 1988.

[26] R.J. Francillon. *McDonnell Douglas Aircraft since 1920*. Putnam Aeronautical Books, London, UK, 1988.

[27] T.M. Gaffey. The effect of positive pitch–flap coupling (negative δ_3) on rotor blade motion stability and flapping. Washington, D.C., USA, May 8–10 1968. American Helicopter Society 24^{th} Annual Forum.

[28] D. Gazdag and L. Altonin. Potential use of tiltrotor aricraft in canadian aviation. Technical Report TM–102245, NASA Technical Memorandum, Ames Research Center, Moffett Field, CA, USA, 1990.

[29] G. Gibertini, F. Auteri, G. Campanardi, C. Macchi, A. Zanotti, and A. Stabellini. Wind tunnel tests of a tilt–rotor aircraft. *The Aeronautical Journal*, 115(1167):315–322, May 2011.

[30] H. Glauert. *Airplane Propellers, Division L of Aerodynamic Theory*. Springer Verlag, Berlin, Germany, 1935.

[31] L. Goldstein. On the vortex theory of screw propellers. *Proceedings of the Royal Society of London. Series A, Containing Papers of a Mathematical and Physical Character*, 123(792):440–465, 1929.

[32] A. Grife, A. Darabi, and I. Wygnanski. Download reduction on a three dimensional v–22 model using active flow control. In *AIAA–2002–3071*, St. Louis, Missouri, USA, June 24–26 2002. 1^{st} AIAA Flow Control Conference.

[33] V. Gupta and J. D. Baeder. Investigation of quad tiltrotor aerodynamics in forward flight using cfd. In *AIAA*, St. Louis, MO, USA, 24–26 June 2002. 20^{th} AIAA Applied Aerodynamics Conference.

[34] O. Gur and A. Rosen. Comparison between blade-element models. *The Aeronautical Journal*, 112(1138):689–704, December 2008.

[35] E.J. Hall. Prop-rotor stability at high advance ratios. *Journal of the American Helicopter Society*, 11(2), April 1966.

[36] G. Haller. An objective definition of a vortex. *Journal of Fluid Mechanics*, 525:1–26, 2005.

[37] C. Hirsch. *Numerical computation of internal and external flows*. John Wiley & Sons, 1988.

[38] National Instruments. Labview version 2013, user's giude. `http://www.ni.com`, 2013. [Online; accessed 1–December–2013].

[39] A. Jameson. Time dependent calculations using multigrid with applications to unsteady flows past airfoils and wings. In *AIAA 91–1596*, Honolulu, HI., 1991. 10^{th} AIAA Computational Fluid Dynamics Conference.

[40] W. Johnson. Studies in tilt rotor vtol aircraft aeroelasticity, volume 1. Technical Report TM–X–69497, NASA, 1973.

[41] W. Johnson. Studies in tilt rotor vtol aircraft aeroelasticity, volume 2. Technical Report TM–X–69496, NASA, 1973.

[42] W. Johnson. Analytical model for tilting proprotors aircraft dynamics, including blade torsion and coupled bending modes and conversion mode operation. Technical Report TM X–62369, NASA, 1974.

[43] W. Johnson. Dynamics of tilting proprotor aircraft in cruise flight. Technical Report TN D–7677, NASA, 1974.

[44] W. Johnson. *Helicopter Theory*. Princeton University Press, Princeton, New Jersey, USA, 1980.

[45] W. Johnson. Calculation of tilt rotor aeroacoustic model (tram dnw) performance, airloads, and structural loads. Atlanta, Georgia, USA, November 2000. American Helicopter Society Aeromechanics Specialists' Meeting.

[46] T. Lefebvre, P. Beaumier, S. Canard-Caruana, A. Pisoni, A. Pagano, A. Sorrentino, B. Van der Wall, J. Yin, C. Arzoumanian, S. Voutsinas, and C. Hermans. Aerodynamic and aero-acoustic optimization of modern tilt-rotor blades within the adyn project. In *ECCOMAS*, Jyväskylä, Finlande, 24–28 July 2004. 4^{th} European Congress on Computational Methods in Applied Sciences and Engineering.

[47] G.J. Leishman and A. Bagai. Challenges in understanding the vortex dynamics of helicopter rotor wakes. *AIAA Journal*, 36(7):1130–1140, 1998.

[48] J. G. Leishman. *Principles of Helicopter Aerodynamics*. Cambridge Aerospace Series, New York, NY 10013–2473, USA, 2006.

[49] J. G. Leishman and K. M. Rosen. Challenges in the aerodynamic optimization of high-efficiency proprotors. *Journal of the American Helicopter Society*, 56(1):12004–1200421, January 2011.

[50] E.K. Liberatore. *Helicopters Before Helicopters*. Krieger Publishing, Malabar, Florida, USA, 1998.

[51] J. Liu, D. J. Paisley, and J. Hirsh. Tiltrotor aerodynamic blade design by numerical optimization method. Washington, D.C., USA, May 1990. American Helicopter Society Aerodynamics 46^{th} Annual Forum.

[52] Jr. L.K. Loftin. Theoretical and experimental data for a number of naca 6a–series airfoil section. Technical Report TR–903 (Supersedes NACA TN–1368), NACA, 1948.

[53] K.H. Lyle, C.L. Burley, and D.S. Prichard. A comparison of measured and predicted xv-15 tiltrotor surface acoustic pressures. Williamsburg, VA, October 1997. American Helicopter Society Technical Specialists' Meeting for Rotorcraft Acoustics and Aerodynamics.

[54] M.D. Maisel, D.J. Giulianetti, and D.C. Dugan. The history of the xv–15 tilt rotor research aircraft: from concept to flight. Monographs in Aerospace History, 17 SP–2000–4517, NASA History Division, Washington, D.C., USA, 2000.

[55] The MathWorks. Global optimization toolbox, user's giude. `http://mathworks.it`, 2012. [Online; accessed 10–December–2012].

[56] M.S. McCluer and J.L. Johnson. Full–span tiltrotor aeroacoustic model (fs tram). overview and initial testing. San Francisco, CA, USA, 23–25 January 2002. American Helicopter Society Aerodynamics, Acoustics, and Test and Evaluation Technical Specialists' Meeting.

[57] M. A. McVeigh. The v–22 tiltrotor large–scale rotor performance/wing download test and comparison with theory. *Vertica*, 10(3/4):281–297, 1986.

[58] M. A. McVeigh, H. J. Rosenstein, and F. J. McHugh. Aerodynamic design of the xv–15 advanced composite tiltrotor blade. St. Louis, MO, USA, 9–11 May 1983. American Helicopter Society Aerodynamics 39^{th} Annual Forum.

[59] M.A. McVeigh, W.K. Grauer, and D.J. Paisley. Rotor/airframe interaction on tiltrotor aircraft. *Journal of American Helicopter Society*, 35(3):43–51, July 1990.

[60] R. Meakin. Unsteady simulation of the viscous flow about a v–22 rotor and wing in hover. In *AIAA–95–3463–CP*, pages 332–344, Baltimore, MD, USA, 7–10 August 1995. AIAA Atmospheric Flight Mechanics Conference Proceedings.

[61] Z. Michalewicz. *Genetic Algorithms + Data Structures = Evolution Programs*. Springer–Verlag Berlin Heidelberg, 1992.

[62] Z. Michalewicz and C. Z. Janikow. Handling constraints in genetic algorithms. pages 151–157. Proceedings of the Fourth International Conference on Genetic Algorithms, 1991.

[63] A. Neubauer. Adaptive non–uniform mutation for genetic algorithms. *Computational Intelligence Theory and Application*, 1226:pp. 24–34, 1997.

[64] D. J. Paisley. Rotor aerodynamic optimization for high speed tiltrotors. St. Louis, MO, USA, 18–20 May 1987. American Helicopter Society Aerodynamics 43^{th} Annual Forum.

[65] A. Le Pape and P. Beaumier. Numerical optimization of helicopter rotor aerodynamic performance in hover. *Aerospace Science and Tecnology*, 9(3):191–201, 2005.

[66] E.W. Patterson and A.L. Braslow. Ordinates and theoretical pressure-distribution data for naca 6– and 6a–series airfoil sections with thicknesses from 2 to 21 and from 2 to 15 percent chord, respectively. Technical Report TR–R–84, NASA, 1961.

[67] L. Peveroni. Sviluppo e qualifica di una attrezzatura di prova per modelli di rotore di elicottero. Master's thesis, Politecnico di Milano, Milano, Italy, 2011.

[68] PIVTEC. Pivview 2c version 3.0. user manual. `www.pivtec.com`, January 2009.

[69] D.R. Polak, W. Rehm, and A.R. George. Effects of an image plane on the tiltrotor fountain flow. *Journal of American Helicopter Society*, 45(2):90–96, April 2000.

[70] S. Poles, Y. Fu, and E. Rigoni. The effect of initial population sampling on the convergence of multi–objective genetic algorithms. *Multiobjective Programming and Goal Programming: Theoretical Results and Practical Applications*, 618(3):pp. 123–133, 2009.

[71] M.A. Potsdam and R.C. Strawn. Cfd simulations of tiltrotor configurations in hover. *Journal of the American Helicopter Society*, 50(1):82–94, 2005.

[72] R.R. Reber. Civil tiltrotor transportation for the 21^{st} century. In *AIAA 93-4875*. AIAA International powered lift conference, 1993.

[73] P. L. Roe. Approximate riemann solvers, parameter vectors and difference schemes. *Journal of Computational Physics*, 43:357–372, 1981.

[74] J. Roskam. *Aircraft design*. Roskam Aviation and Engineering Corporation, Rt4, Box 274, Ottawa, Kansas, 66067, USA, 1985.

[75] A.H. Shapiro. *The Dynamics and Thermodynamics of Compressible Fluid Flow*. The Ronald Press Company, New York, 1992.

[76] P.R. Spalart and S.R. Allmaras. One equation model for aerodynamic flows. In *AIAA 92-0439*, Reno, Nevada, USA, 1992. 30^{th} AIAA Aerospace Science Meeting & Exhibit.

[77] J.P. Spenser. *Whirlybirds, A History of U.S. Helicopter Pioneer*. University of Washington Press, Washington D.C., USA, 1998.

[78] E. Torenbeek. *Synthesis of Subsonic Airplane Design*. Delft University Press, Rotterdam, Netherlands, 1976.

[79] B.G. van der Wall and O. Schneider. Wind tunnel tests in dnw: Report of data acquired by dlr institute of flight systems. Technical Report TILTAERO/WP5/DLR/R–01/A, TILTAERO Project, 2006.

[80] V. Venkatakrishnan. On the accuracy of limiters and convergence to steady state solutions. In *AIAA 1993–880*, Reno, Nevada, USA, 1993. 31^{st} AIAA Aerospace Science Meeting & Exhibit.

[81] A. Viscardi, J. Decours, W. Khier, and S. Voutsinas. Code–to–code comparisons for the blind–test activity of the tiltaero project. Florence, Italy, 13–15 September 2005. 31^{st} European Rotorcraft Forum.

[82] J.A. Weiberg and M.D. Maisel. Wind-tunnel tests of the xv–15 tilt rotor aircraft. Technical Report NASA–TM–81177, NASA, 1980.

[83] K.G. Wernicke and J.P. Magee. Xv–15 flight test results compared with design goals. In *AIAA 79–1839*. 30^{th} AIAA Aerospace Science Meeting & Exhibit, 1979.

[84] T. L. Wood and M. A. Peryea. Reduction of tiltrotor download. *Journal of the American Helicopter Society*, 40(3):42–51, July 1995.

[85] L.A. Young, D. Lillie, M. McCluer, G.K. Yamauchi, and M.R. Derby. Insights into airframe aerodynamics and rotor-on-wing interactions from a 0.25–scale tiltrotor wind tunnel model. San Francisco, CA, USA, 23–25 January 2002. American Helicopter Society Aerodynamics, Acoustics, and Test and Evaluation Technical Specialists' Meeting.

[86] A. Zanotti. *Retreating blade dynamic stall*. PhD thesis, Politecnico di Milano, Milano, Italy, 2012.